

Magnetic particle actuation for functional biosensors

Citation for published version (APA):

Janssen, X. J. A. (2009). *Magnetic particle actuation for functional biosensors*. [Phd Thesis 1 (Research TU/e / Graduation TU/e), Applied Physics and Science Education]. Technische Universiteit Eindhoven.
<https://doi.org/10.6100/IR652765>

DOI:

[10.6100/IR652765](https://doi.org/10.6100/IR652765)

Document status and date:

Published: 01/01/2009

Document Version:

Publisher's PDF, also known as Version of Record (includes final page, issue and volume numbers)

Please check the document version of this publication:

- A submitted manuscript is the version of the article upon submission and before peer-review. There can be important differences between the submitted version and the official published version of record. People interested in the research are advised to contact the author for the final version of the publication, or visit the DOI to the publisher's website.
- The final author version and the galley proof are versions of the publication after peer review.
- The final published version features the final layout of the paper including the volume, issue and page numbers.

[Link to publication](#)

General rights

Copyright and moral rights for the publications made accessible in the public portal are retained by the authors and/or other copyright owners and it is a condition of accessing publications that users recognise and abide by the legal requirements associated with these rights.

- Users may download and print one copy of any publication from the public portal for the purpose of private study or research.
- You may not further distribute the material or use it for any profit-making activity or commercial gain
- You may freely distribute the URL identifying the publication in the public portal.

If the publication is distributed under the terms of Article 25fa of the Dutch Copyright Act, indicated by the "Taverne" license above, please follow below link for the End User Agreement:

www.tue.nl/taverne

Take down policy

If you believe that this document breaches copyright please contact us at:

openaccess@tue.nl

providing details and we will investigate your claim.

Magnetic particle actuation for functional biosensors

PROEFSCHRIFT

ter verkrijging van de graad van doctor aan de
Technische Universiteit Eindhoven, op gezag van de
rector magnificus, prof.dr.ir. C.J. van Duijn, voor een
commissie aangewezen door het College voor
Promoties in het openbaar te verdedigen
op woensdag 18 november 2009 om 16.00 uur

door

Xander Jozef Antoine Janssen

geboren te Roermond

Dit proefschrift is goedgekeurd door de promotor:

prof.dr.ir. M.W.J. Prins

Copromotor:

dr. L.J. van IJzendoorn

A catalogue record is available from the Eindhoven University of Technology
Library

ISBN: 978-90-386-2031-2

Printed by University Press Facilities, Eindhoven, The Netherlands.

Cover design by An Prenen.

Voor de goede zorgen; aan mijn ouders
Aan An

Contents

Summary	v
<i>Samenvatting</i>	ix
1 Introduction	1
1.1 Background	1
1.2 Biological recognition using antibodies	2
1.3 Example: Pregnancy test	3
1.4 Magnetic biosensors	6
1.5 Functional biosensor	8
1.6 Outline of thesis	10
References	11
2 Magnetic forces and biological interactions	17
2.1 Introduction	18
2.2 Super-paramagnetism	18
2.3 Forces on molecules and small bodies in aqueous solution	22
2.4 Kinetics of biological bonds	26
References	29
3 On-chip detection of magnetic particles	31
3.1 Introduction	32
3.2 Magnetic biosensor	34
3.2.1 Sensor and readout electronics	34
3.2.2 Sensor response	36
3.3 Experimental	39
3.3.1 Setup	39
3.3.2 Image analysis	40
3.4 Results and discussion	41
3.4.1 Single particle detection	41
3.4.2 Detection of multiple particle transfers	45
3.5 Conclusion	50
References	50

4	Controlled pulling force on particles by magnetic field gradients	53
4.1	Introduction	54
4.2	Experimental	55
4.2.1	Design	55
4.2.2	Direct force measurements	58
4.3	Non-specific binding of protein coated particles	63
4.4	Conclusion	66
	References	66
5	Controlled torque on particles by rotating magnetic fields	69
5.1	Introduction	70
5.2	Experimental	70
5.2.1	On-chip crossed wires	70
5.2.2	Image analysis	72
5.3	Results and discussion	74
5.3.1	Low frequency actuation	74
5.3.2	High frequency actuation	83
5.3.3	Chemically coupled two-particle cluster	87
5.4	Conclusion	90
	References	90
6	Non-specific binding of particles studied by rotating magnetic fields	93
6.1	Introduction	94
6.2	Experimental	94
6.2.1	Quadrupole setup	94
6.2.2	Sample preparation and methods	98
6.3	Results and discussion	99
6.3.1	Influence of ionic strength	99
6.3.2	Influence of pH	101
6.3.3	Surface blocking with bovine serum albumin	103
6.4	Conclusion	105
	References	105
7	Torsional stiffness of a protein system: a feasibility study	109
7.1	Introduction	110
7.2	Rotational properties of bound particles	110
7.3	Experimental	112
7.4	Results and discussion	114
7.4.1	Permanent magnetic moment of M-270 particles	114
7.4.2	Sample preparation	116
7.4.3	Torsional stiffness of IgG-protein G couple	118
7.5	Conclusion	123
	References	123

List of publications	125
Acknowledgments/<i>dankwoord</i>	127
<i>Curriculum Vitae</i>	129

Magnetic particle actuation for functional biosensors

Summary

Molecular processes play a major role in the biology of the human body. As a consequence, molecular-level information can be very effectively used for medical diagnostics. In medical practice, samples of *e.g.* blood, urine, saliva, sputum, faeces or tissue are taken and investigated in specialized laboratories using a variety of biological tests. The tests can generally be separated into five process steps: (i) sample taking, (ii) sample preparation, (iii) specific recognition of the molecules of interest, (iv) transduction of the presence of the molecules into a measurable signal and (v) translation of the measured signal into a diagnostic parameter that can support the treatment of the patient. Particles with nanometer to micrometer sizes are widely used as carriers and labels in bio-analytical systems/assays. An important class of particles used in in-vitro diagnostics are so-called super-paramagnetic particles, which consist of magnetic nanoparticles embedded inside a non-magnetic matrix. The absence of magnetic material in biological samples allows a controlled application of magnetic fields. Super-paramagnetic particles are therefore powerful because they can be easily manipulated and reliably detected inside complex biological fluids. These properties are exploited in magnetic-label biosensors, which employ the magnetic particles as labels in order to measure the concentration of target molecules in a biological sample.

In this thesis we investigate techniques for a novel generation of biosensors - called functional biosensors - in which the concentration as well as a functional property of biological molecules can be determined by controlled manipulation of the magnetic particles. We demonstrate real-time on-chip detection and manipulation of single super-paramagnetic particles in solution. The chip-based sensor contains micro fabricated on-chip current wires and giant magneto resistance (GMR) sensors. The current wires serve to apply force on the particles as well as to magnetize the particles for on-chip detection. By simultaneously measuring the sensor signal and the position of an individual particle crossing the sensor, the sensitivity profile of the sensor was reconstructed and qualitatively understood from

a single-dipole model. The manipulation of multiple particles in parallel combined with real-time detection of single particles opens the possibility to perform on-chip high-parallel assays with single-particle resolution.

A practical drawback of on-chip magnetic actuation and detection is the limited amount of particles (typically several dozens) that can be studied in a single experiment. To study a large number of particles (typically several hundreds) without hydrodynamic and magnetic particle-to-particle interactions, a magnetic tweezers setup is designed and built to apply translational pulling forces to magnetic particles. The magnetic tweezers setup is based on an electromagnet combined with an optical microscope for the detection of the particles. Using this setup the non-specific binding of protein coated particles to a glass substrate is measured for various buffer conditions. The increase of binding with increasing ionic strength is understood from the electrostatic interaction between the particles and the glass substrate.

A complementary way to probe biological molecules or interactions is by applying a controlled torsion, *i.e.* a controlled rotation under well-defined torque. Particle-based single-molecule experiments described in literature already indicate novel types of assays enabled by the application of rotation to biological molecules. Although the degree of rotation was known in these single-molecule experiments, the quantitative value of the applied torque was not controlled. In fact, it is a surprise that a torque can be applied because in an idealized super-paramagnetic particle, the angle difference between the induced magnetization and the applied magnetic field is zero and thus the torque should be zero as well.

To answer the question which physical mechanism is responsible for torque generation, a rotating magnetic field was applied to single super-paramagnetic particles by on-chip current wires. We unraveled the mechanisms of torque generation by a comprehensive set of experiments at different field strengths and frequencies, including field frequencies many orders of magnitude higher than the particle rotation frequency. A quantitative model is developed which shows that at field frequencies below 10 Hz, the torque is due to a permanent magnetic moment in the particle of the order of 10^{-15} Am². At high frequencies (kHz - MHz), the torque results from a phase lag between the applied field and the induced magnetic moment, caused by the non-zero relaxation time of magnetic nanoparticles in the particle.

A magnetic quadrupole setup is developed to upscale the rotation experiments to multiple particles in parallel. The advantage of the rotation experiments over the pulling experiments is that rotation experiments not only give information on dissociation but also on association processes. Using the quadrupole setup, the non-specific binding between protein coated particles and a glass substrate is measured for various buffer conditions. The increase of binding with increasing ionic strength and decreasing pH is understood from the electrostatic interaction between the particles and the glass substrate. When coating the glass substrate with bovine serum albumin (BSA), the non-specific binding of streptavidin coated

particles is strongly reduced. Although the blocking effect of BSA is not fully understood, our measurements clearly show the feasibility of rotational excitation of particles to probe molecular interactions.

Finally, we studied the feasibility of rotational actuation of magnetic particles to measure the torsional stiffness of a biological system with a length scale of several tens of nanometers. As a model system we used protein G on the particles that binds selectively to the crystallisable part of the IgG antibody that is physically adsorbed on a polystyrene substrate. The angular orientation of the particles that are bound to the substrate show an oscillating behavior upon applying a rotating magnetic field. The amplitude of this oscillation decreases with increasing anti-body concentration, which we attribute to the formation of multiple bonds between the particle and the substrate. By evaluating the details of the oscillatory behavior, we found a lower limit of the torsional modulus of the IgG-protein G complex of $6 \cdot 10^{-26} \text{ Nm}^2$. The torsional modulus is two orders of magnitude larger than typical values found in literature for DNA strands. A difference in torsional modulus is expected from the structural properties of the molecules *i.e.* DNA is a long and flexible chain-like molecule whereas the protein G and IgG molecules are more globular due to the folding of the molecules.

Actuatie van magnetische deeltjes voor functionele biosensoren

Samenvatting

In het menselijke lichaam spelen zich veel biologische processen af op moleculair niveau. Daarom wordt in de medische diagnostiek veel gebruik gemaakt van moleculaire informatie. In de praktijk worden in gespecialiseerde laboratoria biologische tests uitgevoerd op biologisch materiaal zoals bloed, urine, speeksel of weefsel. Zo'n biologische test bestaat uit 5 kenmerkende stappen: (i) nemen van het monster, (ii) voorbereiden van het monster, (iii) specifieke herkenning van de te detecteren moleculen, (iv) omzetten van deze herkenning in een meetbaar signaal en (v) vertalen van het gemeten signaal naar een klinisch relevante parameter. Tegenwoordig wordt er in bio-analytische systemen veel gebruik gemaakt van nano- en microdeeltjes als drager en als label. Een veelgebruikt type deeltjes voor diagnostische tests is de groep van de zogenaamde super-paramagnetische deeltjes. Deze bestaan uit magnetische nanodeeltjes in een niet magnetische polymeer matrix. Door de afwezigheid van magnetisme in biologisch materiaal, is het gecontroleerd aanleggen van magnetische velden mogelijk. Het grote voordeel van het gebruik van magnetische deeltjes is dat deze eenvoudig gemanipuleerd en gedetecteerd kunnen worden in complexe biologische vloeistoffen. Zogenaamde magnetische-label biosensoren maken gebruik van deze specifieke eigenschappen voor het meten van de concentratie van specifieke moleculen in een biologische vloeistof. De magnetische deeltjes worden hierbij als een label aan de te detecteren moleculen gebonden.

In dit proefschrift onderzoeken we nieuwe technieken die gebruikt kunnen worden voor de volgende generatie biosensoren, de zogenaamde functionele biosensoren. Hierin kunnen naast de concentratie ook functionele eigenschappen van biologische moleculen onderzocht worden met behulp van de gecontroleerde magnetische manipulatie van de deeltjes. In een van onze experimenten hebben we gebruik gemaakt van sensor chips met stroomdraden en zogeheten GMR sensoren. De stroomdraden worden gebruikt zowel om krachten op de deeltjes uit te oefenen als om de deeltjes te magnetiseren voor de detectie. Het gevoeligheidsprofiel van

de sensor werd bepaald door gelijk-tijdig het sensor signaal en de positie van een individueel deeltje te meten. Het gemeten profiel wordt kwalitatief beschreven met een model gebaseerd op het veld van een magnetische punt-dipool. De gelijk-tijdige manipulatie van meerdere deeltjes in combinatie met real-time detectie van individuele deeltjes maakt het in principe mogelijk om op een chip biologische assays uit te voeren.

Locale actuatie en detectie op een chip bleken in het onderzoek een groot nadeel te hebben: de beperkte hoeveelheid statistiek, een gevolg van het kleine aantal deeltjes (enkele tientallen) dat gebruikt kan worden in een experiment op een chip. Om een groter aantal deeltjes te kunnen actueren en detecteren werd een zogenaamde magnetische pincet opstelling ontworpen en gebouwd. Het magnetisch pincet is gebaseerd op een elektromagneet, gecombineerd met een optische microscoop voor de detectie van de deeltjes. In deze opstelling wordt de magnetische kracht over een groot oppervlak aangelegd, zodat zelfs bij een groot aantal deeltjes (enkele honderden) de hydrodynamische en magnetische interacties tussen deeltjes onderling verwaarloosbaar zijn. De niet-specifieke binding tussen proteïne gecoate deeltjes en een glazen substraat werd met behulp van deze opstelling bestudeerd voor verschillende eigenschappen van de buffer. Bij een toenemende ionische sterkte van de buffer blijkt een toenemend aantal deeltjes aan het substraat te binden. Dit kan worden verklaard vanuit de elektrostatistische interactie tussen de deeltjes en het glazen substraat.

Naast het aanleggen van translationele krachten, kan het gecontroleerd aanleggen van een draaimoment extra informatie verschaffen over eigenschappen van moleculen. Het voordeel van het aanleggen van een draaimoment ten opzichte van het aanleggen van een translationele kracht is dat in rotatie experimenten naast dissociatie processen, ook associatie processen bestudeerd kunnen worden. Onderzoek aan individuele moleculen, zoals beschreven in recente literatuur, laten nieuwe analysetechnieken zien die gebaseerd zijn op de rotatie van biologische moleculen. In tegenstelling tot de verdraaiing van de moleculen, was het aangelegde draaimoment niet kwantitatief bekend in deze experimenten. Het kan zelfs wonderlijk genoemd worden dat een draaimoment kan worden aangelegd, want de hoek tussen het geïnduceerde magnetische moment van een ideaal super-paramagnetisch deeltje en het aangelegde veld is nul en zodoende zou het draaimoment ook nul moeten zijn.

Om te onderzoeken welk fysisch principe aan de basis ligt van het draaimoment op het super-paramagnetisch deeltje, hebben we experimenten gedaan waarin een roterend magneetveld is aangelegd op een enkel deeltje door middel van een chip met kruisende stroomdraden. In een reeks experimenten waarbij de veldsterkte en de veldfrequentie gevarieerd werden, hebben we het principe achter het aanleggen van een draaimoment ontrafeld. Een kwantitatief model laat zien dat voor veldfrequenties lager dan 10 Hz, het draaimoment wordt veroorzaakt door een klein permanent magnetisch moment (ordegrootte 10^{-15} Am²) in het deeltje. Voor hoge veldfrequenties (kHz - MHz) is het draaimoment een gevolg van de

fase-achterstand tussen het geïnduceerde magnetische moment en het aangelegde veld. Deze fase-achterstand is een direct gevolg van de eindige relaxatietijd van de nanodeeltjes.

Voor het gelijktijdig roteren van meerdere deeltjes tijdens een experiment werd een magnetische rotatie opstelling met vier elektromagneten ontwikkeld. Met behulp van deze opstelling is de niet-specifieke binding tussen proteïne gecoate deeltjes en een glazen substraat bestudeerd voor verschillende buffer condities. Bij afnemende pH en toenemende ionische sterkte van de buffer neemt het aantal deeltjes toe dat bindt aan het substraat. Dit kan opnieuw worden verklaard door de elektrostatische interactie tussen de deeltjes en het glazen substraat. De niet-specifieke binding van deeltjes aan het substraat neemt sterk af wanneer het substraat bedekt is met BSA. Hoewel deze afname van de binding niet volledig begrepen is, tonen onze metingen aan dat rotationele actuaties gebruikt kan worden om moleculaire interacties te onderzoeken.

Tenslotte hebben we de toepasbaarheid van rotationele actuaties onderzocht voor het meten van de torsiestijfheid van een biologisch systeem met een afmeting van enkele tientallen nanometers. Het gebruikte modelsysteem bestaat uit deeltjes bedekt met proteïne G. Dit bindt specifiek aan het kristalliseerbare gedeelte van IgG antilichamen die zijn geabsorbeerd aan een polystyreen substraat. De hoekverdraaiing van de deeltjes die gebonden zijn aan het substraat vertoont een oscillatie wanneer een roterend magneetveld wordt aangelegd. De amplitude van deze oscillatie neemt af met een toenemende concentratie van antilichamen op het substraat. Wij schrijven dit toe aan de vorming van meerdere bindingen tussen het deeltje en het substraat.

De torsiemodulus van het IgG-proteïne G complex werd bepaald door een gedetailleerde analyse van de waargenomen oscillaties. De gevonden torsiemodulus van $6 \cdot 10^{-26} \text{ Nm}^2$ is twee ordegrottes lager dan die van DNA zoals deze typisch in de literatuur gevonden wordt. Gezien het verschil in structurele eigenschappen tussen DNA en proteïne G, kon een verschil in torsiemodulus worden verwacht. DNA heeft een lange, flexibele keten-achtige structuur, terwijl de proteïne G en IgG moleculen een compacter en bolvormige structuur hebben door de vouwing van de moleculen.

Chapter 1

Introduction

1.1 Background

Molecular processes play a major role in the biology of the human body.^[1] As a consequence, molecular-level information can be very effectively used for medical diagnostics. In medical practice, samples of e.g. blood, urine, saliva, sputum, faeces or tissue are taken and investigated in specialized laboratories using a variety of biological tests. The tests can generally be separated into five process steps: (i) sample taking, (ii) sample preparation, (iii) specific recognition of the molecules of interest, (iv) transduction of the presence of the molecules into a measurable signal and (v) translation of the measured signal into a diagnostic parameter that can support the treatment of the patient.^[2] Depending on the complexity and priority of the test, it can take hours up to several days for a result to arrive at the physician. One of the technological trends is that more and more biological tests can be performed at the point of care (POC),^[3,4] i.e. close to the patient, which allows a smooth integration of the testing into the medical workflow. The research field dealing with the miniaturization and integration of molecular-level biological tests into high-performance devices is called lab-on-a-chip.^[5-7] The integration of a complete biological test into a small, easy to use, reliable and cost-effective cartridge is scientifically and technologically very challenging. Completely new concepts are required for the manipulation of fluids and biological molecules, the integration of sample pretreatment steps, the integration of biological materials, the generation and transduction of signals, and the fabrication of devices. One of the approaches to facilitate the integration of a biological test is by using magnetic particles. Magnetic particles can be used to (i) efficiently capture biological molecules from solution, (ii) transport and concentrate molecules using magnetic forces, (iii) label molecules for detection, (iv) make a distinction between bound and unbound particles using magnetic forces, and (v) apply controlled forces to molecules in order to investigate their properties. These properties are being exploited in investigations on novel generations of POC sensors.^[8-11]

An example of a situation in which a patient can benefit from such a POC sensor is:

Chest pain^[12] is a symptom of a number of life threatening cardiac conditions but also of a harmless pain on the muscles between the ribs or even hypochondria. So when a patient with chest pain visits his general practitioner, the doctor will try to find the cause of the pain. When a life threatening cardiac condition is suspected, he will send the patient to a hospital for emergency care. If the doctor does not suspect such an acute condition, but can not rule out an oncoming cardiac problem, he can decide to take a blood sample and send it to a laboratory for a troponin test.^[13] Some subtypes of the troponin proteins are markers for damage to the heart muscle and an increase of troponin concentration can point to an immanent cardiac condition. When the test results arrive after several days, the general practitioner can advise the patient to visit a hospital for further examination if the results give rise to concern. But during the days it takes for the results to arrive, the patient is still concerned about his health state. In the worse case scenario the patient might even die before the test results arrive. With a point-of-care sensor for troponin the general practitioner can immediately test and reassure the patient, without as a precautionary measure, sending all patients with chest pain to the hospital.

In the tests used by central laboratories, the biological recognition of the molecule of interest is often done by means of antibodies in a so-called immunoassay. In this chapter the biological recognition of antigens using antibodies is explained. The home-pregnancy test is used as an illustrative example of a POC sensor based on the recognition by antibodies. Finally the magnetic biosensor and its extension towards a functional biosensor is discussed.

1.2 Biological recognition using antibodies

Organisms have an immune system that protects them against disease by identifying and killing pathogens and tumor cells for example. In this constantly adapting system of biological processes, antibodies play a major role in the primary detection of antigens. Antibodies also called immunoglobulins (abbreviated Ig) are proteins with a configuration which is often depicted as Y-shaped (Fig. 1.1). The antibody has two identical parts each of which consists of a heavy chain and a shorter so called light chain. The tips of the Y, called the antigen binding fragment (Fab), are composed of one constant and one variable domain from the heavy as well as from the light chain. The paratope is formed by the variable domains at the end of the Fab fragment and binds specifically to a certain part of the antigen,

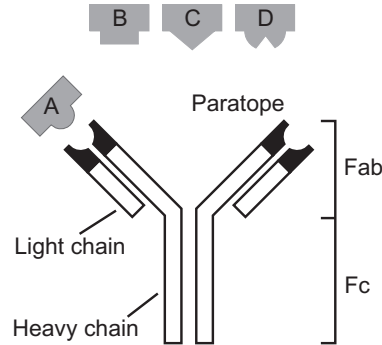


Fig. 1.1: Schematic representation of an antibody (Y-shape) that binds specific to a particular antigen (A). The variable part of the heavy chain and the variable part of the light chain (indicated by the black regions) form the binding site of the antibody called paratope. The antigens B, C and D will only bind selectively to an antibody with a different paratope.^[14]

the so called epitope. The specific affinity to the epitope of the antigen arises from a unique three dimensional topology and a combination of *e.g.* hydrogen bonds, electrostatic and van der Waals interactions. The base of the Y is called the crystallisable region (Fc) and is composed of two heavy chains. This part of the antibody plays a role in modulating immune cell activity by binding to specific proteins and cell receptors. After the recognition, a pathogen is disposed of in a cascade of biological processes in a dynamic network of proteins, cells, organs and tissue.

Since antibodies are so powerful and selective in the detection of antigens, antibodies are nowadays harvested from various life forms to be used for the biological recognition in so called immunoassays.^[14] Immunoassays are used in centralized labs for the screening and detection of diseases from various samples. Alternatively, immunoassays are available as point-of-care and home testing kits.

1.3 Example: Pregnancy test

A widely available (at the local pharmacy and even in supermarkets) home testing kit based on an immunoassay is the pregnancy test.^[15] After nidation *i.e.* a fertilized ovum implants in the uterus wall, the placenta starts developing and begins to release a hormone called human Chorionic Gonadotropin (hCG) into the blood. Some of this hCG is also excreted in the urine.

In the first few weeks of pregnancy, the average amount of hCG in the urine rises rapidly and reaches a maximum after 10 weeks (Fig. 1.2). The goal of the pregnancy test is to measure the amount of hCG in the urine and conclude from this whether or not a fertilized ovum has implanted.

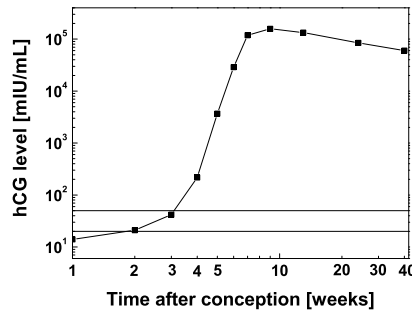


Fig. 1.2: The average level of hCG in the urine versus time after conception in weeks.^[16] The detection limit for commercial available tests lies between 10 mIU/mL and 50 mIU/mL (horizontal lines). For hCG, 25 mIU/mL corresponds to a concentration of 100 pM.*

For testing (Fig. 1.3), the urine containing hCG is absorbed by the material of the testing strip and a dried label-antibody conjugate ($Ab\beta$) is dissolved in the urine. While the mixture of the urine and conjugate travels further through the absorbent material, the antibody selectively binds to the β -subunit of the hCG. As soon as the mixture reaches the immobilized antibody ($Ab\alpha$) it selectively binds to the α -subunit of the hCG and by that the sandwich assay and the recognition of the molecule is completed. Note that the α -subunit is also present in other hormones whereas the β -subunit is unique for hCG which allows for selective detection of hCG without interference of other hormones.

The amount of label bound to the substrate of the sensor is a measure for the concentration of hCG in the urine. The presence of the molecule is converted in a signal by the label of the conjugate that produces a purple color band in the window. Finally the detection of the signal is done by the human eye. In case the test band stays colorless, one can conclude that there is no hCG present in the urine and the person is not pregnant. But it might also be that the test failed *e.g.* due to a error in the production process, decay of the device during long term storage or human error while testing the urine. Therefore the strip has an internal test to check the performance of the device. After the mixture reaches the testing band, the rest of the mixture continues flowing through the device and reaches the control zone. In this control zone, the label-antibody conjugate that has not

* In pharmacology the international unit (IU) is a measure for the amount of a certain substance *e.g.* hormones, vitamins, vaccines and medication based on its biological activity. The definition of one IU differs from substance to substance and is based on the measured activity in a substance specific standardized test *i.e.* one IU of a certain hormone is not equivalent with one IU of another hormone regarding weight or number of molecules. For hCG, 25 mIU/mL corresponds to a concentration of 100 pM.^[17]

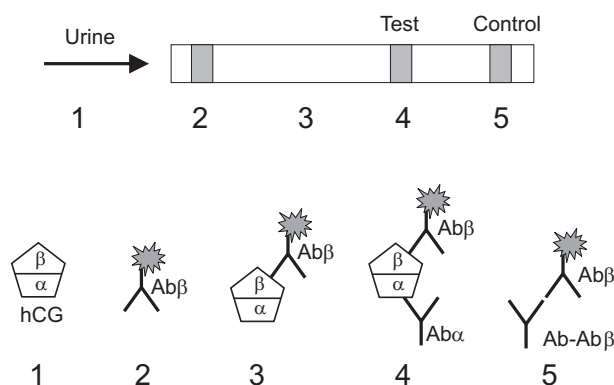


Fig. 1.3: **Top:** Test strip of a immunoassay for rapid qualitatively determination of human Chorionic Gonadotropin (hCG).^[15] The numbers indicate the location where the individual steps of the immunoassay take place. **Bottom:** Schematic representation of the immunoassay. (1) The urine is absorbed by the material of the testing strip. (2) The label-antibody conjugate ($Ab\beta$) is dissolved in the urine. (3) The antibody selectively binds to the β -subunit of the hCG. (4) The immobilized antibody ($Ab\alpha$) selectively binds to the α -subunit of the hCG and the label (e.g. gold nanoparticle) produces a purple color band. (5) The remaining mixture continues flowing through the absorbent device and reaches the control zone where the remaining label-antibody conjugate binds to another antibody ($Ab-Ab\beta$) and produces a purple color band demonstrating that the test was functioning correctly. Note that in absence of hCG only the control band becomes purple.

been bound to hCG selectively binds to another immobilized antibody ($Ab-Ab\beta$) and produces a purple color band demonstrating that the reagents completely ran through the device and that the test device was functioning correctly.

The pregnancy test contains all principles of a biosensor, but the test does not give a quantitative result on the concentration. Furthermore the detection limit is subject to inter-observer-variability *i.e.* it is difficult for the human eye and brain to accurately detect low amounts of label molecule in the colored band. Kits are available with different detection limits defined by the manufacturers: 50 mIU/mL (Clear blue^[18] and Predictor^[19]), 25 mIU/mL (Mat Care^[20] and Clearview^[21]) and 10 mIU/mL (Mat Care Ultra^[20]). With a more sensitive kit it is in principle possible to test shorter after ovulation (even before the first day of the missed menstrual period). Since nidation (6-12 days post ovulation) needs to occur before hCG is produced, a test might give a false negative on pregnancy (not on hCG level) due to the low level of hCG (Fig. 1.2) where women that are in a fertility program, might get a false positive on pregnancy because of a high level of hCG due to hCG-injections.

Nowadays tests based on the same lateral-flow principle as the pregnancy test are being developed or already available to test for all kinds of diseases like Chlamy-

dia, Streptococcal and even HIV.^[18] With the development of more home-testing kits, the reliability of the tests and also ethical questions on free access to such tests (e.g. via internet) and proper professional support become more and more important.

Depending on the type of test, even more parameters are of interest for a POC biosensor *e.g.* unit price, time it takes to perform a test, amount and availability of the body fluid (blood, saliva, urine), reliability under broad environmental conditions.

For example in the pregnancy test, a low detection limit is only of interest for early testing since the hCG concentration remains high during the pregnancy (Fig. 1.2) whereas for an ovulation test^[22] that measures the presence of the Luteinizing Hormone (LH) in urine, it is more important to have a low detection limit. The LH level increases dramatically prior to a women's most fertile day of the month in a process commonly referred to as the "LH Surge". This surge then triggers the release of an ovum from woman's ovary (ovulation). The LH level increases rapidly within a few days and after reaching a maximum (typically 45 mIU/mL), the level rapidly decreases to normal level (typically 5 mIU/mL). Since the level of LH in urine only exceeds the detection limit (25 mIU/mL) during one day, the LH test has to be conducted at least once a day and preferably even two or three times a day in order not to miss the surge. A lower detection limit will make the test less time critical *i.e.* the level of LH exceeds the detection limit for a longer period of time.

1.4 Magnetic biosensors

The lateral-flow home-testing kits discussed in the previous section all use an antibody-label conjugates that produce a colored band and the final detection of this band is performed by the human eye. This concept allows to produce a low cost, easy to use, point-of-care biosensor but also puts limits on the application of this principle. First of all, a certain number of label-molecules have to bind before the presence of the colored band can be positively identified by the human eye which puts a limit on the detection sensitivity. Furthermore the test does not directly give a quantitative result on the concentration of the antigen due to inter-observer-variability *i.e.* it is difficult for the human eye and brain to accurately detect and interpret the amount of label molecule in the colored band. A way to make the sensor quantitative and more sensitive is by adding electronics to the device which perform the detection and interpretation of the results and display the outcome in a user-friendly way *e.g.* on a small screen.

Several labels can be used for biosensing, *e.g.* fluorescent molecules, radioactive isotopes, enzymes, nano- and microparticles.^[14] Since a number of years biosensors are being investigated which use super-paramagnetic particles (nm to μm size) as labels. The particles consist of magnetic nanoparticles embedded inside a non-magnetic matrix.^[24] Figure 1.4a shows a schematic representation of a mag-

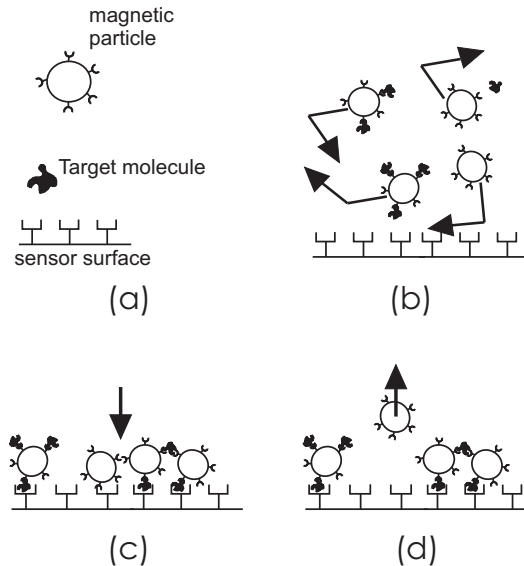


Fig. 1.4: Schematic representation of a magnetic biosensor assay.^[23] (a) The surface of the sensor as well as the magnetic particles are coated with antibodies. The antibodies bind specifically to (different parts) of the target molecule. (b) The magnetic particles are moved by magnetic fields through the fluid to capture target molecules. (c) After a certain amount of time the particles are pulled downwards and the magnetic particles bind to the surface of the sensor. (d) Finally the unbound particles are removed from the surface and the remaining number of magnetic particles is determined which gives a measure for the concentration of the target molecule in the solution.

netic biosensor assay wherein the target molecule becomes sandwiched between the magnetic particle and the sensor surface. The amount of labels bound to the surface is a measure for the concentration of the target molecule. It is particularly advantageous to detect magnetic labels in a chip-based device, because of the integration and miniaturization potential.

Furthermore the biological fluids are hardly magnetic, so magnetic fields can be reliably applied and the magnetic particles can easily be detected, which allows for a low detection limit. Detection of magnetic labels has been demonstrated using magneto-resistive sensors,^[8,9,25–28] Hall sensors,^[29–33] field coils^[34,35] and by optical detection.^[36–38]

The magnetic particles offer another particularly interesting option: by moving the labels coated with antibodies through the fluid,^[23] the labels can efficiently catch the antigen from the fluid (Fig. 1.4b). Once the antigen is bound, the labels can be pulled down towards the sensor surface where they bind due to the formation of the sandwich format (Fig. 1.4c). Finally the unbound labels are

pulled away by magnetic forces and the number of magnetic particles is measured (Fig. 1.4d). Using these actuation concepts, the assay can be integrated and accelerated and picomolar detection limits are achievable for fast (< 10 min) POC sensor applications.^[10, 11, 23, 28]

1.5 Functional biosensor

Because forces can be applied to the magnetic labels, the concept of the magnetic biosensor can be extended towards a functional biosensor. The goal of a functional biosensor is to unveil a functional property of the biological system *e.g.* stiffness of the target molecule, nonspecific interactions between proteins and surfaces or the affinity between antibody-antigen^[14] in addition to the concentration of a target molecule.

An example of how a functional biosensor might be used:

Staphylococcus Aureus (SA) is a strain of bacteria which is normally found on the skin and mucosae of humans and animals. Once the bacteria penetrates the skin and/or infects a wound, the toxins excreted by the bacteria can cause life threatening conditions such as toxic shock syndrome, especially for persons with a weakened health state or with a suppressed immune system. Normally an infection with SA can be treated with a variety of antibiotics but some types of SA like Methicillin-Resistant *Staphylococcus Aureus* (MRSA) have become resistant to a large group of antibiotics. Therefore alternative therapies against infections need to be developed and a potential alternative is based on antibodies in the form of immuno-therapeutics.^[39] The antibodies used in such therapies can for example be harvested from cow milk as already happens for the treatment of diarrhoea caused by *Clostridium difficile* infection.^[40, 41] After infecting lactating cows with an inactivated strain of bacteria, antibodies against this strain are produced which are also secreted into the milk. In short, the goal is to produce large amounts of antibodies that are very selective for the intended antigen and show a high affinity to it. Since the amount produced as well as the affinity varies between individual cows and even in time, it becomes necessary to measure the quantity as well as the quality of the antibodies. Nowadays these tests are done in specialized labs but in the future it might be possible that the farmer regularly tests the milk of individual cows by using a functional biosensor.

In the past decades, single molecule DNA strands have been studied using magnetic and optical tweezers and atomic force microscopy (AFM) where each of the techniques has its particular field of application.^[42, 43] Magnetic tweezers techniques allow highly parallel single-molecule experiments which is difficult to

achieve with optical tweezers and even impossible with AFM techniques. Another advantage of magnetic and optical tweezers is the ability of 3D manipulation and even the application of a torque, whereas AFM techniques lack the ability to apply a torque. An advantage of optical tweezers and AFM techniques is the high spatial (several nm) and temporal (several kHz) resolution that can be achieved.^[42] The main advantage of magnetic tweezers is that forces can be applied non-invasively since the magnetic field is exquisitely selective for the magnetic label and has no direct interaction with the biological system. Optical tweezers lack this selectivity and as a consequence, the force that can be applied is limited by the amount of power that is dissipated in the system which causes photoaging and absorption induced heating of the biological system. Using magnetic tweezers various properties of DNA have been studied in single molecule studies *e.g.* stretching under force,^[44] DNA condensation^[45] and interaction with Topoisomerase.^[46] The limited statistics in single molecule tweezers experiments are overcome by repeating the experiments, which is feasible in a research environment but limits the application of the techniques in a sensor.

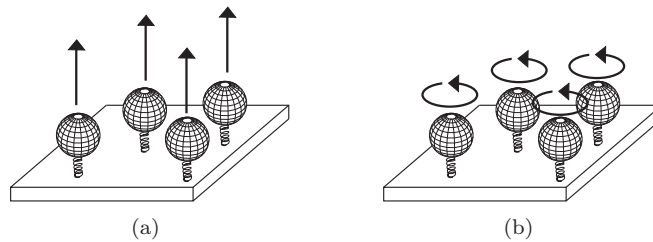


Fig. 1.5: Once the magnetic labels are bound to the surface of the sensor, forces can be applied to the biological system either by: (a) pulling on the labels or (b) applying a torque on the labels.

The important advantage of magnetic tweezers is the possibility to perform multiple experiments in parallel *i.e.* apply forces on multiple magnetic particles (Fig. 1.5a). Consequently, multiple single molecule systems can be probed at the same time which allows to retrieve statistically reliable results from a single measurement. The rate of irreversible dissociation of biological bonds under force has been measured with magnetic tweezers using multiple particles in a single experiment.^[47–49] In these experiments the forces were applied using permanent magnets^[47,48] or on-chip current wires.^[49] Another advantage of magnetic labels is the ability to rotate them *i.e.* apply a torque with a magnetic field (Fig. 1.5b). Magnetic tweezers based on the rotation of magnetic particles have been used to study properties of DNA.^[45,46,50] Although the degree of rotation was known in these single-molecule experiments, the quantitative value of the applied torque was not controlled. Recent experiments show the possibility to measure the applied

torque by studying thermal fluctuations in angular orientation of the magnetic particle.^[51] The technique allows to measure the applied torque in a static situation using a probe system of a magnetic particle and a nanorod.

In this thesis we will present methods for the detection and manipulation of magnetic particles. The goal is to develop new methods that have single molecule sensitivity but allow to study multiple molecules in parallel to obtain statistically relevant information. The properties of the biological system are obtained by studying the response of the magnetic particles upon applying a magnetic field. The actuation principles can be divided in two area's: rotation of and pulling on magnetic particles.

1.6 Outline of thesis

Chapter 2 starts with the description of the magnetic properties of the particles that are used in the experiments. Furthermore the forces on these particles are summarized using the Derjaguin-Landau-Verwey-Overbeek-theory (DLVO).^[52] In **chapter 3**, single particle detection and manipulation of magnetic particles with a diameter of 1 μm and 2.8 μm are quantified and compared to a theoretical model.

In **chapter 4** the development of a magnetic pulling setup based on an electromagnet is described. The force on the magnetic particles is measured directly from the speed of the particles moving through the fluid. As a demonstration of the feasibility of this technique, the non-specific binding of protein coated particles to a glass substrate is studied for varying ionic strength of the fluid. The results are quantitatively understood from a model based on the DVLO-theory.

In **chapter 5** we show how a well-defined torque can be applied on super-paramagnetic particles. The rotating magnetic fields are applied by on-chip current wires which allow a detailed study of the rotation of the particles. We unravel the mechanisms of torque generation by a comprehensive set of experiments at different field strengths and frequencies, and develop a quantitative model to calculate the magnetic torque on super-paramagnetic particles.

In **chapter 6** we present a new technique to continuously measure the binding and unbinding of magnetic particles. The discrimination between the bound and unbound state is made by rotation of the particles. Since the unbound particles stay on the surface, the full binding behavior can be measured over time in a single measurement using a single sample. We show the feasibility of this novel technique by measuring the non-specific binding of streptavidin coated particles on a glass surface under varying conditions e.g. ionic strength, pH and BSA coating of the substrate.

In **chapter 7** we show how rotational actuation of magnetic particles can be used to measure the torsional stiffness of a biological system with a typical length scale of several tens of nanometers. As a model system we use protein G on the particles that binds selectively to the crystallisable part of the IgG antibody that is present on a polystyrene substrate.

References

- [1] B. Alberts, A. Johnson, J. Lewis, M. Raff, K. Roberts, and P. Walter. *Molecular Biology of the Cell*. Garland, 4 edition, 2002.
- [2] C.A. Burtis, E.R. Ashwood, and D.E. Bruns. *Tietz Textbook of Clinical Chemistry and Molecular Diagnostics*. Elsevier.
- [3] A.J. Tüdös, G.A.J. Besselink, and R.B.M. Schasfoort. Trends in miniaturized total analysis systems for point-of-care testing in clinical chemistry. *Lab on a Chip*, 1:83–95, 2001.
- [4] S. A. Soper, K. Brown, A. Ellington, B. Frazier, G. Garcia-Manero, V. Gau an S.I. Gutman, D.F. Hayes, B. Korte, J.L. Landers, D. Larson, F. Ligler, A. Majumdar, M. Mascini, D. Nolte, Z. Rosenzweig, J. Wang, and D. Wilson. Point-of-care biosensor systems for cancer diagnostics/prognostics. *Biosensors and Bioelectronics*, 21:1932–1942, 2006.
- [5] A. van den Berg and T.S.J. Lammerink. in *Microsystem Technology in Chemistry and Life Sciences*, pages 21–50. editor: A. Manz and H. Becker. Springer, Berlin, 1999.
- [6] P. Yager, T. Edwards, E. Fu, K. Helton, K. Nelson, M.R. Tam, and B.H. Weigl. Microfluidic diagnostic technologies for global public health. *Nature*, 442, 2006.
- [7] F.B. Myers and L.P. Lee. Innovations in optical microfluidic technologies for point-of-care diagnostics. *Lab on a Chip*, 8:2015–2031, 2008.
- [8] D.R. Baselt, G.U. Lee, M. Natesan, S.W. Metzger, P.H. Sheehan, and R.J. Colton. A biosensor based on magnetoresistance technology. *Biosensors and Bioelectronics*, 13:731–739, 1998.
- [9] J.C. Rife, M.M. Miller, P.E. Sheehan, C.R. Tamanah, M. Tondra, and L.J. Withman. Design and performance of GMR sensors for the detection of magnetic microbeads in biosensors. *Sensors and Actuators A*, 107:209–218, 2003.
- [10] W.U. Dittmer, P. de Kievit, M.W.J. Prins, J.L.M. Vissers, M.E.C. Mersch, and M.F.W.C. Martens. Sensitive and rapid immunoassay for parathyroid hormone using magnetic particle labels and magnetic actuation. *Journal of Immunological Methods*, 338:40–46, 2008.
- [11] M. Koets, T. van der Wijk, J.T.W.M. van Eemeren, A. van Amerongen, and M.W.J. Prins. Rapid DNA multi-analyte immunoassay on a magnetoresistance biosensor. *Biosensors and Bioelectronics*, 24(7):1893–1898, 2008.

-
- [12] G.S. Hillis and K.A.A. Fox. Cardiac troponins in chest pain, can help in risk stratification. *British Medical Journal*, 319:1451–1452, 1999.
- [13] N. Curzen. Troponin in patients with chest pain. *British Medical Journal*, 329:1357–1358, 2004.
- [14] D. Wild. *The Immunoassay Handbook*. Elsevier, 3 edition, 2005.
- [15] *Consulted 2009: <http://www.healthtests.co.uk>.*
- [16] *Consulted 2009: <http://www.americanpregnancy.org/duringpregnancy/hcglevels.html>.*
- [17] K. Handschuh, J. Guibourdenche, V. Tsatsaris, M. Guesnon, I. Laurendeau, D. Evain-Brion, and T. Fournier. Human chorionic gonadotropin produced by the invasive trophoblast but not the villous trophoblast promotes cell invasion and is down-regulated by peroxisome proliferator-activated receptor- γ . *Endocrinology*, 148(10):5011–5019, 2007.
- [18] *Consulted 2009: <http://www.clearblue.info>.*
- [19] *Consulted 2009: <http://www.predictor.eu>.*
- [20] *Consulted 2009: <http://www.matcare.nl>.*
- [21] *Consulted 2009: <http://www.clearview.com>.*
- [22] *Consulted 2009: <http://www.ovulation-calculator.com/ovulation-tests.htm>.*
- [23] D.M. Bruls, T.H. Evers, J.A.H. Kahlman, P.J.W. van Lankvelt, M. Ovsyanko, E.G.M. Pelssers, J.J.H.B. Schleipen, F.K. de Theije, C.A. Verschuren, T. van der Wijk, J.B.A. van Zon, W.U. Dittmer, A.H.J. Immink, J.H. Nieuwenhuis, and M.W.J. Prins. Rapid integrated biosensor for multiplexed immunoassays based on actuated magnetic nanoparticles. *accepted for publication in Lab on a Chip*.
- [24] G. Fønnum, C. Johansson, A. Molteberg, S. Mørup, and E. Aksnes. Characterisation of Dynabeads by magnetization measurements and Mössbauer spectroscopy. *Journal of Magnetism and Magnetic Materials*, 293:41–47, 2005.
- [25] R. Wirix-Speetjes, W. Fyen, Jo. De Boeck, and G. Borghs. Single magnetic particle detection: Experimental verification of simulated behavior. *Journal of Applied Physics*, 99:103903, 2006.
- [26] B.M. de Boer, J.A.H.M. Kahlman, T.P.G.H. Janssen, H. Duric, and J. Veen. An integrated and sensitive detection platform for magneto-resistive biosensors. *Biosensors and Bioelectronics*, 22:2366–2370, 2007.
- [27] M. Megens, F. de Theije, B. de Boer, and F. van Gaal. Scanning probe measurements on a magnetic bead biosensor. *Journal of Applied Physics*, 102:014507, 2007.

-
- [28] M.W.J. Prins and M. Megens. *Chapter in Encyclopedia of Materials: Science and Technology*, volume doi: 10.1016/B978-008043152-9/02146-1. Elsevier, 2007.
- [29] P.A. Besse, G. Boero, M. Demierre, V. Pott, and R. Popovic. Detection of a single magnetic microbead using a miniaturized silicon Hall sensor. *Applied Physics Letters*, 80(22):4199–4201, 2002.
- [30] L. Ejsing, M.F. Hansen, A.K. Menon, H.A. Ferreira, D.L. Graham, and P.P. Freitas. Planar Hall effect sensor for magnetic micro- and nanobead detection. *Applied Physics Letters*, 84(23):4729–4731, 2004.
- [31] L. Ejsing, M.F. Hansen, A.K. Menon, H.A. Ferreira, D.L. Graham, and P.P. Freitas. Magnetic microbead detection using planar Hall effect. *Journal of Magnetism and Magnetic Materials*, 293:677–684, 2005.
- [32] H. Fukumoto, K. Takeguchi, M. Noruma, and H. Endo. Rapid and high sensitive bio-sensing system utilizing magnetic beads. *The 13th IEEE International Conference on Solid-state Sensors, Actuators and Microsystems*, pages 1780–1783, 2005.
- [33] T. Aytur, J. Foley, M. Anwar, B. Boser, E. Harris, and P.R. Beatty. A novel magnetic bead bioassay platform using a microchip-based sensor for infectious disease diagnosis. *Journal of Immunological Methods*, 314:21–29, 2006.
- [34] A.P. Astalan, F. Ahrentorp, C. Johansson, K. Larsson, and A. Krozer. Biomolecular reactions studied using changes in brownian rotation dynamics of magnetic particles. *Biosensors and Bioelectronics*, 19:945–951, 2004.
- [35] P.I. Nikitin, P.M. Vetoshko, and T.I. Ksenevich. New type of biosensor based on magnetic nanoparticle detection. *Journal of Magnetism and Magnetic Materials*, 311:445–449, 2007.
- [36] S.P. Mulvaney, C.L. Cole, M.D. Kniller, M. Malito, C.R. Tamanaha, J.C. Rife, M.W. Stanton, and L.J. Whitman. Rapid, femtomolar bioassays in complex matrices combining microfluidics and magnetoelectronics. *Biosensors and Bioelectronics*, 23:191–200, 2007.
- [37] T.Y. Morozova and V.N. Morozov. Force differentiation in recognition of cross-reactive antigens by magnetic beads. *Analytical Biochemistry*, 374:263–271, 2008.
- [38] L. Cohen-Tannoudji, E. Bertrand, J. Baudry, C. Robic, C. Goubault, M. Pellissier, A. Johner, F. Thalmann, N.K. Lee, C.M. Marques, and J. Bibette. Measuring the kinetics of biomolecular recognition with magnetic colloids. *Physical Review Letters*, 100:108301, 2008.

-
- [39] M.J. Tempelmans Plat-Sinnige, N.J. Verkaik, W.J.B. van Wamel, N. de Groot, D.S. Acton, and A. van Belkum. Induction of *Staphylococcus aureus*-specific IgA and agglutination potency in milk of cows by mucosal immunization. *Vaccine*, 2009.
- [40] *MucoVax BV founded in 1998, is a bio-medical company, based in Leiden, The Netherlands, and specialised in the development and production of milk based anti-body therapies for the prevention and treatment of gastro-intestinal infections in humans as well as in animals.*
- [41] J.T. van Dissel, N. de Groot, C.M.H. Hensgens, S. Numan, E.J. Kuijper, P. Veldkamp, and J. van 't Wout. Bovine antibody-enriched whey to aid in the prevention of a relapse of clostridium difficile associated diarrhoea: preclinical and preliminary clinical data. *Journal of Medical Microbiology*, 54:197–205, 2005.
- [42] K.C. Neuman and A. Nagy. Single-molecule force spectroscopy: optical tweezers, magnetic tweezers and atomic force microscopy. *Nature Methods*, 5(6):491–505, 2008.
- [43] U. Bockelmann. Single-molecule manipulation of nucleic acids. *Current Opinion in Structural Biology*, 14:368–373, 2004.
- [44] C. Gosse and V. Croquette. Magnetic tweezers: Micromanipulation and force measurement at the molecular level. *Biophysical Journal*, 82:3314–3329, 2002.
- [45] K. Besteman, S. Hage, N.H. Dekker, and S.G. Lemay. Role of Tension and Twist in Single-Molecule DNA Condensation. *Physical Review Letters*, 98(5):058103, 2007.
- [46] D.A. Koster, K. Palle, E.S.M. Bot, M.A. Bjornsti, and N.H. Dekker. Antitumour drugs impede DNA uncoiling by topoisomerase I. *Nature*, 448:213–217, 2007.
- [47] H. Shang, P.M. Kirkham, T.M. Myers, G.H. Cassell, and G.U. Lee. The application of magnetic force differentiation for the measurement of the affinity of peptide libraries. *Journal of Magnetism and Magnetic Materials*, 293:382–388, 2005.
- [48] H. Shang and G.U. Lee. Magnetic Tweezers Measurement of the Bond Lifetime-Force Behavior of the IgG-Protein A Specific Molecular Interaction. *Journal of the American Chemical Society*, 129(20):6640–6646, 2007.
- [49] M. Panhorst, P.B. Kamp, G. Reiss, and H. Brückl. Sensitive bondforce measurements of ligand-receptor pairs with magnetic beads. *Biosensors and Bioelectronics*, 20:1685–1689, 2005.

-
- [50] D.A. Koster, V. Croquette, C. Dekker, S. Shuman, and N.H. Dekker. Friction and torque govern the relaxation of DNA supercoils by eukaryotic topoisomerase IB. *Letters to Nature*, 434:671–674, 2005.
- [51] A. Celedon, I.M. Nodelman, B. Wildt, R. Dewan, P. Searson, D. Wirtz, G.D. Bowman, and S.X. Sun. Magnetic tweezers measurement of single molecule torque. *Nano Letters*, 9(4):1720–1725, 2009.
- [52] D. Leckband and J. Israelachvili. Intermolecular forces in biology. *Quarterly Reviews of Biophysics*, 34(2), 2001.

Chapter 2

Magnetic forces and biological interactions

This chapter contains the theoretical background of super-paramagnetism and non-specific physical interactions between objects in aqueous solutions. Super-paramagnetism is a form of magnetism that is observed in material composed of small ferromagnetic nanoparticles. The main characteristic of a super-paramagnetic material is that its magnetization in absence of an external field is rapidly randomized by thermal energy i.e. the material has zero magnetization in absence of an applied field. The magnetization curve is measured of the different types of magnetic particles used in the experiments described in this thesis. During the experiments the particles are in an aqueous solution and subject to magnetic forces, hydrodynamic forces and physicochemical forces. We summarize the effects of the van der Waals and the electrostatic forces following the work of Leckband and Israelachvili. Finally we describe the binding/unbinding reactions of biological systems (such as antibody-antigens couples) by the reaction between two components that form a complex in a dynamic equilibrium.

2.1 Introduction

An important class of particles used for in-vitro diagnostics^[1] are so-called super-paramagnetic particles (nm to μm size), which consist of a non-uniform composite material of magnetic nanoparticles embedded inside a non-magnetic matrix.^[2] Particles with a biologically functionalized surface were designed for the separation and upconcentration of bio-material.^[1] For these applications, the particles are mixed with a complex biological fluid *e.g.* serum, saliva, urine or cell lysate in a test tube. During stirring, the molecules of interest bind specifically to the functionalized surface of the particles. Subsequently, the particles are pulled to the bottom of the tube by magnetic fields (often by using a permanent magnet) and the supernatant fluid is removed. By resuspending the particles in another fluid and repeating the separation process several times, all the original fluid can be replaced. The molecule of interest is generally released from the particles by breaking the biological bonds between the particle and the molecule, for example by changing the conditions of the fluid (*e.g.* pH, ionic strength). Finally the particles (now without the molecule of interest) are pulled to the bottom and the supernatant fluid containing the purified molecule is ready for further use.

The important property that allows this manipulation is the fact that the particles do not have a magnetic moment in absence of an applied field. If the particles would have a magnetic moment, they would form large clusters as a result of magnetic dipole-dipole attraction. Once the particles are magnetized by the external magnetic field, a gradient in this applied field will apply a force on the particle pulling them to the bottom of the test tube. After the magnetic field is switched off, clusters that have formed fall apart due to the thermal motion of the particles, so that the particles can be resuspended. The same properties that allow the separation/upconcentration of biological molecules also make the particles suitable as label in a biological assay.

In this chapter we first explain the theory of super-paramagnetism in more detail. In view of the intended application of forces on particles in immunoassays, the magnetic response of an ensemble of particles upon applying a magnetic field is measured using a vibrating sample magnetometer (VSM). The interactions between colloidal particles and surfaces in an aqueous environment are discussed in terms of Van der Waals and electrostatic forces. Finally we describe the binding/unbinding kinetics of biological systems (such as antibody-antigen couples) by the reaction between two components that form a complex in a dynamic equilibrium using the Law of Mass Action.

2.2 Super-paramagnetism

Usually a piece of magnetic material consists of several magnetic domains, regions with a uniform magnetization.^[3] Domain walls in which the magnetization gradually changes its direction separate the domains in this multi-domain state. The

existence of domains is induced by the system minimizing its magnetostatic energy. If the dimensions of the system are smaller than a critical size, no domain walls are formed because the magnetostatic energy that is freed by the formation of a domain wall is smaller than the energy needed to form the domain wall. For magnetite this single-domain state can be obtained below a typical size of several tens of nanometers.^[4]

The magnetization in the domains can have one or more preferred directions due several types of the magnetic anisotropy: magnetocrystalline, shape and surface anisotropy.^[5] The direction in which the domain is easy to magnetize is called the easy axis. A single domain nanoparticle with an uniaxial anisotropy can have its magnetization directed in two equivalent but opposite directions along the easy axis.

The state that is occupied at a given moment in time depends on the history and is preserved by the anisotropy barrier.^[6] For a given finite temperature, the thermal fluctuations enable to overcome the energy barrier resulting in a average lifetime of the magnetic state τ_m given by:

$$\tau_m = \frac{1}{\nu_0} \exp \frac{KV}{k_B T} \quad (2.1)$$

with K the anisotropy constant, V the volume of the nanoparticle, $k_B T$ the thermal energy and ν_0 the attempt frequency factor of the order of 10^9 s^{-1} .

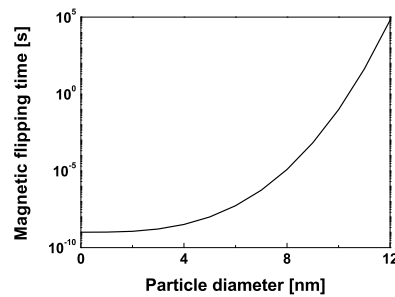


Fig. 2.1: Lifetime of a magnetic state τ_m versus the radius of the single domain nanoparticle with an uniaxial anisotropy constant $K = 1.8 \cdot 10^4 \text{ J/m}^3$.

In case of a high temperature or a small particle size the magnetization is quickly changing between the two metastable states resulting in a time average magnetization of zero. The magnetization of a non-uniform composite material containing these magnetic nanoparticles (like the material the particles are made of) is zero in absence of an external field at any given moment in time because of the random orientation of the nanoparticles inside the composite material. Once an external field is applied to such a composite material, the magnetic moments of

the individual nanoparticles align with the field as individual spins do in paramagnetic materials. Note that due to the random orientation of the nanoparticles, the composite material has in contrast to the individual nanoparticle, no preferential direction in which it is easily magnetized. Since the magnetic moment of a nanoparticle is much larger than that of an individual spin in paramagnetic material, the composite material of nanoparticles is often referred to as super-paramagnetic. Note that the smallest timescale of the experiment determines whether the material shows super-paramagnetic behavior during the experiment.

To calculate the magnetic response of an ensemble of mono-disperse nanoparticles in an external field, we evaluate the energy U of the magnetic moment \vec{m} of a nanoparticle in an external field \vec{B} :

$$U = -\vec{m} \cdot \vec{B} = -mB \cos \theta \quad (2.2)$$

with θ the angle between the magnetic field and the magnetic moment. For perfect alignment ($\theta = 0$) this energy is minimal but due to thermal energy the orientation of the magnetic moment is disturbed. For each domain (i) this can be expressed by a Boltzmann factor P_i :

$$P_i \propto \exp \frac{mB \cos \theta_i}{k_B T} \quad (2.3)$$

Integration over all magnetic moments in the ensemble over all angles θ_i weighted by their Boltzmann factors P_i gives the magnetization M of the ensemble:

$$M = nm \left(\coth(z) - \frac{1}{z} \right) = nmL(z) \quad (2.4)$$

with $z = \frac{mB}{k_B T}$, n the number of magnetic moments in the ensemble and $L(z)$ the Langevin-function^[7] for paramagnetism (Fig. 2.2).

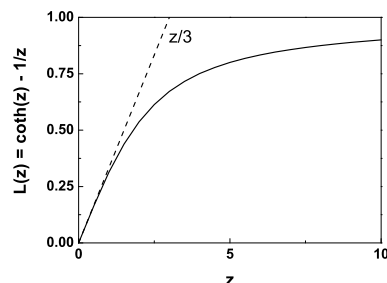


Fig. 2.2: The Langevin curve $L(z)$ as function of the argument z with the approximation $L(z) = z/3$ for small values of z (dashed line).

For small fields and/or high temperatures *i.e.* small values of z , the first order approximation of the Langevin equation is given by $z/3$ and the magnetization is linearly dependent on the applied field *i.e.* with a constant susceptibility (χ) that is defined by $\chi = \frac{M}{H}$.

The particles used in the experiments described in this thesis, are obtained from Dynal and consist of polydispersed iron-oxide nanoparticles inside a polystyrene matrix. The particles are available with various types of active groups or antibodies on the surface and are suspended in a buffer solution.^[8] In the experiments My-One particles with a diameter of $1 \mu\text{m}$, and M-270 and M-280 particles both with a diameter of $2.8 \mu\text{m}$ are used. The My-One and M-280 particles are coated with a protein called streptavidin while the M-270 particles have carboxyl ($-\text{COOH}$) groups on the surface.

In view of the intended application of forces on particles and since the manufacturer does not provide detailed specification of the magnetic properties of the particles, we characterized the particles by measuring the magnetization curve of $50 \mu\text{L}$ of undiluted stock suspension in a vibrating sample magnetometer (VSM 10, by DMS magnetics). The measured magnetic moment is normalized to the number of particles in the sample as given by the manufacturer (Fig. 2.3).

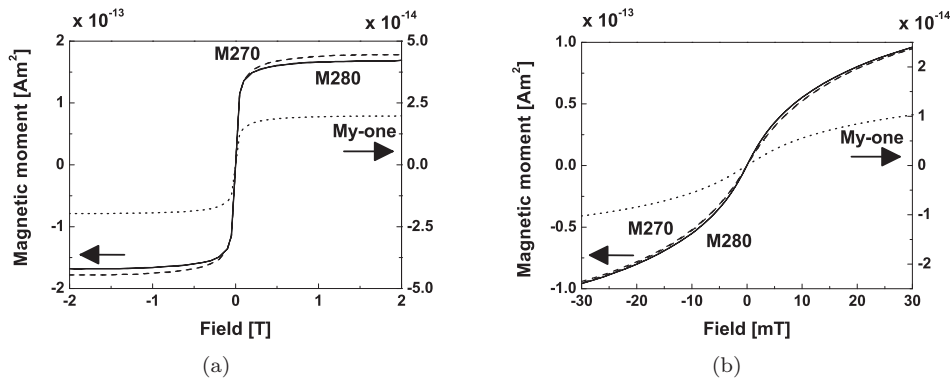


Fig. 2.3: (a) The magnetic moment per particle of Dynal M-280, M-270 and My-One particles for fields up to 2 T. The magnetic moments of the M-270 and M-280 particles are comparable, and about 8.5 times the magnetic moment of the My-One particles. Note the different scales on the axes. (b) Magnetic moments for low fields (up to 30 mT) showing no hysteresis.

The measured magnetization curves show a Langevin-like behavior but can not be fitted with a single curve as given by equation 2.4 because the nanoparticles in the particles are not monodisperse. If we calculate the ratio between the magnetic moments of the $1 \mu\text{m}$ and $2.8 \mu\text{m}$ particles, we find an 8.5 times increase in magnetic moment independent of the applied field. Under the assumption that the same composite material is used for all particles, the magnetic content of a

particle scales with its volume and we would expect an increase of a factor of 22. The iron content of the 1 μm and 2.8 μm Dynal particles has been determined by Fonnum *et al.*^[2] using inductively coupled plasma atomic emission spectrometry (ICP-AES). They report a higher iron concentration for the My-One particles compared to the M-280 particles (255 mg/g versus 118 mg/g) which results in an increased density for the My-One particles (1700 kg/m³ versus 1400 kg/m³). Taking these numbers into account, the 2.8 μm particles contain 8.3 times more iron with respect to the 1 μm particles which is consistent with the results found from our VSM measurements.

2.3 Forces on molecules and small bodies in aqueous solution

When molecules or small bodies like micro/nano-meter sized particles are suspended in an aqueous solution, they are subject to forces of various nature. These forces can be divided in two categories: specific forces and non-specific forces. The specific forces can be seen as a unique combination of non-specific forces between two macromolecules that fit together in a 3D space to form a strong non-covalent bond.^[9] The antigen-antibody bond is an example of such a very specific bond from a combination of 3D structured molecules and non-specific molecular interactions. Table 2.1 lists the major non-specific physical forces as summarized in the work of Leckband and Israelachvili titled *Intermolecular forces in biology*.^[9]

The DLVO theory named after the groups of Derjaguin & Landau (1941) and of Verwey & Overbeek (1949) accounts for the van der Waals and electrostatic double layer interactions between surfaces in aqueous solutions using the mean field approximation. In addition to the van der Waals and electrostatic interaction, the classic DLVO theory has been extended with forces arising from *e.g.* acidbase, steric, and hydrodynamic interactions in the extended DLVO theory (XDLVO).^[10]

The experimental results on non-specific binding of particle to a glass substrate as presented in this thesis (chapter 4 and 6) are interpreted using the classic DLVO theory. Therefore in this chapter, we restrict ourselves to explaining the van der Waals and electrostatic interaction.

The van der Waals force arises from fluctuations in the electric dipole moments of the material. In more detail, the van der Waals interaction can be separated into three different interactions: Keesom interaction which describes the interaction between two polar molecules that tend to align in the energetically most favorable position, Debye interaction which describes the interaction when a polar molecule polarizes a non-polar molecule and finally London dispersion which describes the increase in correlation of the charge distributions when two molecules approach each other. In the mean field approximation of the interaction between mesoscopic bodies, the Hamaker constants of the materials are the key parameters.

Table 2.1: *Non-specific physical interactions and their characteristics.*^[9]

Interaction	Characteristics
van der Waals	Existing between all bodies, usually attractive but occasionally repulsive.
Electrostatic	Existing between charged bodies, attractive or repulsive depending on charge.
Steric	Short-range quantum-mechanical repulsive force that defines the geometry and shape of a molecule.
Thermal fluctuation	Temperature dependent force associated with the local concentration and configurational entropy of atoms or molecular groups, usually repulsive.
Hydrogen bonding	Special electrostatic binding between positively charged hydrogen atoms bound to electronegative atoms, attractive and directional.
Hydrophobic	Attractive interaction in water between inert, non-polar molecules or surfaces.

Hamaker constants are positive and describe the interaction of two identical bodies in vacuum. The combined Hamaker constant for the interaction of two different bodies through a medium can be calculated from the individual Hamaker constants. For the system of the bodies 1 and 2 separated with a medium m , each having their own Hamaker constant of respectively A_{11} , A_{22} and A_{mm} the combined Hamaker constant A_{1m2} is given by:^[11,12]

$$A_{1m2} = c \left(\sqrt{A_{11}} - \sqrt{A_{mm}} \right) \left(\sqrt{A_{22}} - \sqrt{A_{mm}} \right) \quad (2.5)$$

the correction factor c accounts for the dielectric constant of the medium. For vacuum this constant is equal to one whereas for water it is experimentally determined to be 1.6.^[13] Note that the exact value of this correction factor does not influence the conclusions drawn from the qualitative interpretations of the results as presented in this thesis.

Depending on the individual constants, the combined Hamaker constant can be either positive or negative. Table 2.2 lists typical Hamaker constants of several materials.

Table 2.2: Typical Hamaker constants in vacuum.^[13–15]

material	Hamaker constant $A/10^{-20}$ [J]
water	4
glass	7
polystyrene	8
proteins	2.5

For magnetic particles in the vicinity of a surface, the van der Waals interaction can be approximated by that of a sphere with a radius r close to a flat surface, at a distance D . The van der Waals energy becomes:

$$E_{vdw}(D) = -A_{1m2} \frac{r}{6D} \quad (2.6)$$

with $r \gg D$ and A_{1m2} the combined Hamaker constant.

In addition to the van der Waals force, the electrostatic force is a long-range force that almost always exists between two molecules or surfaces in aqueous solutions. The interaction between particles and a surface can again be approximated by a sphere with a radius r close to a flat surface at a distance D . The electrostatic energy becomes:

$$E_e = rZe^{-\kappa D} \quad (2.7)$$

with D the separation distance, Z the interaction constant and κ the reciprocal Debye length. The interaction constant is given by:

$$Z = 64\pi \left(\frac{k_B T}{e} \right)^2 \epsilon_0 \epsilon_r \tanh \left(\frac{ze\psi_{sphere}}{4k_B T} \right) \tanh \left(\frac{ze\psi_{wall}}{4k_B T} \right) \quad (2.8)$$

with ψ_{sphere} and ψ_{wall} the surface potential of both the sphere and the wall. The reciprocal Debye length is given by:

$$\kappa = \sqrt{\frac{2N_A e^2 I_c}{\epsilon_0 \epsilon_r k_B T}} \quad (2.9)$$

with N_A Avogadro's constant, e the elementary charge, ϵ_0 the permittivity of free space, ϵ_r the dielectric constant of the fluid, k_B Boltzmann's constant, T the temperature and I_c the ionic strength:

$$I_c = \frac{1}{2} \sum_i c_i z_i^2 \quad (2.10)$$

with c_i the molar concentration of ion i with a charge number z_i .

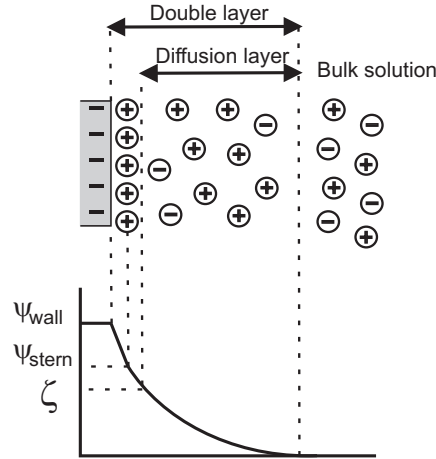


Fig. 2.4: A solid that is brought into contact with a liquid can acquire a surface charge which results in a surface potential ψ_{wall} . In the Stern layer the potential decreases linearly and the Stern potential ψ_{stern} is defined as the potential in the center of the layer. Outside the Stern layer a diffusion layer is formed in which an excess of counter-ions shield the surface potential until the electric potential is equal to zero. The combination of the Stern layer and the diffusion layer is called the electric double layer and the zeta-potential is defined as the potential at the transition between the immobile Stern layer and the mobile diffusion layer.

In spite of their different meaning, commonly the zeta-potential ζ is used as a measure for the surface potential since the zeta-potential is easily measured experimentally (Fig. 2.4).^[9, 12] When a solid is brought into contact with a liquid, it can acquire a surface charge which results in a surface potential ψ_{wall} . Counter-ions from the fluid are then attracted to the wall and form an immobile layer called Stern layer. In this layer of typically a few Ångström, the potential decreases linear and the Stern potential ψ_{stern} is defined as the potential in the center of the Stern layer. Outside the Stern layer a diffusion layer is formed in which an excess of counter-ions shield the surface potential until the electric potential is equal to zero. The combination of the Stern layer and the diffusion layer is called the electric double layer and the zeta-potential is defined as the potential at the transition between the immobile Stern layer and the mobile diffusion layer. Note that the zeta-potential is therefore directly dependent on the ionic strength of the fluid.

As an illustrative example, the van der Waals and electrostatic energy are calculated (Fig. 2.5) as function of the distance between a perfect sphere with a diameter of $2.8 \mu\text{m}$ that is protein coated and a flat glass surface using typical values for the parameters as listed in (Tab. 2.3).

Parameter	Value
ζ -glass	-30 mV
ζ -sphere	-15 mV
R	1.4 μm
ϵ_r	80
z	1
I_c	1 mM and 10 mM
A_{1m2}	$-0.45 \cdot 10^{-20}$ J

Table 2.3: Parameters and their values as used in the calculation of the van der Waals and Electrostatic energy.

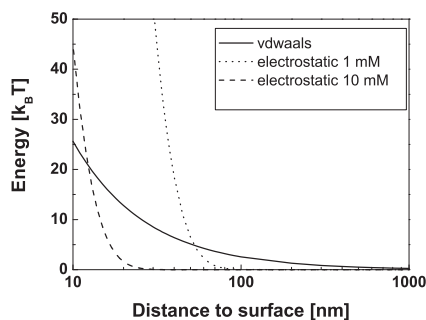


Fig. 2.5: The van der Waals and Electrostatic energy of a 2.8 μm sphere above a glass substrate versus the distance to the surface.

Due to the equal sign of the surface charges, the electrostatic force between the sphere and the surface is repulsive. For increasing ionic strength this force becomes more shielded due to the formation of the double layer causing a shift of the curve. The van der Waals energy is not directly dependent on the ionic strength, yet the Hamaker constants are reported slightly lower in fluids with a high ionic strength.^[9] In this particular example, the van der Waals force is repulsive since the combined Hamaker constant (A_{1m2}) for the protein-water-glass system, as calculated from the typical values given in table 2.2, is negative. Note that the theory as described above is only valid for a perfect sphere in the vicinity of a perfectly flat surface. In the experimental case, the surfaces of the two bodies are likely to have some surface irregularities and these become increasingly important with decreasing distance between the bodies.^[16, 17] The particles used in the experiments described in this thesis have a surface roughness of the order of 100 nm (chapter 4). Furthermore when the surfaces are functionalized with biological molecules, these molecules can rearrange themselves depending on *e.g.* their size or stiffness which gives the surfaces some flexible "fluffy" layer. The way these processes perturb the ideal situation is difficult to model theoretically or to express in terms of a simple force-law.

2.4 Kinetics of biological bonds

Since the use of particles in immunoassays involves the binding and unbinding of antibody-antigen pairs, the most important aspect of antibody-antigen inter-

actions will be summarized here. The binding/unbinding reactions of biological systems such as antibody-antigen couples can simplistically be described by the reaction between two components that form a complex in a dynamic equilibrium as given by the Law of Mass Action:^[1, 18, 19]



with $[A]$ and $[B]$ the concentrations of the individual component and $[AB]$ the concentration of the formed complex. The rate at which the complex is formed is characterized by the association rate constant k_a where the dissociation rate constant k_d characterizes the dissociation of the complex into the free antigen and antibody.

The ratio of the bound and unbound component after reaching equilibrium is known as the equilibrium constant K_{eq} or affinity constant and is equal to:

$$K_{eq} = \frac{[AB]}{[A][B]} = \frac{k_a}{k_d} \quad (2.12)$$

For an antigen-antibody bond, the differences in k_a between different antigen-antibody pairs are rather limited and usually of the order of $1 \cdot 10^7 \text{ M}^{-1}\text{s}^{-1}$ whereas k_d varies widely between $1 \cdot 10^{-4} \text{ s}^{-1}$ and $1 \cdot 10^4 \text{ s}^{-1}$ for antigen-antibody pairs with various affinities.^[19]

Before binding between the two macromolecules can occur, they have to align in 3D space such that the binding sites of both molecules come into contact. This alignment over a short length scale is driven by Brownian rotation and translation of the molecules. As a result, the association rate displays relatively restricted variations between different but similar sized antigen-antibody pairs. The variation in affinity between different antigen-antibody pairs is therefore mainly due to variations in dissociation rate constant. A broad range of techniques exists to measure association and dissociation rate constants and by that characterize the binding in biological systems.^[1]

A single molecular bond can be seen as being in a confined state in an energy landscape with an energy minimum (Fig. 2.6). Escape from this confined state happens along a preferential path called the reaction coordinate. Note that this is not related to a one dimensional translation along a certain axis but it represents a pathway in 3D space.

The dissociation rate constant for such an escape process is given by:^[20]

$$k_d = \nu \exp \frac{-E_b}{k_B T} \quad (2.13)$$

with E_b the activation energy corresponding to the height of the energy barrier and ν is an attempt frequency factor in which all dynamics of the molecules are captured. In liquids this frequency is of the order of magnitude of 10^{10} s^{-1} .^[20]

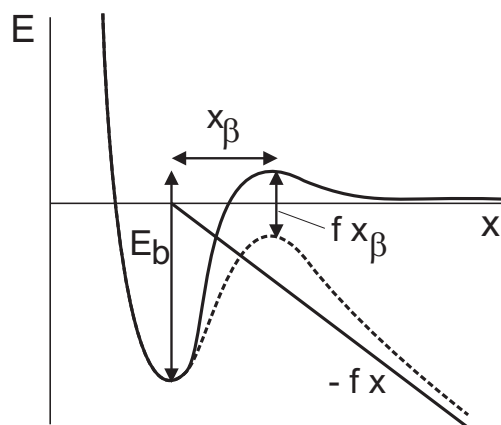


Fig. 2.6: Energy landscape of a bond with a single barrier versus the reaction coordinate (x). If a force (f) is applied the energy landscape gets tilted and the barrier is lowered by an energy equal to $-fx_\beta$.^[20]

One way of measuring the dissociation rate constant is by applying an external force to the biological bond by using magnetic tweezers. Once a force (f) is applied to the biological bond, the energy landscape is tilted and the barrier is lowered by an energy equal to the $-fx_\beta$. The dissociation rate constant becomes now dependent on the force and is given by:

$$k_d(f) = \nu \exp \frac{-(E_b + fx_\beta)}{k_B T} = k_d(0) \exp \frac{fx_\beta}{k_B T} \quad (2.14)$$

with $k_d(0)$ the dissociation rate constant at zero force.

When the molecules are separated from each other after the bond breaks, no rebinding is possible and the effective association rate constant becomes zero. The number of molecules bound to the surface is then given by the following differential equation:

$$\frac{dN(t)}{dt} = -k_d(f)N(t) \quad (2.15)$$

with $k_d(f)$ the force dependent dissociation rate constant. If the force is time-independent, the number of bound molecules in time is given by:

$$N(t) = N(0) \exp(-k_d(f)t) \quad (2.16)$$

So by measuring the amount of bound molecules in time at a given force, the dissociation rate constant at zero force can be calculated. This implies that magnetic particles that have been used as labels in an immunoassay may in principle be used as magnetic tweezers to probe the affinity of a biological bond.

The question arises whether bond breaking by twisting (chapter 1) can be achieved and how this can be described. For rotational excitation of a molecular bond an analogue description can be given as presented here for the force induced dissociation. In such a description, the reaction coordinate then represents the angle over which the system is twisted. However, a detailed knowledge of the potential energy landscape of the bond upon twisting is required. The most elementary angle-dependent potential energy is found for bond twisting in organic molecules, where the potential is periodically with respect to the rotation angle *i.e.* over 360 degrees of rotation. For more complex structures such as proteins, this angle-dependent energy landscape is more complex and not likely to be periodic, especially when the molecules are elastically and/or plastically deformed for large twisting angles. In this thesis only small torques are applied and no rotation induced bond-breaking is observed. Consequently, the unknown angular-dependent potential is approximated by a harmonic potential through the application of Hook's law for rotation.

References

- [1] D. Wild. *The Immunoassay Handbook*. Elsevier, 3 edition, 2005.
- [2] G. Fønnum, C. Johansson, A. Molteberg, S. Mørup, and E. Aksnes. Characterisation of Dynabeads by magnetization measurements and Mössbauer spectroscopy. *Journal of Magnetism and Magnetic Materials*, 293:41–47, 2005.
- [3] R.C. O'Handley. *Modern Magnetic Materials: Principles and Applications*. Wiley-Interscience, 1999.
- [4] R.F. Butler and S.K. Banerjee. Theoretical single-domain grain size range in magnetite and titanomagnetite. *Journal of Geophysical Research*, 80(29):4049–4058, 1975.
- [5] B.M. Moskowitz. Hitchhiker's guide to magnetism. *Consulted 2009*: <http://www.irm.umn.edu/hg2m/hg2m.pdf>.
- [6] G. Bertotti. *Hysteresis in Magnetism: for Physicists, Materials Scientists, and Engineers*. Academic Press, 1998.
- [7] W.T. Coffey, Y.P. Kalmykov, and J.T. Waldron. *The Langevin Equation with Applications in Physics, Chemistry and Electrical Engineering*, volume 10 of *Series in Contemporary Chemical Physics*. World Scientific Publishing Co Pte Ltd, 1997.
- [8] Dynal-Biotech. *Dynabeads Streptavidin Products and Applications*, 2003.
- [9] D. Leckband and J. Israelachvili. Intermolecular forces in biology. *Quarterly Reviews of Biophysics*, 34(2), 2001.

-
- [10] E.M.V. Hoek and G.K. Agarwal. Extended DLVO interactions between spherical particles and rough surfaces. *Journal of Colloid and Interface Science*, 298:50–58, 2006.
- [11] T.F. Tadros. *Colloid Stability: The Role of Surface Forces*. Wiley, 2006.
- [12] D. Grasso, K. Subramaniam, M. Butkus, K. Strevett, and J. Bergendahl. A review of non-DLVO interactions in environmental colloidal systems. *Reviews in Environmental Science and Biotechnology*, 1(1):17–38, 2002.
- [13] J. Visser. On Hamaker constants: a comparison between Hamaker constants and Lifshitz-Van der Waals constants. *Advances in colloid and interface science*, 3(4):331–363, 1972.
- [14] M. Lund and B. Jönsson. A mesoscopic model for protein-protein interactions in solution. *Biophysical Journal*, 85(5):2940–2947, 2003.
- [15] *Consulted 2009: http://web2.clarkson.edu/projects/crcd/me437/downloads/5_vanderWaals.pdf*.
- [16] L. Suresh and J.Y. Walz. Effect of surface roughness on the interaction energy between a colloidal sphere and a flat plate. *Journal of Colloid and Interface Science*, 183:199–213, 1996.
- [17] L. Suresh and J.Y. Walz. Direct measurement of the effect of surface roughness on the colloidal forces between a particle and flat plate. *Journal of Colloid and Interface Science*, 196:177–190, 1997.
- [18] H. Shang and G.U. Lee. Magnetic Tweezers Measurement of the Bond Lifetime-Force Behavior of the IgG-Protein A Specific Molecular Interaction. *Journal of the American Chemical Society*, 129(20):6640–6646, 2007.
- [19] P. Bongrand. Ligand receptor interactions. *Reports on Progress in Physics*, 62:921–968, 1999.
- [20] E. Evans. Probing the relation between force-lifetime and chemistry in single molecular bonds. *Annual Review of Biophysics and Biomolecular Structure*, 30:105–128, 2001.

Chapter 3

On-chip detection of magnetic particles

In this chapter we demonstrate the real-time on-chip detection and manipulation of single 1 μm and 2.8 μm super-paramagnetic particles in solution, with the aim to investigate the feasibility of a biosensor that can give information on biological function. The chip-based sensor contains micro fabricated current wires and giant magneto resistance (GMR) sensors. The current wires serve to apply force on the particles as well as to magnetize the particles for on-chip detection. The particle is pulled back and forth over the GMR sensor by alternately applying a current to one of the two wires flanking the sensor. By simultaneously measuring the sensor signal and the position of the particle, the sensitivity profile of the sensor was reconstructed. A single-dipole model reproduces the measured sensitivity curve for a 1 μm particle. For a 2.8 μm particle, the model shows deviations which we attribute to the fact that the particle size becomes comparable to the width of the GMR sensor. A linear relationship between the number of particles and the sensor signal is found in the range between 1 and 9 particles. The real-time detection and manipulation of individual particles opens the possibility to perform on-chip high-parallel assays with single-particle resolution.

A condensed version of this chapter has been published as: X.J.A. Janssen, L.J. van IJzendoorn and M.W.J. Prins *On-chip manipulation and detection of magnetic particles for functional biosensors* Biosensors and Bioelectronics **23**, 833–838 (2008)

3.1 Introduction

In chapter 1, two different ways of magnetic actuation were suggested, *i.e.* pulling and rotation. In this chapter we study the possibility of on-chip pulling on and detection of magnetic labels. The work of Panhorst *et al.*^[1] shows that two on-chip current wires allow sensitive bondforce measurements on ligand-receptor pairs using super-paramagnetic particles. In these measurement, a current through one of the wires induces a magnetic field which magnetizes the particles and pulls them towards the wire due to the gradient in the magnetic field. The streptavidin coated particles bind to the biontynylated surface by forming a streptavidin-biotin bond. After a given incubation time, the current through the first wire is switched off and the current through the adjacent wire is slowly increased. At low currents, all the unbound particles move from the first to the second wire. At a specific higher current, the particles that were specifically bound on top of the first wire are ripped of the surface. The movement of the particles and by that the bond breaking events are monitored by video-microscopy. Here we investigate the feasibility of this measurement technique in a miniaturized point-of-care sensor with particle detection inside the sensor cartridge itself.

The Philips GMR biosensor^[2-5] is designed for measuring concentrations of biological agents in fluids using super-paramagnetic particles as a label. The detection platform consists of a printed circuit board with readout electronics and a disposable cartridge that contains the actual sensor. The sensor cartridge^[6,7] consists of a molded interconnection device (MID) that connects the chip to a flex foil cable (Fig. 3.1a). The chip contains four individual sensors so in principle the concentration of four different agents can be detected simultaneously (Fig. 3.1b). Each sensor consists of a magnetic field sensor (based on the Giant Magneto Resistance effect), flanked by two current wires (Fig 3.1c).

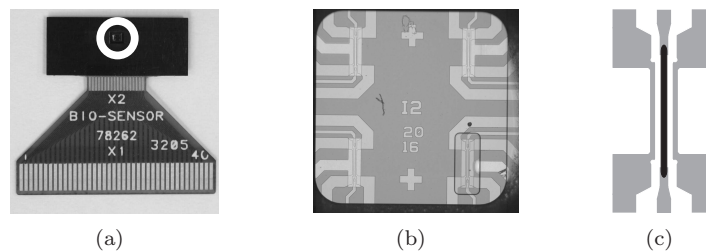


Fig. 3.1: (a) The Philips GMR biosensor cartridge consists of a molded interconnection device (black) which connects the chip (indicated by white circle) with the flex foil cable. (b) The chip is $1\text{ mm} \times 1\text{ mm}$ and contains four sensors. The sensor in the lower right corner is covered with a layer of SU8 to prevent particles from reaching the surface of the chip to use this sensor as an internal reference. (c) Each sensor consists of a magnetic field sensor (black) flanked by two current wires (gray).

The sensor and wires are covered with a layer of silicon nitride ($0.5 \mu\text{m}$) and a 80 nm thick gold layer (Fig. 3.2). The silicon nitride insulates the wires from the fluid while the gold provides a surface for biochemical functionalization. In absence of an applied magnetic field, the super-paramagnetic particles do not have a magnetic moment. Once a field is applied by the wire, the particle becomes magnetized. The vertical component of the magnetic field generated by the wire is not detected since the GMR sensor is most sensitive for the in-plane component of the magnetic field perpendicular to the long axis of the sensor.^[8] The horizontal component of the dipole-field of the particle does change the resistance of the GMR sensor:

$$R_{GMR}(H_p) = R_0 + cH_p \quad (3.1)$$

with R_0 the resistance without field, c a constant depending on *e.g.* the sensitivity and geometry of the sensor and H_p the horizontal component of the dipole-field of the particle. Note that the changes in resistance are small (a few percent) compared to R_0 .

Once the particles are bound to the surface of the sensor in a biological assay as explained in chapter 1, the change in resistance is a measure for the amount of particles present and by that a measure for the concentration of the biological agent.

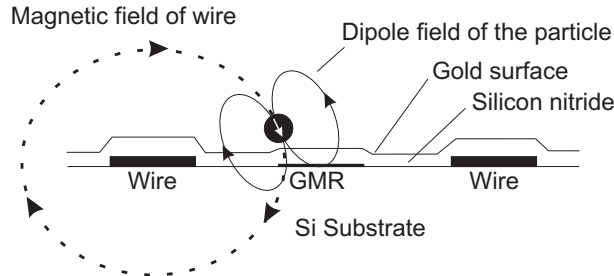


Fig. 3.2: Cross-section of the sensor: The current wire ($3 \mu\text{m} \times 100 \mu\text{m} \times 0.35 \mu\text{m}$) produces a magnetic field that induces a dipole moment in the super-paramagnetic particle. The GMR sensor ($3 \mu\text{m} \times 100 \mu\text{m} \times 0.04 \mu\text{m}$) is most sensitive for in-plane magnetic fields. Therefore the presence of the particle is detected by the horizontal component of the stray field while the magnetic field of the wire is hardly detected since it has essentially an out of plane component at the position of the sensor.

In this chapter we study the capability of the Philips biosensor platform to detect a single magnetic particle. First the details of the readout electronics are explained followed by an analytical calculation and finite element (Comsol Multiphysics) simulation of the sensor signal. A brief discussion of the experimental setup is followed by the results and discussion on the detection of single $1 \mu\text{m}$ and $2.8 \mu\text{m}$ Dynal particles.

3.2 Magnetic biosensor

3.2.1 Sensor and readout electronics

The purpose of the readout electronics is to convert the change in resistance of the GMR sensor into a measurable signal.^[3] The change in resistance can be measured by incorporating the resistor in the feedback loop of an inverting amplifier (Fig. 3.3).

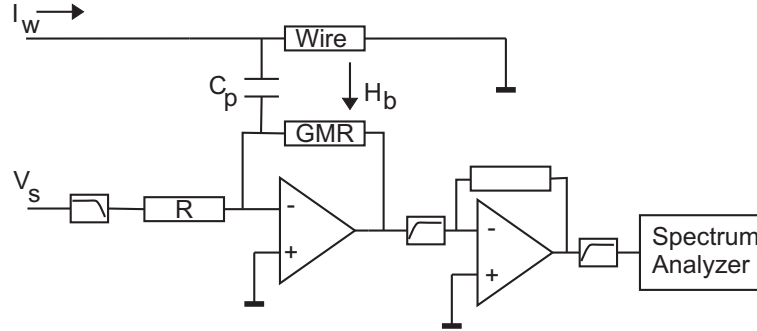


Fig. 3.3: Schematic representation of the sensor readout circuit. The current through the wire (I_w) creates a magnetic field around the wire. The changes in the magnetic field (H_p) due to the presence of the particles induces changes in the resistance of the GMR sensor. The changes in resistance are converted to changes in voltage by the first inverting amplifier. This signal is then amplified by a second inverting amplifier and analyzed by a spectrum analyzer. The purpose of the low and two high-pass filters is explained in the text.

The output voltage of the first amplifier then depends on the input voltage (V_s), the input resistance (R) and the field dependent resistance of the GMR-strip ($R_{GMR}(H_p)$):

$$V_{out} = -V_s \frac{R_{GMR}(H_p)}{R} \quad (3.2)$$

Finally the output of the first amplifier is amplified by the second amplifier. In principle this circuit can operate with a DC current through the wire and a DC sensor voltage. To overcome 1/f noise, an AC current is applied to the wire: $I_w(t) = \hat{I}_w \cos(\omega_1 t)$ instead of a DC current. This modulation allows lock-in detection with the spectrum analyzer (Fig. 3.3). The drawback of using a AC current through the wire is capacitive crosstalk (C_p) between the wires and the sensor *i.e.* the wires are isolated from but in close proximity of the sensor which can be seen as a parasitic capacitor. The crosstalk increases with increasing frequency because the impedance of this capacitor: $Z = \frac{1}{\omega C}$ decreases with increasing frequency. The crosstalk component is depicted in the power spectrum in figure 3.4 by the dotted

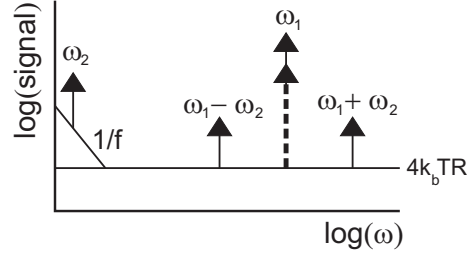


Fig. 3.4: Schematic representation of the power spectrum as measured with the spectrum analyzer. The spectrum shows the thermal noise ($4k_bTR$) which is independent of the frequency and scales with the temperature (T) and the resistance (R). The effect of $1/f$ noise is reduced by measuring at high frequencies (ω_1). The presence of the other frequency components is explained in the text

arrow. Note that this component is present in the spectrum even without the presence of particles.

Because the magnetic field of the wire is modulated, also the stray field of the particle: $H_p(t) = \hat{H}_p \cos(\omega_1 t)$ is modulated and by that the resistance of the GMR sensor: $R_{GMR}(t) = R_0 + c\hat{H}_p \cos(\omega_1 t)$. The contribution of the particles to the signal (small arrow on top of the dotted arrow in Fig. 3.4) is small (few percent) compared to the cross talk. Variations in cross talk (due to variations in the parasitic capacitance by e.g. changes in temperature, ionic strength of the fluid) make it difficult to separate the signal of the particles from the cross talk.

The signal of the GMR is therefore modulated by applying an AC sensor voltage: $V_s(t) = \hat{V}_s \cos(\omega_2 t)$ with $\omega_2 \ll \omega_1$. The output voltage of the circuit is now the product of the two AC signals:

$$V_{out} = -\hat{V}_s \cos(\omega_2 t) \frac{R_0 + c\hat{H}_p \cos(\omega_1 t)}{R} \quad (3.3)$$

$$= \frac{-\hat{V}_s}{R} \left(R_0 \cos(\omega_2 t) + c\hat{H}_p \cos(\omega_1 t) \cos(\omega_2 t) \right) \quad (3.4)$$

The product of the two sinusoidal signals can be rewritten:

$$\cos(\omega_1 t) \cos(\omega_2 t) = \frac{1}{2} (\cos(\omega_1 t - \omega_2 t) + \cos(\omega_1 t + \omega_2 t)) \quad (3.5)$$

The modulation of the sensor voltage creates two sidebands ($\omega_1 - \omega_2$ and $\omega_1 + \omega_2$) and a low frequency component (ω_2) in the spectrum (Fig. 3.4). The cross talk signal is not modulated with frequency ω_2 because it does not arise from changes in the resistance of the GMR sensor. The sidebands now contain the signal due to the presence of the particles. Note that the signal at ω_1 only contains the cross talk since the contribution of the particles vanishes due to the modulation of the sensor voltage.

Apart from the basic components for the detection and amplification, the readout electronics also contains some filters (Fig. 3.3). The sensor voltage is filtered with a low-pass filter to prevent high frequency noise entering the readout electronics. The high-pass filter (cutoff ≈ 60 kHz) at the output of the first amplifier removes the low frequency component (ω_2) of the sensor voltage to avoid clipping of the second amplifier. The second high-pass filter (cutoff ≈ 200 kHz) finally filters the signal before it is sent to the spectrum analyzer.

3.2.2 Sensor response

The change in sensor signal (Δu_{sensor}) can be calculated by integration of the horizontal component of the stray field of the particle over the sensor strip:^[9]

$$\Delta u_{sensor} = \frac{SRI}{wL} \int dx' dy' H_{b_x}(x', y') \quad (3.6)$$

with S the sensitivity of the GMR-sensor in $\%/(\text{A/m})$, R the absolute resistance of the GMR, I the GMR sensor current, w the width and L the length of the sensor strip. For the sensors used in this thesis, the product of the sensitivity and the absolute resistance is about $2.7 \cdot 10^{-3} \Omega\text{mA}^{-1}$. The induced magnetization of the particle can be calculated from the magnetic field of the wire. The magnetic field $\mathbf{H}(\mathbf{r})$ at a position \mathbf{r} around a current density $\mathbf{j}(\mathbf{r})$ is given by integrating the Biot-Savart law:

$$\mathbf{H}(\mathbf{r}) = \int d^3r' \frac{\mathbf{j}(\mathbf{r}') \times (\mathbf{r} - \mathbf{r}')}{4\pi|\mathbf{r} - \mathbf{r}'|^3} \quad (3.7)$$

For a current density j_y running through a infinitely long wire (orientated parallel to the y -axis) with a rectangular shaped cross-section (Fig. 3.5) with the lower left corner (x_1, z_1) and the upper right corner (x_2, z_2) , the x -component of the magnetic field at the origin $(0,0)$ is given by:

$$\frac{2\pi}{j_y} H_x(0,0) = - \left[\left[z \arctan \frac{x}{z} + \frac{x}{2} \ln(x^2 + z^2) \right]_{x_1}^{x_2} \right]_{z_1}^{z_2} \quad (3.8)$$

Linear coordinate transformation $x_1 \rightarrow x_1 - x$, $x_2 \rightarrow x_2 - x$, $z_1 \rightarrow z_1 - z$ and $z_2 \rightarrow z_2 - z$ gives the horizontal magnetic field component H_x at any position (x,z) . Rotation of the coordinate system gives the vertical field component H_z .

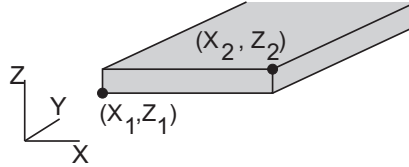


Fig. 3.5: Coordinate system used in the calculation of the magnetic field around a rectangular shaped infinitely long wire.

When the super-paramagnetic particle is approximated by a homogenously magnetized sphere, the magnetization \mathbf{M} is parallel with the external magnetic field \mathbf{H} and for low fields (typically tens of mT) given by:^[10]

$$\mathbf{M} = \chi \mathbf{H} \quad (3.9)$$

with χ the magnetic susceptibility of the particle material including demagnetization effects. For high fields this relation does not hold due to saturation of the magnetic material. The field outside a homogenously magnetized sphere is mathematically equal to that of a magnetic dipole with a dipole moment (\mathbf{m})

$$\mathbf{m} = \mathbf{M}V \quad (3.10)$$

with the magnetization (\mathbf{M}) and the volume of the sphere (V). In coordinate free form the magnetic dipole field is given by

$$\mathbf{H}_{\text{dip}}(\mathbf{r}) = \frac{3(\mathbf{m} \cdot \hat{\mathbf{r}})\hat{\mathbf{r}} - \mathbf{m}}{4\pi r^3} \quad (3.11)$$

with \mathbf{r} the vector from the position of the dipole to the position where the field is calculated, r the absolute value of \mathbf{r} , $\hat{\mathbf{r}}$ the unit vector of \mathbf{r} and \mathbf{m} the magnetic dipole moment.

The combined magnetic field of the current through the wire and the induced dipole field of the particle have been simulated (Comsol Multiphysics) for a particle with a diameter of $3 \mu\text{m}$ (Fig. 3.6). The particle is in contact with the surface of the silicon nitride layer and the horizontal position is varied between the center of the right wire (W2) over the sensor surface towards the center of the left wire (W1). In this simulation only the left wire (W1) is actuated with a current of 100 mA.

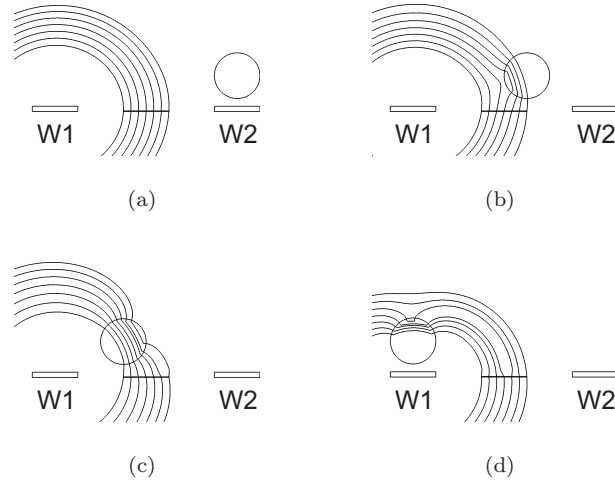


Fig. 3.6: The combined magnetic field of the current through the left wire (W1) and the induced dipole field of a $3\ \mu\text{m}$ particle for various positions of the particle simulated in Comsol Multiphysics. For clarity only some of the field lines through the sensor are plotted. Note that the right wire (W2) does not conduct a current.

With the particle at the center of the right wire (Fig. 3.6a), the magnetization of the particle due to the field of the left wire can be neglected and therefore does not influence the magnetic field at the location of the GMR sensor. It is important to note that in the real sensor, the bottom of the wires and the sensor are aligned in the manufacturing process and the wires are thicker than the GMR sensor ($0.35\ \mu\text{m}$ versus $0.04\ \mu\text{m}$), therefore the magnetic field of the wire is not completely perpendicular to the sensor. The horizontal component (directed away from the wire) gives a small positive sensor signal, even in the absence of a particle as can be seen in figure 3.7 indicated with the letter a. When the particle approaches the sensor, the particle is increasingly magnetized and the net magnetic field is deflected towards the particle. This deflection increases the horizontal component of the field and therefore the sensor signal increases. A maximum is reached when the center of the particle is over the edge of the sensor (Fig. 3.6b). When the particle crosses the center of the sensor, the horizontal field components cancel each other and the signal becomes zero. The signal reaches a minimum at the other edge of the sensor (Fig. 3.6c). Note that the absolute signal at the edge of the sensor closest to the powered current wire, is larger since the particle is more magnetized due to the close proximity of the live current wire. When the distance between the particle and the sensor increases, the signal decreases until the particle reaches the center of the left wire (Fig. 3.6d). The full sensor response is plotted in figure 3.7.

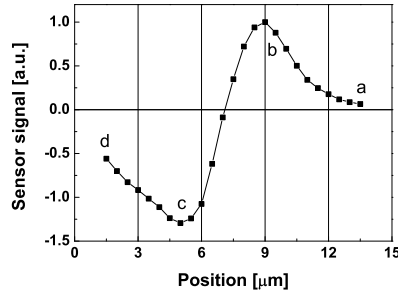


Fig. 3.7: Simulation of the sensor signal for a particle with a diameter of $3 \mu\text{m}$. The sensor signal is normalized and the letters (a-d) correspond to the situations in Fig. 3.6a-d. The vertical lines indicate the edges of the wires and GMR sensor.

3.3 Experimental

3.3.1 Setup

During the experiments the sensor is imaged using an optical microscope (Leica DM 6000M) with a long distance (3 mm) water immersion objective (Leica HXC APO L63X0.90 W U-V-I). The microscope is equipped with a camera (Redlake MotionPro HS-3) for high speed recording of the movements of the particles. A $3 \mu\text{L}$ droplet of 1:8000 diluted suspension of $1 \mu\text{m}$ particles (Dynal MyOne) is put on the sensor with a pipet (Transferpette 2-20 μL Brand). After sedimentation of the particles (typically a few minutes), de-ionized water was added to the droplet to make optical contact with the immersion objective. The high dilution ensures that only a small number of particles is present on the surface of the chip (typically 1 particle per $100 \mu\text{m}^2$). Due to this low amount it is possible to study the sensor response for a single particle, the drawback is that no particles might be present near one of the four sensors. Experimentally it is found that it can take up to 30 minutes for Brownian motion to bring a particle in the vicinity of one of the wires. Once a particle is less than $20 \mu\text{m}$ away from the wire, the magnetic force becomes dominant over the Brownian motion and the particle is pulled to the wire.

By alternately switching the current every 10 seconds between the two wires, the particle is pulled back and forth between the wires (Fig. 3.8). The currents through the wire (100 mA_{pp} at 200 kHz) and the sensor (4 mA_{pp} at 1 kHz) are supplied by function generators (Agilent 33250A). The output signal of the readout electronics is analyzed with a spectrum analyzer (Agilent 4395A) at a rate of 100 Hz and the high speed camera is synchronized with the spectrum analyzer. The pictures are saved and during post processing, the positions of the particles are determined and compared with the measured signal of the GMR.

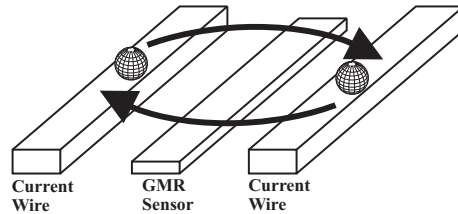


Fig. 3.8: A particle is caught in the potential well of one wire. By alternately switching the current between the wires, the particle crosses the sensor back and forth. The goal is to detect the single particle passing over the GMR sensor.

3.3.2 Image analysis

Particle tracking software is developed in Matlab to automatically determine the position of each particle in each image of the video. The position of the particle(s) in the first image is first determined manually. To reduce the processing time, a region of interest (typically three times the diameter of the particle) is defined around this position. The script then determines the position with an accuracy of 1 pixel (180 nm) by 2D correlation of a template with the region of interest. In each following frame, the region of interest is defined around the position found in the previous frame and the position of the particle is determined again. As a result, the region of interest moves with the position of the particle and the path followed by the particle is determined (Fig. 3.9).

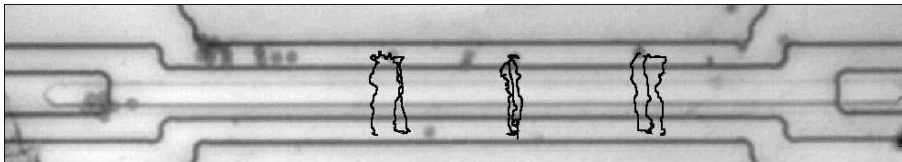


Fig. 3.9: Optical microscopy image of the sensor surface made with a 63 \times water immersion objective. The edges of the current wires are visible as dark horizontal lines (Figure 3.1c shows a schematic representation of the chip for comparison). The gray dots are Dynal My-One particles with a diameter of 1 μm . The black traces show the path of three particles as analyzed by the particle tracking software.

Figure 3.10 shows the position of three particles perpendicular to and parallel with the long axis of the sensor. The particles start at one wire (position ≈ 50) and move toward the second wire (position ≈ 110) with increasing speed once the current is switched to the second wire ($t = 0$ sec). The current is switched every 10 seconds causing the particles to cross back and forth.

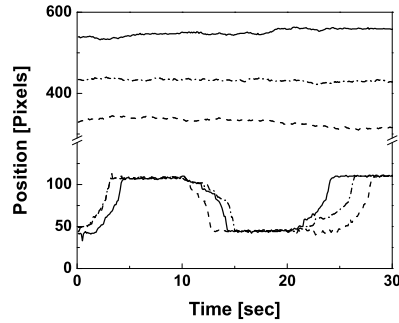


Fig. 3.10: The position of three particles in time (180 nm/pixel). The upper part (above the break) shows the position of the particle parallel with the sensor and the lower part shows the position perpendicular to the sensor.

After switching the current, initially the Brownian motion is dominant over the magnetic force which causes a irregular and non-monotone movement of the particle. The magnetic force increases with decreasing distance to the wire and becomes dominant in the last part of the transition. Once the particle is arrived on the wire that is powered by the current, the motion perpendicular to the wire is confined while the particle is still free to move parallel to the wire.

Obviously, the time to cross to the powered wire as measured from the moment of switching the currents, varies significantly. Variations in crossing time up to 100% are observed between individual particles, but also between different crossings of a single particle (Fig. 3.10). These variations are primarily due to the effect of Brownian motion. Persistent variations in crossing time between particles due to particle-to-particle variations in magnetic content can only be detected after averaging the crossing time of each particle over a large number of crossings.

3.4 Results and discussion

3.4.1 Single particle detection

The sensor signal (Fig. 3.11 bottom panel) is measured simultaneously with the position of the particle perpendicular to the sensor (Fig. 3.11 top panel). The sensor signal results from the superposition of the magnetic field of the particle and that of the wires (section 3.2.2).

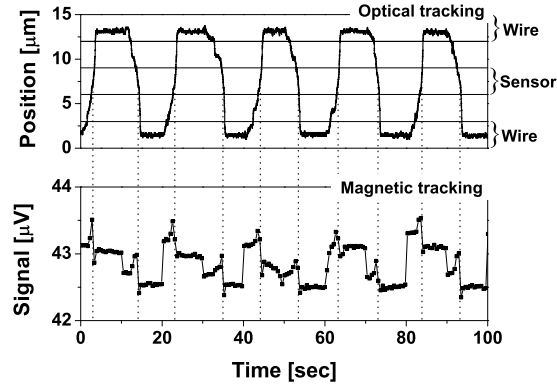


Fig. 3.11: Combined recordings in time of the position (top panel) of the particle perpendicular to the sensor and the sensor signal (bottom panel). Each time the particle crosses the sensor (dotted vertical lines) a sudden rise and decrease in the signal is measured.

The current through the wires is switched by switching the supply voltage from one wire to the other. Therefore small wire-to-wire variations in the resistance (typically 2%) cause variations in the current and by that variations in the magnetic field. This causes the square wave behavior of the sensor signal with a periodicity of 20 seconds. Even if the currents are equal, the square wave is often still slightly visible, because the sensor is not exactly centered between the wires.

During the crossing of the particle, the sensor signal suddenly rises and drops again. These spikes clearly correlate with the moment the particle crosses the sensor strip (dotted vertical lines in Fig. 3.11). The sensitivity profile of the sensor is reconstructed by plotting the sensor signal versus the position of the particle for a Dynal 1 μm My-One and a 2.8 μm M-280 particle (Fig. 3.12).

The upper part (above the break) of the graph shows the sensitivity profile for the particle moving from the right wire towards the left wire (comparable to the simulated particle response in figure 3.6 and 3.7). The lower part of the graph shows the sensitivity profile for the particle moving in the opposite direction. Apart from the offset, the sensitivity profile is equal but mirrored around the center of the GMR sensor. The sensitivity profile measured with the 2.8 μm particle shows the same shape as that of a 1 μm particle. The difference in signal amplitude is caused by the difference in magnetic content. The shape of the sensitivity curves (Fig. 3.12) is qualitatively understood from the model as explained in section 3.2.2 and illustrated in figure 3.7.

Our results show single particle sensitivity for 2.8 μm Dynal M-280 particles as well as for 1 μm Dynal My-One particles that move across the sensor by lo-

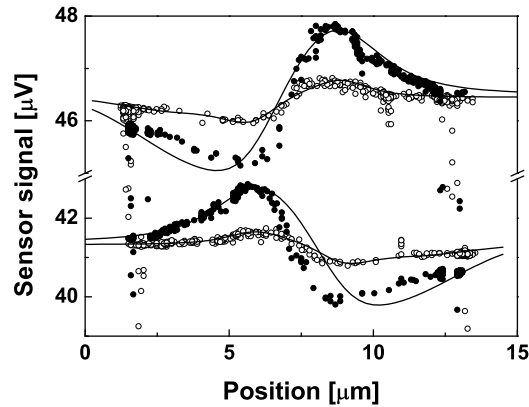


Fig. 3.12: Measured GMR signal versus the position of the particle for a $1 \mu\text{m}$ (\circ) and a $2.8 \mu\text{m}$ particle (\bullet). The lines show the simulated response of the single dipole model. The upper part (above the break) of the graph shows the sensitivity profile for the particle moving from the right wire towards the left wire. The lower part of the graph shows the sensitivity profile for the particle moving in the opposite direction.

cally applied magnetic fields. Single particle detection has been shown for various detector types^[11] *e.g.* microcantilever, Hall and GMR sensors using a stationary $2.8 \mu\text{m}$ Dynal M-280 particle and externally applied magnetic fields. Note that compared to the M-280 particles, the magnetic content of the My-One particles is factor 10 lower showing a lower detection limit of our sensor compared to those described in literature.^[11] Furthermore our approach with the combination of on-chip current wires and a GMR-sensor allows us to detect particles and to exert forces on particles which consequently offers a platform to develop a functional biosensor.

The model based on the dipole moment is plotted (Fig. 3.12) with an offset A to account for the offset due to the field of the wire and prefactor B to account for the amplification in the readout electronics:

$$u_{\text{sensor}} = A + B \int dx' dy' H_{\text{dip}_x}(x', y') \quad (3.12)$$

Compared to the simulated sensitivity curve based on the single dipole, the measured profile for the $2.8 \mu\text{m}$ particle is shifted away from the wire which conducts the current and the deviation increases when the particle approaches the wire. We attribute this deviation to the fact that the size of the particle is comparable to the width of the GMR sensor. Consequently, a part of the particle is considerably

closer to the sensor than the center of the particle is. As a result, the particle is detected further away from the sensor than is expected from the single-dipole model. The deviation from the single-dipole model increases with increasing size of the particle and decreasing distance between the particle and the sensor.

The difference in signal amplitude between the 1 μm and 2.8 μm particles is caused by the difference in magnetic content. We measure an increase in signal amplitude of approximately 6 times for the 2.8 μm particles compared to the 1 μm particles. When the measured profile (Fig. 3.12) is fitted with the single dipole model, we find an increase of the point-dipole strength of a factor 9 for the 2.8 μm particles with respect to the 1 μm particles. This ratio is close to 8.5, as found by the vibrating sample magnetometer (VSM) measurements (chapter 2). Furthermore it is known that the ratio in magnetic content is found to be 8.3 by Fønnum *et al.*^[10] using inductively coupled plasma atomic emission spectrometry (ICP-AES).

The difference between the increase in signal amplitude and the increase in calculated dipole strength (6 times versus 9 times) is understood from the decreasing sensitivity of the sensor with increasing distance to the sensor surface. This decrease in sensitivity is caused by the fact that the particle is less magnetized when it is further away from the wire. Furthermore, the stray field of the particle that is detected by the sensor decreases with increasing distance from the particle. Therefore the material of the particle that is further away from the sensor surface (upper part of the particle) contributes less to the signal than the material close to the sensor. As a result, the sensor signal is not proportional to the size of the particle.

Since the sensitivity profile depends on the height of the particle above the surface of the sensor, the signal does not only decrease in amplitude with increasing distance but the total shape of the profile changes.^[9] In our experiments, the particle is free in solution and consequently the distance between the particle and the sensor surface can not be assumed constant when the particle crosses the sensor. Particles moving parallel to and in close proximity of a wall, experience a force that is directed away from the wall, called hydrodynamic lift-off depending on the *e.g.* speed, density of the fluid and the particle.^[12] Besides by hydrodynamic lift-off, the height of the particle is also influenced by Brownian motion. In addition, when the particle approaches the wire, it is attracted towards the surface due to the gradient in the magnetic field. Due to the interplay of all these effects, the height of the particle is not exactly known in our experiments.

Megens *et al.*^[9] performed measurements showing single particle sensitivity of the GMR sensor by scanning a 2.8 μm particle across the sensor surface using an atomic force microscope (AFM). Sensitivity profiles are measured for various heights of the particle above the sensor surface. When the particle is in contact with the surface, a similar deviation from the single dipole model is observed as we do in our measurements. When the AFM scan is executed with the particle lifted 2 μm above the surface, the deviation of the measurements from the single

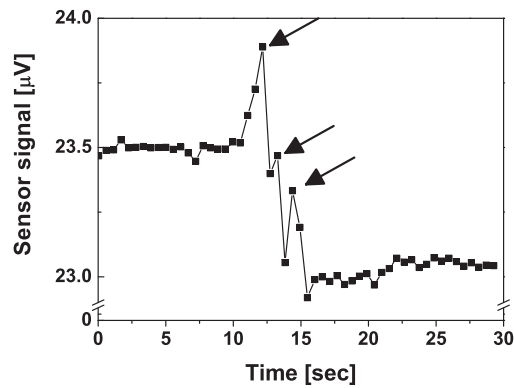
dipole model becomes negligible. This is attributed to the fact that the validity of the single dipole model increases with increasing distance between the sensor surface and the particle. Note that in the experiments of Megens *et al.*^[9] the position of the 2.8 μm particle is actively controlled by the AFM whereas we show single particle sensitivity for 2.8 μm and 1 μm particles that are free in solution, a situation which is closer to the real application in a functional biosensor.

We have shown that the sensor is suited to detect individual particles and a detailed understanding of the sensitivity profile was given. However, the application of the GMR sensor in immunoassays requires the detection of multiple particles. The detection of wire-to-wire transfer is particularly interesting for investigating bond dissociation in a functional biosensor.

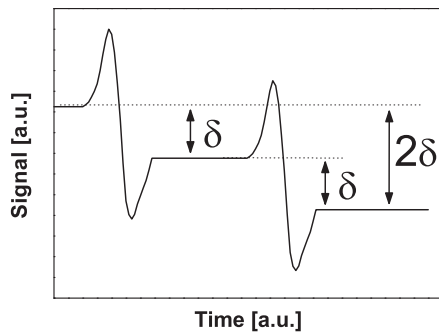
Let us assume the situation in which multiple particles are attracted to one of the two wires by running a current through it. When the particles come in contact with the surface, they bind to the surface due to the formation of a biological bond. Once the current is switched to the other wire, the biological bonds break and the released particles will cross the sensor. If the bonds would break one by one, the particles cross the sensor consecutively and each particle can be detected individually by recording the sensor signal in time and counting the number of spikes. However, in a real experiment it is likely that multiple particles will cross the sensor one by one because the breaking of a bond is a statistical process. Therefore we tested the capability of the sensor to detect multiple particles crossing at the same time.

3.4.2 Detection of multiple particle transfers

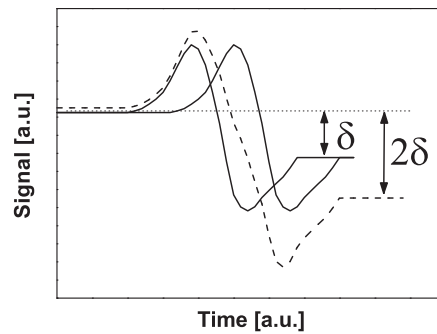
Five particles were caught on one wire and the current was switched. In the recorded sensor signal, three spikes are distinguishable which suggests that only three particles crossed the sensor (Fig. 3.13a). However, video recordings show that all five particles crossed the sensor, so counting the number of spikes underestimates the number of particles that crossed the wire. This underestimation can easily be understood since the sensor output is depending on the net magnetic field that is measured. Figure 3.13b shows a situation in which two particles cross consecutively. Each time a particle has crossed the sensor, a spike is observed and the steady-state signal is decreased by a given amount δ . As a result, the total change (2δ) in the steady state signal is proportional to the number of particles that crossed the sensor. When two particles cross almost at the same time (Fig. 3.13c), the spikes in sensor signal that are related to the crossing of the individual particles are masked. Therefore the number of particles that crossed the sensor can not be determined from the signal recorded during the crossing of the particles. However, the total change in signal (2δ) is still proportional to the number of particles that crossed the sensor. This shift in signal can thus be interpreted as a measure for the number of particles that have crossed the sensor.



(a)



(b)



(c)

Fig. 3.13: (a) Measurement of the sensor signal in time for multiple particles crossing the GMR-sensor. From the three spikes (indicated by arrows) in the sensor signal it might be concluded that three particles crossed the sensor. Actually five particles crossed the sensor almost at the same time and the signal two particles remained undetected. (b) Schematic representation of the sensor signal when two particles cross the sensor consecutively. The sensor signal decreases (δ) each time a particle has crossed the sensor. The total change in signal (2δ) is proportional to the number of particles that have crossed the sensor. (c) Schematic representation of the individual signals of two particles crossing the sensor at almost the same moment in time (full lines) and the combined signal that is measured (dashed line). Note that although the peaks in sensor signal that we related to the crossing of individual particles are masked, the total change in signal is still proportional to the number of particles that crossed the sensor (2δ).

Experiments have been performed to investigate whether the change in steady-state signal can be used as a sensitive measure of the number of particles that have crossed the GMR sensor. The change in signal after crossing the sensor is measured using a procedure as follows:

- I. A particle is caught on the right wire (W2) using a direct current of 20 mA. The sensor output is zero since no AC current runs through either one of the wires.
- II. An alternating current (200 kHz) is applied to the left wire (W1) and the signal due to this wire is measured. Note that although the alternating current is higher (40 mA) than the direct current in right wire, the particle stays on the right wire because of the relative large distance between the particle and the left wire. When the particle is on top of the right wire, its magnetization is constant and therefore does not contribute to the modulation of the resistance of the GMR sensor as explained in section 3.2.1.
- III. The direct current in the right wire is switched off and the particle is attracted by the left wire.
- IV. Once the particle is on the left wire, the direct current is switched on to restore the original configuration. The particle is magnetized by the alternating current and the alternating magnetization of the particle does contribute to the sensor signal.

Figure 3.14a shows the current through wire 1 and 2 (bottom/top) versus time. In the upper graph also the position of the particle with respect to the GMR-sensor is sketched for three key positions in time. Figure 3.14b shows the measured sensor signal for a 1 μm as well as for a 2.8 μm particle. The time intervals numbered in the procedure (I to IV) correspond to those in both graphs (Fig. 3.14a and b).

Although the change in signal (δS) is smaller than the amplitude of the spike, it can still be detected for the 1 μm particles after averaging the signal over several seconds. Increasing the alternating current will increase the change in signal and decrease the averaging time required for single particle sensitivity. In a real application where biological molecules are present, the maximum amplitude of the current through the wire is limited due to heating of the fluid by Joule heating of the wire. Note that in a real application no direct current has to be applied because the particles are biologically bound to the surface of the chip.

We studied the particle response by increasing the number of particles on the sensor one by one up to nine particles (Fig. 3.15a). One particle is caught and the change in signal (δS) is measured as described above. After the first measurement cycle, the AC wire is switched off and the particle is collected on the DC wire. This configuration is maintained until a second particle is attracted by the wire.

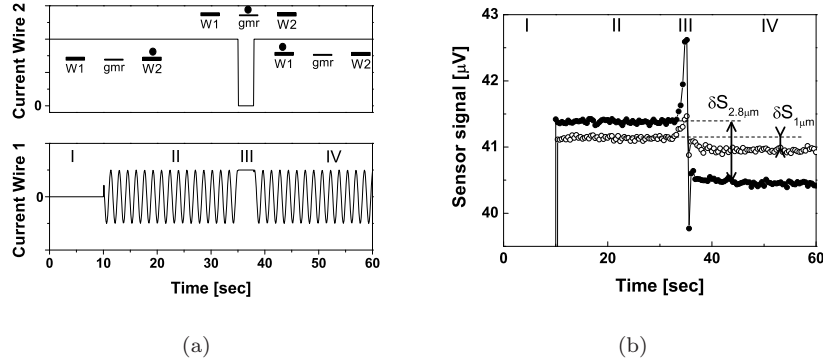
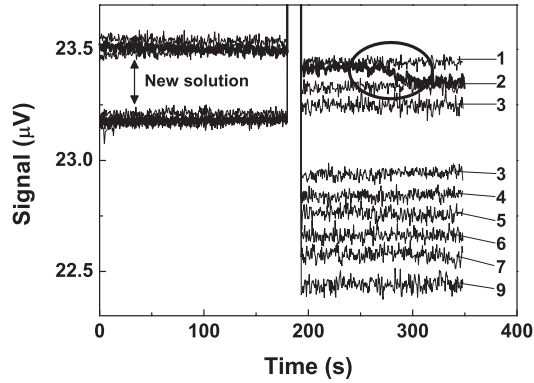


Fig. 3.14: (a) Procedure to measure the change in signal for a single particle crossing the sensor. The graphs show the current through wire 1 and 2 (bottom/top) versus time. Note that the frequency of the alternating current is reduced for clarity. The position of the particle with respect to the GMR-sensor is sketched in the top graph for three key positions in time. The time intervals numbered in the bottom graph (I to IV) correspond to these in figure 3.14b. (b) Measurement of the change in signal for a single $1 \mu\text{m}$ (\circ) and a $2.8 \mu\text{m}$ (\bullet). The decrease in signal δS clearly depends on the size of the particle.

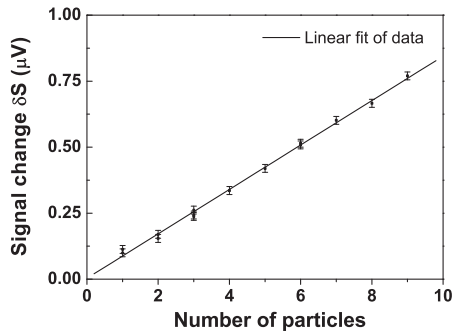
Once the second particle is on the DC wire, the AC wire is switched on and the measurement cycle is repeated.

Figure 3.15a shows the measured signal for different numbers of particles crossing the sensor. Note that during the second measurement on the single particle, a second particle is attracted from the surrounding fluid to the AC wire (Fig. 3.15a circle). The particle approaches the wire from the direction opposite to the position of the GMR. Since the particle does not cross the GMR sensor only a decrease in signal and no spike is observed. After the first measurement on three particles, more fluid is added to increase the number of particles on the sensor surface. The addition of fluid causes a change in the baseline, but the absolute change in signal per particle remains constant.

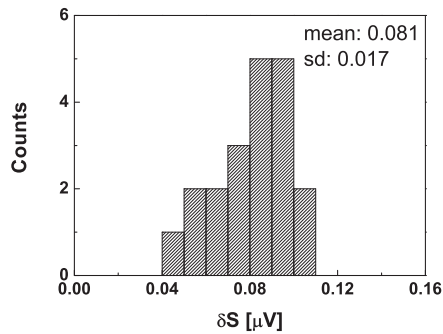
In figure 3.15b the signal change (δS) is plotted versus the number of particles crossing the sensor. The change in signal increases linear with the number of particles on the wire. Experiments of de Boer *et al.*^[3] show a linear response curve for large numbers (50 to 400) of 300 nm particles distributed homogeneously over the surface. Due to the large number of particles, particle-to-particle variations in the magnetic content average out as well as the fact that the sensitivity profile of the sensor is strongly dependent on the position of the particle. We calculated the signal change per $1 \mu\text{m}$ particle to be $0.081 \pm 0.017 \mu\text{V}$ (Fig. 3.15c). The variation in signal change per particle (20%) is larger than standard deviation of the mean signal ($1 \cdot 10^{-4} \mu\text{V}$) and is most probably due to particle-to-particle variations in



(a)



(b)



(c)

Fig. 3.15: (a) The change in signal before and after crossing of $1 \mu m$ particles is measured for 1 up to 9 particles. The change in signal increases with increasing number of particles. The numbers indicate the number of particles present in the experiment. Adding more fluid to increase the number of particles on the chip causes a change in the baseline, but the absolute change in signal per particle remains constant. (b) The change in signal for increasing number of $1 \mu m$ particles. For each measurement, the signal is averaged over 180 sec before and 180 sec after the particles crossed the sensor. (c) Histogram of the signal change shows an average signal change of $0.081 \pm 0.017 \mu V$ per particle.

the magnetic content. The same order of variation is found by Ranzoni *et al.*^[13] by experimentally determining the susceptibility of individual My-One particles. The variations we find for the 1 μm particles are remarkably smaller than the signal variations of 70% observed for 2.8 μm particles by Rife *et al.*^[11]

3.5 Conclusion

We have shown the manipulation and detection of the position of magnetic particles on the surface of a chip with integrated current wires and a sensor based on the giant magnetoresistance (GMR) effect. The magnetic field induced by the current wires magnetizes the super-paramagnetic particles and the stray field of the particles is detected by the GMR sensor. High frequency modulation (200 kHz) of the current through the current wires allows lock-in detection to reduce $1/f$ noise. The current through the GMR sensor is modulated with 1 kHz to distinguish the sensor signal from the capacitive cross-talk in the readout electronics.

Single-particle resolution is proven for 1 μm and 2.8 μm Dynal particles traveling across the sensor surface. The sensitivity profile of the sensor was reconstructed by simultaneous recordings of the position of the particle and the sensor signal. Sensitivity profiles simulated with a single-dipole model resemble the curves measured with 1 μm particles. Experiments with 2.8 μm particles showed deviations with respect to the single-dipole model. These deviations become visible when the size of the particle is comparable (or larger) than the width of the GMR sensor.

A particle-response curve was measured with 1 μm particles, for particle numbers ranging from 1 up to 9. The curve shows a linear relationship between the number of particles and the measured signal. The signal per particle shows variations of about 20%, which we attribute to variations in the susceptibility of the individual particles.

References

- [1] M. Panhorst, P.B. Kamp, G. Reiss, and H. Brückl. Sensitive bondforce measurements of ligand-receptor pairs with magnetic beads. *Biosensors and Bioelectronics*, 20:1685–1689, 2005.
- [2] M.W.J. Prins and M. Megens. *Chapter in Encyclopedia of Materials: Science and Technology*, volume doi: 10.1016/B978-008043152-9/02146-1. Elsevier, 2007.
- [3] B.M. de Boer, J.A.H.M. Kahlman, T.P.G.H. Janssen, H. Duric, and J. Veen. An integrated and sensitive detection platform for magneto-resistive biosensors. *Biosensors and Bioelectronics*, 22:2366–2370, 2007.
- [4] M. Koets, T. van der Wijk, J.T.W.M. van Eemeren, A. van Amerongen,

- and M.W.J. Prins. Rapid DNA multi-analyte immunoassay on a magneto-resistance biosensor. *Biosensors and Bioelectronics*, 24(7):1893–1898, 2008.
- [5] W.U. Dittmer, P. de Kievit, M.W.J. Prins, J.L.M. Vissers, M.E.C. Mersch, and M.F.W.C. Martens. Sensitive and rapid immunoassay for parathyroid hormone using magnetic particle labels and magnetic actuation. *Journal of Immunological Methods*, 338:40–46, 2008.
- [6] T. Nelissen, W. Weekamp, J. Van Delft, W. Ansems, E. Janssen, M. Prins, M. Megens, R. Wiberger-Friedl, and B. Van Iersel. *Proceedings: 15th European Microelectronics and Packaging Conference and Exhibition, Brugge, Belgium*, 2005.
- [7] R. Wiberger-Friedl, T. Nelissen, W. Weekamp, J. van Delft, W. Ansems, M. Prins, M. Megens, W. Dittmer, C. de witz, and B. van Iersel. Packaging of silicon sensors for microfluidic bio-analytical applications. *Journal of Micromechanics and Microengineering*, 19, 2009.
- [8] M. Megens and M.W.J. Prins. Magnetic biochips: a new option for sensitive diagnostics. *Journal of Magnetism and Magnetic Materials*, 293:702–708, 2005.
- [9] M. Megens, F. de Theije, B. de Boer, and F. van Gaal. Scanning probe measurements on a magnetic bead biosensor. *Journal of Applied Physics*, 102:014507, 2007.
- [10] G. Fønnum, C. Johansson, A. Molteberg, S. Mørup, and E. Aksnes. Characterisation of Dynabeads by magnetization measurements and Mössbauer spectroscopy. *Journal of Magnetism and Magnetic Materials*, 293:41–47, 2005.
- [11] J.C. Rife, M.M. Miller, P.E. Sheehan, C.R. Tamanah, M. Tondra, and L.J. Withman. Design and performance of GMR sensors for the detection of magnetic microbeads in biosensors. *Sensors and Actuators A*, 107:209–218, 2003.
- [12] N.A. Patankar, P.y. Huang, T. Ko, and D.D. Joseph. Lift-off of a single particle in newtonian and viscoelastic fluids by direct numerical simulation. *Journal of Fluid Mechanics*, 438:67–100, 2001.
- [13] A. Ranzoni, X.J.A. Janssen, M. Ovsyanko, L.J. van IJzendoorn, and M.W.J. Prins. Magnetically controlled rotation and torque of uniaxial microactuators for lab-on-a-chip applications. *accepted for publication in Lab on a Chip*, 2009.

Chapter 4

Controlled pulling force on particles by magnetic field gradients

In this chapter we demonstrate how a well defined magnetic force can be applied to super-paramagnetic particles. A magnetic tweezers setup based on an electromagnet is developed to apply forces on magnetic particles. The force is calibrated directly from the movement the particles through the fluid. Using this setup, the influence of the ionic strength of the buffer on the non-specific binding of streptavidin coated particles to a glass substrate is studied. The binding shows a sigmoidal behavior on increasing ionic strength around 5 mM, which is qualitatively understood from increased shielding of the electrostatic repulsion between the particles and the surface.

4.1 Introduction

In chapter 1, pulling on magnetic particles is suggested as an actuation method to be used in a functional biosensor system. The on-chip detection and actuation of magnetic particles by locally applied magnetic forces has been demonstrated in chapter 3. The drawback of local actuation and detection is the limited amount of statistics since only a limited amount of particles (typically several dozens) can be used in a single experiment to avoid hydrodynamic as well as magnetic particle-to-particle interactions. Furthermore the integration of the actuator and sensor can become expensive especially since the cartridge is disposed of after every experiment.

To study a large number of particles (typically several hundreds) without particle-to-particle interactions, a magnetic tweezers setup is designed and build to apply translational forces to magnetic particles using an electromagnet (Fig. 4.1a). The magnet consists of a coil around a soft iron^[1] core with a tapered pole tip and is placed on top of the sample that is imaged from below. The advantage of using an electromagnet over a permanent magnet^[2] is the ability to apply varying forces without changing the configuration of the setup *i.e.* changing the position of the magnet.

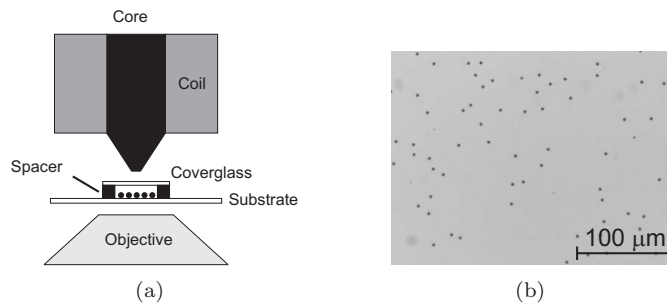


Fig. 4.1: (a) Schematic representation of the magnetic tweezers setup. The sample consists of a glass substrate with a spacer which creates a well with a diameter of 9 mm and depth of 0.12 mm. The height of the sample and size of the particles is largely exaggerated. (b) Cropped light microscopy image showing 2.8 μm particles on the glass substrate. The images used in the data analysis have a field of view of 700 μm × 550 μm.

The sample consists of a transparent substrate with a Secure-Seal spacer to create a well with a diameter of 9 mm and depth of 0.12 mm. After filling the well with particle solution, the well is covered with a glass coverslip (18 mm x 18 mm x 0.15 mm). Then the coil is placed on top of the sample and the sample is imaged from the bottom with an inverted microscope (Leica DMI 5000 M). A high speed camera (Redlake MotionPro X3) allows for video microscopy (Fig. 4.1b) that is synchronized with the coil control.

The magnetic force on the particles is dependent on a number of parameters that are difficult to control experimentally *e.g.* local magnetic field strength and gradient and the magnetic content of the particles. Therefore it is essential to develop a method to measure the force on the particles independently. In this chapter we show how a well defined magnetic force can be applied to super-paramagnetic particles. The force on the particles is calibrated directly from their speed through the fluid when they are pulled towards the pole tip of the magnet. In this procedure the microscope is focused at a given distance above the substrate and the magnetic field is switched on. The speed of the particles is determined by measuring the time of flight (TOF) over this distance. Finally the setup is used to study the influence of the ionic strength of the buffer on the non-specific binding of streptavidin coated particles to a glass substrate.

4.2 Experimental

4.2.1 Design

The magnetic field of the electromagnet is generated by a current running through the windings. The current I through the coil after instantaneously applying a voltage V is given by:

$$I(t) = \frac{V}{R_c} \left(1 - e^{-tR/L}\right) \quad (4.1)$$

with R_c the resistance, L the inductance of the coil and the steady state current (I_{max}) given by Ohm's law ($I_{max} = V/R$). The finite rise-time is caused by the induced electromotive force ($\epsilon = -L \frac{dI}{dt}$) that effectively lowers the applied voltage.

Although it is not feasible, for the interpretation of the measurements it is profitable when the magnetic force could be applied instantaneously. To reduce the finite rise-time of the step response, we developed a voltage-controlled push-pull current source (Fig. 4.2a). The output current (I_{out}) through the coil is given by the ratio of the input voltage (V_{in}) and the resistance of the sense resistor (R).

The controller allows to use a higher supply voltage than necessary to run the steady-state current ($V_{cc}^+ \gg \frac{I_{max}}{R_c}$). This higher voltage partially overcomes the electromotive force and by that decreases the rise-time. Once the desired current is reached, the voltage applied to the load is automatically reduced by the operational amplifier (Fig. 4.2b). For high currents, the reduction in rise-time becomes smaller since the difference between the supply voltage (V_{cc}^+) and the voltage at steady state ($V = I_{max}/R$) becomes smaller.

Experimentally, the supply voltage is limited to 25 V by the components used in the push-pull circuit and the coil resistance of 25 Ω therefore limits the current to 1 A. Apart from the reduction of the rise-time, the push-pull circuit also allows to easily apply time dependent currents for *e.g.* demagnetization of the coil and applying forces with a variable loading rate.

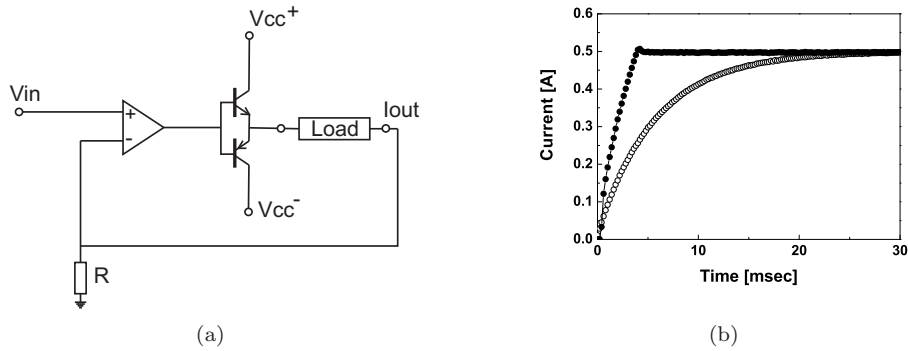


Fig. 4.2: (a) Schematic representation of the voltage-controlled push-pull current source to control the current through the electromagnet. The output current (I_{out}) through the load is equal to the the input voltage (V_{in}) divided by the resistance (R). (b) The current through the coil measured in time showing the step-response for a constant voltage of 12.5 V (\circ) and using the push-pull circuit with a supply voltage of 25 V (\bullet). The time until 95% of I_{max} is reduced by a factor 4 from 16 ms to 4 ms. Because the circuit is not critically damped, there is a small ($<2\%$) overshoot.

The magnetic field of the coil is measured as function of the applied current through the coil (Fig. 4.3a) using a Hall-probe (STH57-0404) connected to a Sypris Tesla meter (model 5070). The field can not be measured closer than 0.5 mm to the pole tip due to the dimensions of the probe. No saturation of the magnetic material is observed up to 1 A and a proportionality constant of 360 mT/A is found. Even though saturation is not reached, a remanent field of 2 mT is found when decreasing the current from 1 A back to zero.

The field at the central axis of the coil is measured using the Hall-probe and simulated in Comsol Multiphysics for increasing separation distance to the pole tip (Fig. 4.3b). The field gradient is calculated by numerical differentiation of the measured/simulated field with respect to the position. The measurements and simulations give comparable results although the measured field is slightly lower. This can be due to non-ideal packaging of the coils windings and the non-ideal magnetization curve of the soft iron core. Furthermore, the field decreases with increasing horizontal distance to the central axis and the Hall-probe effectively averages the field over the sensitive area (0.4 mm in diameter). The decreasing field gradient for small separation distance (< 0.25 mm) is caused by the finite width of the pole tip. For very small separation distance the tip can be approximated by a flat surface. Note that in the measurement on biological systems the surface of the substrate is at least 0.5 millimeter away from the pole tip due to the thickness of the substrate itself. The results of a Comsol Multiphysics simulation in figure 4.3c

show that the magnetic field decreases with increasing distance from the central axis of the coil. Note that in the experiments, the field of view of the microscope (smaller than $1 \text{ mm} \times 1 \text{ mm}$) is always centered around the central axis of the coil. Therefore in the interpretation of the results, the field is assumed to be constant over the field of view.

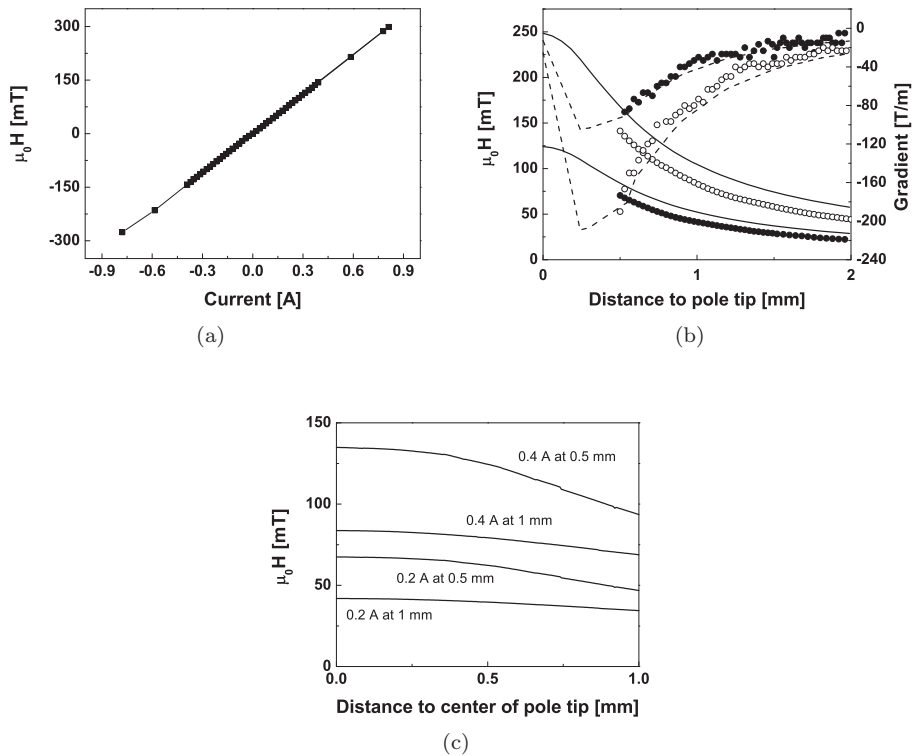


Fig. 4.3: (a) Measured field at a distance of 0.5 mm above the pole tip versus the current through the coil. (b) The measured field versus distance above the pole tip in steps of $30 \mu\text{m}$ for a current of 0.2 A (●) and 0.4 A (○). The magnetic field gradient is obtained by numerical differentiation of the magnetic field. The curves give the field (solid) and field gradient (dashed) versus distance as simulated in Comsol Multiphysics in steps of $30 \mu\text{m}$. Note that the kinks in the simulated field gradient result from the geometry of the slanted pole tip and not from a numerical artifact. (c) Comsol Multiphysics simulation of the magnetic field as function of the distance from the rotational symmetry axis of the pole tip for two different heights (0.5 mm and 1 mm above the pole tip) and two different currents through the coil (0.2 A and 0.4 A).

4.2.2 Direct force measurements

The magnetic force \vec{F}_{mag} on a magnetizable object is given by the integral over its volume V :^[3]

$$\vec{F}_{mag} = \mu_0 \int_V d^3r (\vec{M} \cdot \nabla) \vec{H}_0 \quad (4.2)$$

with \vec{M} the magnetization of the material and \vec{H}_0 the magnetic field in absence of the material.

The magnetization curve of the particles was given in figure 2.3. For the fields created by the electromagnet, the magnetization of the particles is not saturated, nor in the linear regime ($\vec{M} = \chi \vec{H}$). Therefore the force on the particles strongly depends on the field gradient as well as on the field strength. To rule out the uncertainty in the field strength, gradient and magnetization of the particles in the calculation of the force, we developed a technique to measure the magnetic force directly. This is done by studying the motion of the particles that leave the substrate and move through the fluid. The magnetic force can then be calculated from the viscous drag which limits the velocity of the particles.

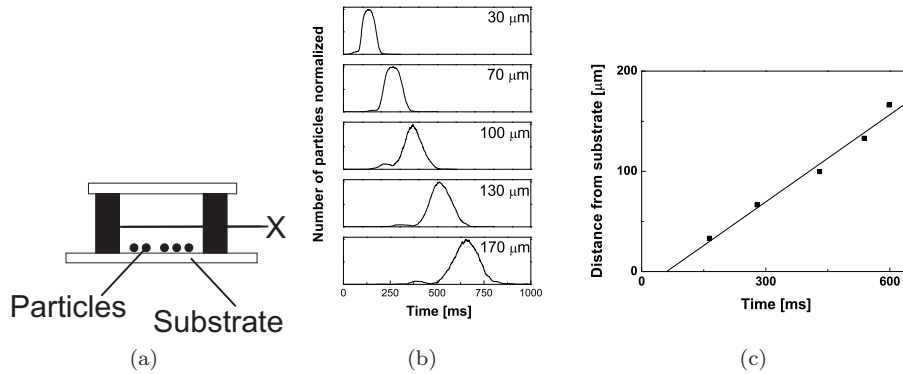


Fig. 4.4: (a) The focal plane of the microscope is positioned a distance (X) above the surface of the substrate and the particles are pulled away from the surface. Note that the height of the sample is largely exaggerated. (b) The normalized number of particles visible in the focal plane of the microscope versus time is sampled with a frame rate of 1 kHz. The maximum in the curve represents typically a few hundred particles. The distance X between the focal plane and the substrate is given by the numbers in the graph. (c) Linear fitting of the position of the particles versus time gives a speed of $290 \pm 5 \mu\text{m}/\text{sec}$ which corresponds to a magnetic force of $7.6 \pm 0.1 \text{ pN}$.

The experiments to measure the force on the particles were carried out by the following procedure. The well is filled with 10 μL of 200 times diluted particle solution and closed with a coverglass. After sedimentation for 5 minutes, all the particles are on the surface of the substrate (typically a few hundred). Note that the particles are not bound to the surface since no biological ligand-receptor system is present. The microscope is focussed at a distance X above the surface (Fig. 4.4a) and the particles are pulled away from the surface by "instantaneously" switching on the field using the designed push-pull circuit operating the coil of the electromagnet. The number of particles visible in the focal plane is determined using software written in Matlab and plotted versus time (Fig. 4.4b).

The peak broadening that is observed for increasing distance to the surface is understood from the particle-to-particle variations in the magnetic content of the particles *i.e.* particles with a higher/lower magnetic content move faster/slower than average. The presence of the second, smaller peak becomes more pronounced for increasing distance to the surface. This peak is located on the left side of the large peak, which means that these particles reach the focal plane earlier in time and therefore travel faster through the fluid. We attribute this second peak to the formation of strings of magnetically coupled particles. String formation is driven by dipole-dipole interaction between particles which takes place when the particles are initially close together, typically a few particle diameters. The strings are aligned with the magnetic field and move with their long axis perpendicular to the focal plane. The magnetic force on a string scales with the number of particles in the string, while the hydrodynamic drag increases less due to the slipstream effect. Derks *et al.*^[4] measured and simulated the increase in speed of a chain compared to the speed of a single particle. The velocity enhancement factor (VEF) is found to be:^[4]

$$VEF = 1 + 0.77 \ln(n) \quad (4.3)$$

with n the number of particles in the chain. For $n = 2$ and $n = 3$ the velocity increases respectively with a factor 1.5 and 1.8 compared to a single particle. From a multiple Gaussian peak fit, we obtain a ratio of 1.6 to 1.7 between the small and the large peak. Furthermore, it is observed that the peak attributed to the string formation vanishes when the number of particles on the substrate is decreased *i.e.* increasing the separation distance between the particles.

The experiment is repeated for various distances X and the distances are plotted versus the time at which the curves reaches their maximum (Fig. 4.4c). The magnetic force on the particle can now be determined from the velocity of the particle by evaluating the forces acting on the particle. The Stokes drag force F_D on a sphere with radius r moving with a speed \vec{v} through a fluid with viscosity η is given by:

$$\vec{F}_D = -6\pi\eta r \vec{v} \quad (4.4)$$

The equation of motion is given by Newton's second law:

$$m \vec{a} = \vec{F}_M + \vec{F}_D \quad (4.5)$$

with m the mass of the particle, \vec{a} its acceleration, \vec{F}_M the magnetic force and \vec{F}_D the drag force. The Reynolds number gives the relative importance of the inertial and viscous forces and is given by:

$$Re = \frac{\rho v D}{\eta} \quad (4.6)$$

with ρ the density of the fluid, v the characteristic velocity, D the characteristic length scale and η the dynamic viscosity of the fluid.

For a 2.8 μm particle moving at a velocity of 300 $\mu\text{m}/\text{sec}$ in water at room temperature the Reynolds number is typically $8 \cdot 10^{-4}$ indicating that the viscous forces dominate over the inertial forces. Now the magnetic force can be deduced from the measured velocity by neglecting the inertial forces:

$$\vec{F}_M = \vec{F}_D = 6\pi\eta r \vec{v} \quad (4.7)$$

It is observed that the linear fits of the distance that the particles traveled in time (Fig. 4.4c), persistently show a negative offset (typically -20 μm). We attribute this negative offset to the fact that Stokes' law as given in equation 4.4 is only valid in bulk fluid. Close to the surface, the particles experience an increased hydrodynamic drag due to an increase in the effective viscosity of the fluid. The increase in hydrodynamic drag can be understood since the presence of the impermeable wall hinders the fluid to be dragged along with the particle. As a consequence, a correction factor (λ) needs to be introduced in Stokes' law when the sphere is in close proximity of a wall:

$$\vec{F}_D = -6\pi\eta r \lambda \vec{v} \quad (4.8)$$

Happel and Brenner^[5] give an infinite series calculation for the correction term for a sphere moving perpendicular away from the surface of the wall in terms of the ratio of the sphere radius (r) and the distance (h) between the center of the sphere and the wall. Note that this correction is fundamentally different from Faxén's law that describes the situation in which the sphere moves parallel with a wall. An approximation for this infinite series of Happel and Brenner is given by Wakiya:^[5]

$$\lambda = \left[1 - \frac{9}{8} \frac{r}{h} + \frac{1}{2} \left(\frac{r}{h} \right)^3 \right]^{-1} \quad (4.9)$$

which agrees with the values computed by Happel and Brenner for $h/r > 2$.

Bevan and Prieve^[6] give an approximation of the infinite series that is also valid for $d > 0$:

$$\lambda = \frac{6d^2 + 9rd + 2r^2}{6d^2 + 2rd} \quad (4.10)$$

with $d = h - r$ the distance between the particle and the wall.

We simulated a sphere moving away from a no-slip wall in Comsol Multiphysics and the correction term for Stokes' law is plotted together with the aforementioned approximations of the infinite series calculation in figure 4.5a. Figure 4.5b shows the calculated position of a $2.8 \mu\text{m}$ particle in time when applying a constant force of 8 pN . The distance the particle has traveled after a given amount of time, is clearly dependent on the initial distance between the particle and the surface. Note that fitting of the linear part of the curves in figure 4.5b will result in a negative offset of the linear fit as is also observed when fitting our measurement data (Fig. 4.4c).

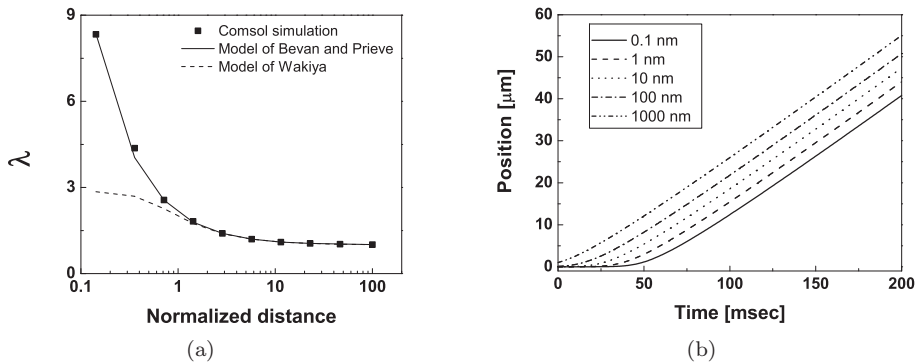


Fig. 4.5: (a) The correction term λ calculated from Comsol Multiphysics simulations together with two approximation of the infinite series calculation of Happel and Brenner. (b) Calculation of the position of a $2.8 \mu\text{m}$ sphere versus time when moving away from a surface under a constant force of 8 pN . The numbers in the legend give the initial distance between the sphere and the surface.

The initial distance between the particle and the surface is determined by various interactions like electrostatic repulsion/attraction, gravity and Brownian motion. Furthermore, the position of the focal plane with respect to the pole tip can only be determined with an accuracy of about $5 \mu\text{m}$ due to the finite depth of focus of the microscope objective and uncertainties in the refractive index of the glass and fluid. In the present imaging setup, we can therefore not accurately measure the initial distance between the individual particles and the surface. As a result, we can not correct the measured time-of-flight for the increased effective viscosity near the surface of the substrate.

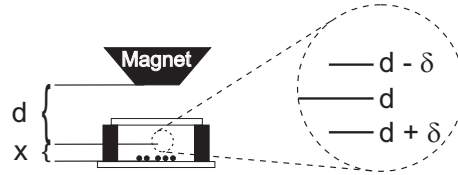


Fig. 4.6: We determined the speed of the particle over the interval $(d - \delta, d + \delta)$ by measuring the number of particles in time at three positions: $d - \delta$, d and $d + \delta$. The measurements are taken far enough ($x > 100 \mu\text{m}$) from the surface to ensure the validity of the bulk fluid approximation.

To solve this problem, we determined the speed of the particle over an interval $(d - \delta, d + \delta)$ by measuring the number of particles in time at three positions: $d - \delta$, d and $d + \delta$ as schematically shown in figure 4.6. The distances x , d and δ are measured and set using the computer controlled focus-drive of the microscope in combination with the "Leica Application Suite". The readout accuracy of this system is $1 \mu\text{m}$ but as mentioned before, experimentally the accuracy is typically $5 \mu\text{m}$ due to the finite depth of focus of the microscope objective and uncertainties in the refractive index of the glass and fluid. The measurements are taken far enough ($x > 100 \mu\text{m}$) from the surface to ensure the validity of the bulk fluid approximation. Since $\delta \ll d$, the force can be assumed constant over the interval and the magnetic force at position (d) is calculated using Stokes' law for bulk fluid (Eqn. 4.4). Using this technique, the magnetic force is determined over a large range by repeating this measurement for different distances (d) from the surface of the pole tip (Fig. 4.7a) and for different currents through the coil and a fixed distance (d) of 2.5 mm (Fig. 4.7b). By repeating the measurements it is found that the average force on the ensemble of particles can reproducibly be determined with an accuracy of 0.5 pN .

After the calibration, the pole tip is moved at least $100 \mu\text{m}$ closer to the substrate such that the surface of the substrate is located in the region where the force is calibrated. Note that in pulling experiments on bound particles, the viscous drag force plays no role since the particle is stationary and the net force applied to the particle is equal to the magnetic force. Furthermore each calibration is unique for the current through the coil and the particular type of particles. Therefore the calibration has to be repeated when using a different current or a different type of particles.

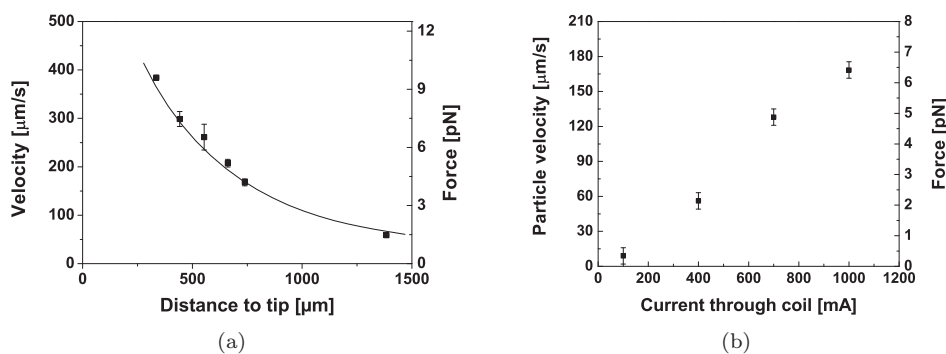


Fig. 4.7: (a) The velocity of the particles versus the distance to the pole tip for a current of 100 mA through the coil. The line is drawn to guide the eye. (b) The velocity of the particles at a distance of 2.5 mm from the pole tip versus the current through the coil. The right axes in both graphs show the corresponding magnetic force calculated using the viscous drag.

4.3 Non-specific binding of protein coated particles

The forces on the magnetic particle that were characterized in the previous section are used to measure the non-specific interaction of streptavidin coated particles with a glass substrate, for various ionic strengths of phosphate buffered saline (PBS) buffer. The cell is filled with 10 μL of standard particle solution diluted 200 times with phosphate buffered saline (PBS) of various ionic strengths. After sedimentation for 5 minutes, a magnetic force of 80 pN is applied to the particles and the number of particles is recorded in time (Fig. 4.8a). During the initial rapid decrease of the number of particles in the first 50 milliseconds, all the unbound (or weakly bound) particles are pulled away from the surface. It takes a few milliseconds before the unbound particles are out of the focal plane, which has a depth of focus of a few μm , wherein the particles are still detected by the image analysis software. After this initial fast decrease, the surface coverage decreases extremely slowly and reaches a quasi steady state that depends on the ionic strength of the solution.

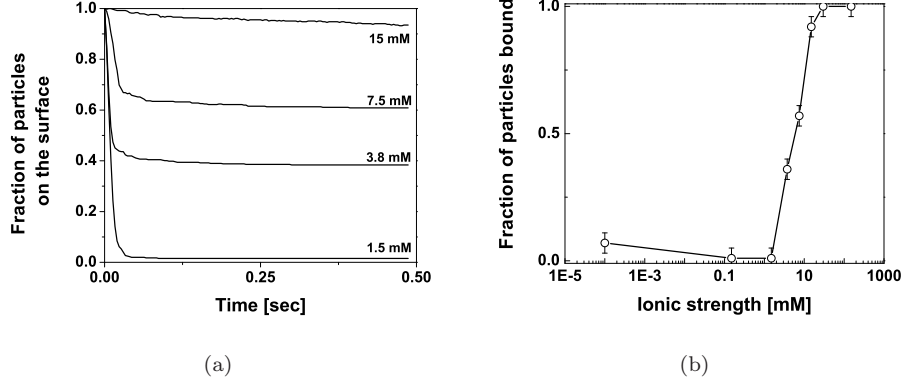


Fig. 4.8: (a) Fraction of particles on the surface versus time while applying a force for different values of the ionic strength of the buffer solution. After an initial rapid decrease, the fraction of particles present on the surface reaches a quasi steady state. (b) The quasi steady state fraction of bound particles (measured after 0.5 sec) versus the ionic strength of the solution. The fraction of particles bound to the substrate increases rapidly with the ionic strength increasing above 1 mM.

The number of bound particles in time was given in section 2.3 by:

$$N(t) = N(0) \exp(-k_d(f)t) \quad (4.11)$$

with $k_d(f)$ the force-dependent dissociation rate constant, characterized by a half-life:

$$t_{1/2} = \frac{\ln 2}{k_d(f)} \quad (4.12)$$

with $k_d(f) = \nu \exp \frac{-(E_b + fx_\beta)}{k_B T}$

The measurement time of the setup is limited to several seconds (depending on the current) due to Joule heating of the coil. Apparently the energy barrier (E_b) for dissociation results in a $t_{1/2}$ that exceeds our measurement time significantly and it is not possible to determine the dissociation rate constant from the measured curves (Fig. 4.8). In a new design, the magnet will be fitted with a water jacket for cooling which allows to increase the measurement time up to several minutes/hours.

If we plot the quasi steady state fraction of bound particles (measured after 0.5 s) at the surface versus the ionic strength of the solution, we obtain a sigmoidal curve that shows high binding for high ionic strengths (Fig. 4.8b). Apparently binding between streptavidin coated particles and a glass surface is highly depen-

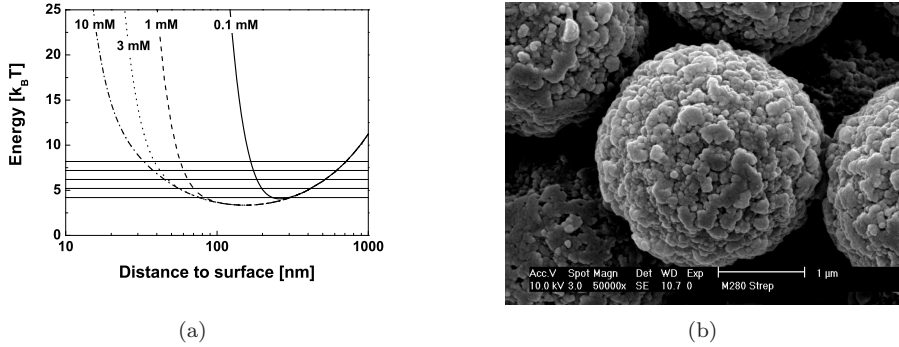


Fig. 4.9: (a) The total energy of a sphere versus the distance between the sphere and the surface for varying ionic strength of the fluid is calculated by summation of the gravitational, van der Waals (Hamaker constant $0.45 \cdot 10^{-20}$ J) and electrostatic energy (zeta-potential sphere/substrate -20 mV/ -30 mV). The horizontal lines are spaced $k_B T$ apart to give an indication of the freedom of movement of the sphere due to thermal energy. (b) Scanning electron microscopy (SEM) image of the 2.8 μm Dynal M-280 particles showing the surface roughness of the particle

dent on the ionic strength of the solution and most likely caused by electrostatic interactions.

It is known that the streptavidin coated Dynaparticles M-280 have a zeta potential of -20 mV at pH 7.0.^[7] Furthermore it is known that glass substrates have a negative surface charge at this pH where the zeta potential varies between -60 mV at an ionic strength of 10^{-3} mM up to -15 mV at 1 mM.^[8,9]

We calculated the electrostatic, van der Waals and gravitational energy of a sphere near a flat surface as function of the distance between the sphere and the surface. The electrostatic and van der Waals interaction as explained in section 2.3 are added to the gravitational energy E_g given by:

$$E_g = (\rho_{\text{sphere}} - \rho_{\text{fluid}})Vgh \quad (4.13)$$

with ρ_{fluid} the density of the fluid (1000 kg/m³ for water), ρ_{sphere} the density of the sphere (1400 kg/m³ for the material of Dynal particles), V the volume of the sphere ($1.15 \cdot 10^{-17}$ m³ for a diameter of 2.8 μm), g the gravitational acceleration (9.81 m/s²) and h the distance in meters between the surface and the sphere.

The balance between the repulsive and attractive forces keeps the sphere at a finite distance from the substrate. The electrostatic force becomes more shielded with increasing ionic strength causing the equilibrium height of the sphere to decrease (Fig. 4.9). Since the sphere has a thermal energy of several times $k_B T$, it can approach the surface closer than the distance at which the energy is minimal. Note that below the equilibrium height, the energy strongly increases with

decreasing distance which prevents the sphere from touching the surface. The observation that the particles bind to the surface for an ionic strength above 1 mM (Fig. 4.8b) together with the shape of the calculated energy curve (Fig. 4.9a) suggest that when the particles have a surface roughness of the order of 100 nm, the protruding parts can come in contact with the surface. Scanning electron microscopy images of the particle indeed confirm such a surface roughness of the particles (Fig. 4.9b). Note that only the approach of the particle to the surface is described by this theory and not the actual binding. The binding is most likely caused by short range interactions between the streptavidin and the surface. In the work of Korwin-Edson et al.^[10] it is suggested that streptavidin preferentially binds to OH-groups on the silica surface due to hydrogen bonding. To further validate the hypothesis that the distance between the particles and the surface is most likely dominated by electrostatic interactions, the non specific binding is studied in chapter 6 under different pH conditions using rotational actuation of the particles.

4.4 Conclusion

In summary, we have developed a magnetic tweezers setup that is able to apply magnetic forces on multiple super-paramagnetic particles in parallel. The magnetic force on the particles is measured directly from their speed through the fluid to account for the field dependent magnetization of the particles. The feasibility of the technique is shown by studying the non-specific interaction between streptavidin coated particles and a glass substrate. The non-specific binding is highly dependent on the ionic strength of the fluid and it is hypothesized that electrostatic repulsion between the particles and the substrate is shielded with increasing ionic strength. When the particles touch the surface, the particles bind non-specifically due to short range interactions.

References

- [1] Armco-Pure-Iron. Ak steel. www.aksteel.com.
- [2] H. Shang and G.U. Lee. Magnetic Tweezers Measurement of the Bond Lifetime-Force Behavior of the IgG-Protein A Specific Molecular Interaction. *Journal of the American Chemical Society*, 129(20):6640–6646, 2007.
- [3] A. Engel and R. Friedrichs. On the electromagnetic force on a polarizable body. *American Journal of Physics*, 70(4):428–432, 2002.
- [4] R.J.S. Derks, A. Dietzel, R. Wimberger-Friedl, and M.W.J. Prins. Magnetic bead manipulation in a sub-microliter fluid volume applicable for biosensing. *Microfluidics and Nanofluidics*, 3:141–149, 2007.

-
- [5] J. Happel and H. Brenner. *Low Reynolds number hydrodynamics*. Noordhoff International Publishing Leyden, the Netherlands, 2 edition, 1973.
 - [6] M.A. Bevan and D.C. Prieve. Hindered diffusion of colloidal particles very near to a wall. *Journal of Chemical Physics*, 113(3):1228–1236, 2000.
 - [7] Dynal-Biotech. *Dynabeads Streptavidin Products and Applications*, 2003.
 - [8] S.H. Behrens and D.G. Grier. The charge of glass and silica surfaces. *Journal of Chemical Physics*, 115(14):6716–6721, 2001.
 - [9] Y. Gu and D. Li. The ζ -potential of glass surface in contact with aqueous solutions. *Journal of Colloid and Interface Science*, 226:328–339, 2000.
 - [10] M.L. Korwin-Edson, A.G. Clare, M.M. Hall, and A. Goldstein. Biospecificity of glass surfaces: streptavidin attachment to silica. *Journal of Non-Crystalline Solids*, 349:260–266, 2004.

Chapter 5

Controlled torque on particles by rotating magnetic fields

We demonstrate that a rotating magnetic field can be used to apply a controlled torque on super-paramagnetic particles which leads to a tunable particle rotation frequency in fluid. Smooth rotation is obtained for field rotation frequencies many orders of magnitude higher than the particle rotation frequency. A quantitative model is developed, based on results from a comprehensive set of experiments at different field strengths and frequencies. At low frequencies (<10 Hz), rotation is caused by a small permanent magnetic moment in the particle. At high frequencies (kHz - MHz), the torque results from a phase lag between the applied field and the induced magnetic moment, caused by the non-zero relaxation time of the magnetic nanoparticles in the particle. The control of torque and rotation will enable novel functional assays in particle-based biosensors.

A condensed version of this chapter has been published as: X.J.A. Janssen, A.J. Schellekens, K. van Ommering, L.J. van IJzendoorn and M.W.J. Prins *Controlled torque on super-paramagnetic particles for functional biosensors* Biosensors and Bioelectronics **24**, 1937–1941 (2009)

The results presented in section 5.3.3. of this chapter form part of a more detailed study on the rotation of two-particle clusters: A. Ranzoni, X.J.A. Janssen, M. Ovsyanko, L.J. van IJzendoorn and M.W.J. Prins *Magnetically controlled rotation and torque of uniaxial microactuators for lab-on-a-chip applications* accepted for publication in Lab on a Chip

5.1 Introduction

In the previous two chapters particle manipulation with magnetic field gradients was demonstrated in both a compact biosensor with integrated current wires and in a flexible laboratory setup with an electromagnet. Magnetic field gradients induce a translational force on the particles which allows to study interactions between biochemical molecules. A complementary way to probe biological interactions is by applying a controlled torsion induced by rotation of a particle. Particle-based single-molecule experiments, using low frequency (\sim Hz) rotating magnetic fields, already showed novel types of experiments enabled by the application of a torsion to biological molecules.^[1–3] Although the degree of rotation was known in these single-molecule experiments, the quantitative value of the applied torque was not controlled. In fact, it is a surprise that a torque can be applied because in an idealized super-paramagnetic particle the magnetization and the applied magnetic field are parallel (section 2.1) and thus no magnetic torque can be applied. This raises the question which physical mechanism is responsible for torque generation and how the magnitude of the torque depends on the magnitude and frequency of the applied rotation field.

In this chapter, we show how a well-defined torque can be applied on super-paramagnetic particles. First the experimental setup that is used to apply rotating magnetic fields to particles is discussed. Then we unravel the mechanisms of torque generation by a comprehensive set of experiments at different field strengths and frequencies and develop a quantitative model to calculate the magnetic torque on super-paramagnetic particles.

5.2 Experimental

5.2.1 On-chip crossed wires

In order to study the rotation of particles, rotating magnetic fields have been induced using a chip with orthogonal current wires that do not interconnect. Two sets of eight current wires form a grid of 64 intersections. The current wires, each having a cross-section of $3\ \mu\text{m} \times 0.35\ \mu\text{m}$, are isolated from each other and from the fluid by a $0.5\ \mu\text{m}$ thick silicon nitride layer (Fig. 5.1a). In every experiment a single particle is confined above the intersection (Fig. 5.1b) by the magnetic potential well generated by the currents through the wires.^[4,5] Two sinusoidal currents that are 90 degrees out of phase induce a rotating magnetic field at angular frequency ω_f above the intersection of the two wires (Fig. 5.1b). The currents through both wires are balanced such that the generated field of both wires is equal in magnitude at the center of the $2.8\ \mu\text{m}$ particle *i.e.* $1.4\ \mu\text{m}$ above the surface of the chip. The balance was established as follows: using the equations given in chapter 3 it is calculated that the current ratio has to be 1.3 *i.e.* the amplitude of the current in the bottom wire is 1.3 times that of the current in the top wire. Field rotation

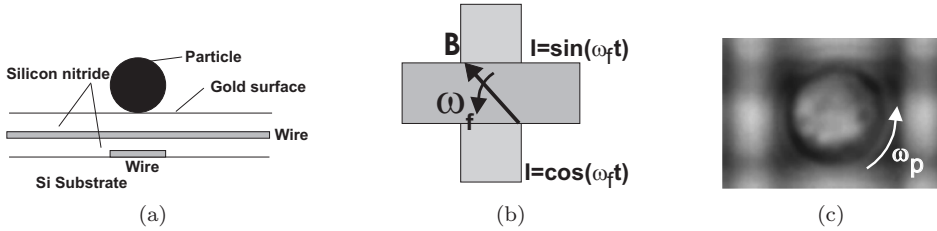


Fig. 5.1: (a) Cross-section of the chip which contains wires ($3 \mu\text{m} \times 0.35 \mu\text{m} \times 100 \mu\text{m}$) that are isolated from the fluid and from each other by a $0.5 \mu\text{m}$ thick silicon nitride layer. (b) Topview of a intersection of two wires. The two sinusoidal currents are 90 degrees out of phase to create a rotating magnetic field with an angular frequency ω_f . (c) Optical microscopy image of a $2.8 \mu\text{m}$ Dynal M-280 particle on two crossing wires (the edges of the wires are visible as dark line). The particle shows some visible features that allow detection of the rotation of the particle when it rotates with angular frequency ω_p .

frequencies between 0.1 Hz and 3 MHz can be achieved, at high frequencies limited by the impedance of the electrical system. The temperature rise of the wires due to Joule heating is measured to be less than 10°C for currents up to 100 mA .

The standard suspension of particles (Dynal M-280, diameter $2.8 \mu\text{m}$) is diluted 4000 times with de-ionized water and a droplet is placed on a silicon chip (as in the experiments described in section 3.3.1). After sedimentation of the particles more water is added to make contact to the long distance (3 mm) water immersion objective (Leica HXC APO L63X0.90 W U-V-I) of the microscope (Leica DM 6000M). The microscope is equipped with a camera (Redlake MotionPro HS-3) for high speed recording of the rotation of the particles. Figure 5.2 shows video microscopy images of a particle that rotates counter-clockwise. The images are recorded with a frame rate of 10 Hz and show a full rotation of the particle. It is observed that the image of the particle shows a characteristic pattern that allows the measurement of the angular displacement of the particle (Fig. 5.1c) using a 2D cross-correlation technique. Scanning electron microscopy (SEM) images (Fig. 5.3b) show the monodispersity of the particle size and also reveal that the pattern that is visible with optical microscopy most probably arises from the surface roughness of the particles (Fig. 5.3b).

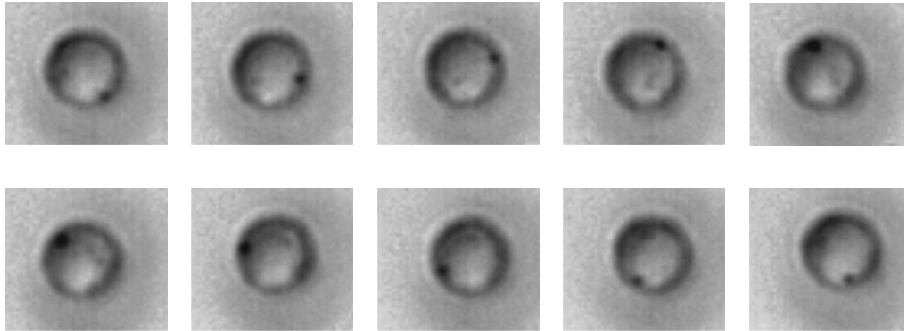


Fig. 5.2: Video microscopy images of a particle that rotates counter-clockwise recorded with a frame rate of 10 Hz (top left through bottom right). Note the dark spot visible on the particle that allows easy detection of the rotation angle of this particular particle.

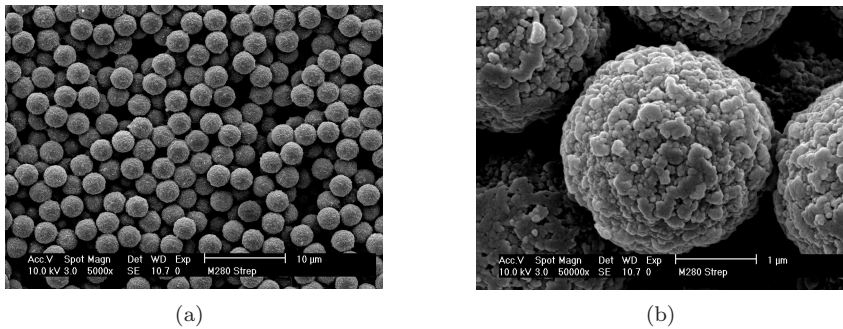


Fig. 5.3: (a) Scanning electron microscopy (SEM) image of the 2.8 μm Dynal M-280 particles showing the small spread in particle size. (b) Close-up of a single particle showing the surface roughness of the particle of about 100 nm.

5.2.2 Image analysis

The angular displacement of the particle is determined using a 2D cross-correlation technique. First, the center of the particle is determined using the cross-correlation technique described in chapter 3. Then the picture is transformed from Cartesian to polar coordinates around the center of the particle. The weighted average intensity $I(r, \theta)$ is calculated using:

$$I(r, \theta) = \Sigma I_i A_i \quad (5.1)$$

with I_i the intensity of the four neighboring pixels and A_i the areas of the rectangles as defined in figure 5.4.

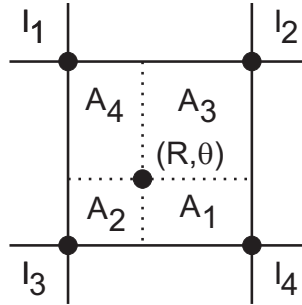


Fig. 5.4: Geometry used for the transformation from Cartesian to polar coordinates. The intensities I_i of the four neighboring pixels and the areas of the rectangles A_i are used to calculate the weighted average intensity $I(r, \theta) = \sum I_i A_i$.

The angular displacement between two pictures is determined by cross-correlation (in the θ -direction) of the transformed images as illustrated in figure 5.5. The maximum in the correlation-function then yields the mutual rotation angle between the two images.

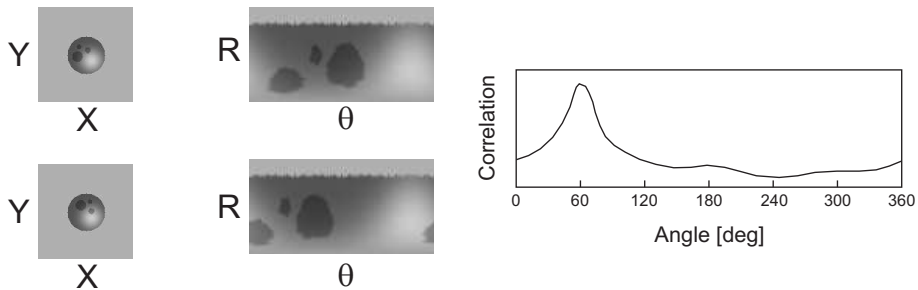


Fig. 5.5: Two artificial images of a particle that is rotated over 60 degrees (left) are first transformed to polar coordinates (middle). Then, the rotation angle is determined by cross-correlation in the θ -direction and the maximum in the correlation yields the mutual rotation angle of the particle between the two frames (right).

Note that the patterns of shades and highlights on the particle due to the illumination do not rotate with the particle (Fig. 5.5 left and middle). Depending on the amount of contrast in the features visible on the particle, these stationary patterns can negatively influence the outcome of the determination of the angular displacement. The software might detect no rotation since the vague pattern on the rotating particle is obscured by the stationary pattern. To minimize the influence of the stationary pattern, an average image is calculated from all the pictures in the movie and subtracted from each image prior to analysis. In this average image

all the stationary patterns are present while the pattern on the rotating particle is averaged out. So after subtraction of the average, the stationary patterns are removed while the pattern of the moving particle is preserved in each individual image.

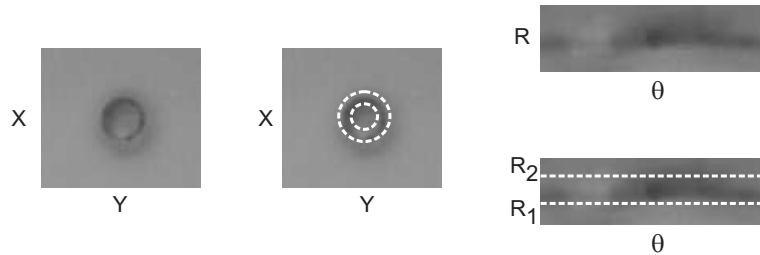


Fig. 5.6: Video microscopy image of a particle on the chip surface in Cartesian coordinates (left) and after transformation to polar coordinates (top right). The pattern that allows the detection of the rotation of the particle is particularly visible at the edge of the particle. The region between R_1 and R_2 that is selected and used in the 2D correlation technique is indicated by the two dotted circles (middle) and two dotted lines (bottom right).

Figure 5.6 shows an video microscopy image of a particle on the chip surface in Cartesian coordinates (top left) and after transformation to polar coordinates (top right). The pictures show that the pattern that allows the detection of the rotation of the particle is particularly visible at the edge of the particle. This region with the high contrast is selected (Fig. 5.6 bottom left and bottom right) and used in the 2D correlation technique in order to increase the angular resolution of the technique.

5.3 Results and discussion

5.3.1 Low frequency actuation

We measured the average angular rotation frequency of a particle over 20 full rotations as a function of the applied field frequency for various field strengths (Fig. 5.7a). The data show that the particle rotation frequency is proportional to the applied field frequency up to a so-called breakdown frequency, where a sharp drop of the particle rotation frequency is observed. To understand the mechanism driving the rotation of the particle, we need to consider the two torques acting on the particle: the magnetic torque driving the particle and the hydrodynamic torque counteracting the rotation. The magnetic torque $\vec{\tau}_{mag}$ on a magnetic moment \vec{m} placed in a magnetic field \vec{B} is given by:

$$\vec{\tau}_{mag} = \vec{m} \times \vec{B} \quad (5.2)$$

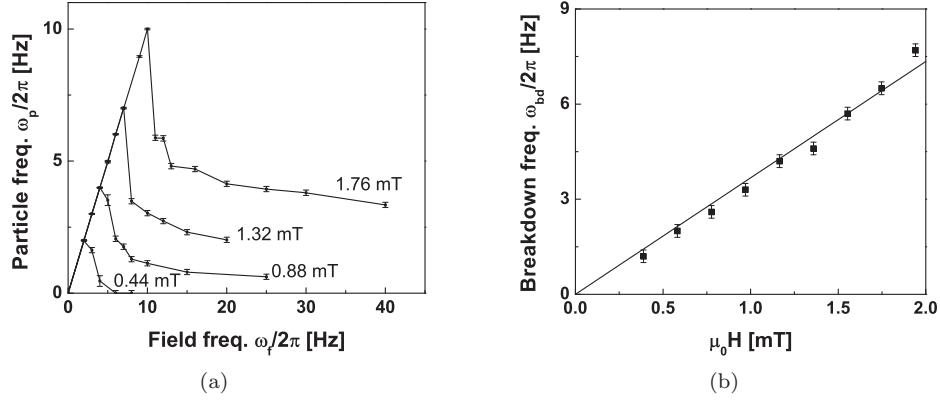


Fig. 5.7: (a) Average rotation frequency of the particle as function of the applied field for different field strength. The lines are plotted as a guide to the eye. (b) A systematic study of the breakdown frequency versus the applied field strength with a linear fit of the data (measured on another particle).

The hydrodynamic torque $\vec{\tau}_{hydro}$ on a sphere with a radius R rotating at a frequency $\vec{\omega}$ in bulk fluid with dynamic viscosity η is given by:

$$\vec{\tau}_{hydro} = -8\pi\eta R^3 \vec{\omega} \quad (5.3)$$

At the breakdown frequency the angular rotation frequency of the particle reaches a maximum and consequently the hydrodynamic torque is maximum. Interestingly the breakdown frequency scales linearly with the applied magnetic field (Fig. 5.7b). This implies that the maximum magnetic torque that is applied to the particle increases linearly with the applied field.

Note that in this experiment, the particles are not rotating in bulk fluid but close to the surface of the chip. Finite element simulations (Comsol Multiphysics) of a rotating sphere close to a no-slip wall have been performed to study the influence of the proximity of the wall on the hydrodynamic drag. The rotational drag coefficient is calculated as a function of the distance between the bottom of the sphere and the wall (Fig. 5.8) and normalized on the drag coefficient in bulk fluid ($8\pi\eta R^3$). For a large distance (10 times the radius of the sphere) between the sphere and the surface, the normalized rotational drag coefficient is close to unity indicating that the bulk drag coefficient is reached. The increase in rotational drag coefficient for decreasing distance is caused by the wall that slows down the fluid that is dragged around by the rotating sphere. This effect can be interpreted as an increase of the effective viscosity of the fluid. A salient detail in figure 5.8 is the finite value of about 1.23 of the relative drag coefficient for a close proximity between the particle and the surface. This can be explained as follows: in the simulations, the contact point between the sphere and the surface is infinitely

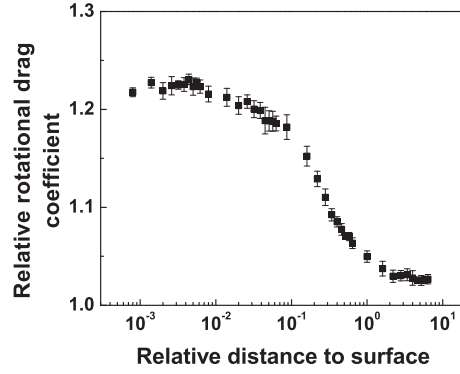


Fig. 5.8: Calculated rotational drag coefficient of a rotating sphere close to a no-slip wall. The distance from the bottom of the sphere to the surface is normalized to the radius of the sphere and the drag coefficient is normalized on the rotational drag coefficient in bulk fluid ($8\pi\eta R^3$).

small and stationary since it is located on the rotation axis of the sphere. So even if the two no-slip surfaces are in contact, no friction is present and the drag coefficient is still determined by the fluid between the sphere and the surface.

Since the exact height of the particle above the surface is not known in the experiments, we introduce the hydrodynamic drag coefficient λ in the hydrodynamic torque ($\vec{\tau}_{hydro} = -\lambda\vec{\omega}_p$). The rotation of the particle can now be understood from solving the equation of motion given by:

$$I \frac{d\vec{\omega}_p}{dt} = \tau_{mag} + \tau_{hydro} = \vec{m} \times \mu_0 \vec{H} - \lambda \vec{\omega}_p \quad (5.4)$$

with I the moment of inertia of the particle.

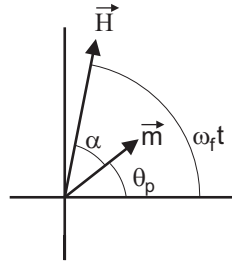


Fig. 5.9: Schematic representation of a magnetic moment m in a magnetic field H rotating at frequency ω_f . θ_p indicates the orientation between the frame of reference and the magnetic moment. α indicates the angle between the moment and the field.

Neglecting the inertial forces (Taylor number $T_a = \frac{4\omega_p^2 R^3}{\nu} \approx 10^{-6}$ for a $2.8 \mu\text{m}$ particle rotating at 20 Hz in water at 20°C) and introducing the angular velocity of the field ω_f and the angle of the particle with respect to the frame of reference θ_p (Fig. 5.9), the equation of motion becomes:

$$m\mu_0 H \sin(\omega_f t - \theta_p) = \lambda \frac{d\theta_p}{dt} \quad (5.5)$$

Note that the arrows indicating the vector property of the variables are left out for clarity. At each moment in time the magnetic torque and the hydrodynamic torque are in balance. For frequencies below the breakdown frequency, the rotation frequency of the particle is equal to the frequency of the field. The increase in magnetic torque necessary for the particle to follow a higher field frequency can only be obtained if the angle between the magnetic moment and the field increases. At the breakdown frequency the magnetic torque is maximum [$\sin(\omega_f t - \theta_p) = 1$] and the magnetic field is perpendicular to the magnetic moment. As mentioned before, the breakdown frequency scales linearly with the applied magnetic field (Fig. 5.7b). This implies that the maximum magnetic torque increases linearly with the applied field. Apparently, in this frequency range, the torque is caused by a field independent magnetic moment in the particle. This permanent magnetic moment can now be derived from fitting the breakdown frequency as function of the applied field using:

$$m_{perm} = \frac{\lambda \omega_{breakdown}}{\mu_0 H} \quad (5.6)$$

The exact height of the particle above the surface is not known, but we can estimate a lower limit of the magnetic moment. By using the drag constant for a particle in a bulk fluid ($\lambda = 8\pi\eta R^3$) with $\eta = 1 \cdot 10^{-3} \text{ Pa s}$ and $R = 1.4 \mu\text{m}$ and the results plotted in figure 5.7b, a permanent magnetic moment of $1.8 \cdot 10^{-15} \text{ Am}^2$ is found. This corresponds to approximately 1% of the saturation magnetic moment of the particle. Apparently, a part of the magnetic material inside the particle is not able to align its magnetic moment with the applied field instantaneously and can be considered as permanently magnetized on the timescale of the experiment. Interestingly the magnetization curves obtained by vibrating sample magnetometry (VSM) as shown in figure 2.3a and by Fonnum *et al.*,^[6] show no coercivity or remanence and from these measurements one might conclude that the particles have no permanent magnetic moment. However, VSM measurements can only be done with a substantial amount of magnetic material. Due to random orientations of the particles and the small size of the permanent magnetic moment (about 1% of the saturation magnetization), the permanent moments of the particles are not visible in the VSM measurements.

We have characterized a number of particles and observed the permanent moment to vary from $2 \cdot 10^{-16} \text{ Am}^2$ up to $2.5 \cdot 10^{-15} \text{ Am}^2$. In section 2.1 it is mentioned

that the lack of magnetic moment in absence of a magnetic field prohibits clustering and is one of the advantages of using super-paramagnetic particles as labels in immunoassays. In spite of the presence of the small permanent magnetic moment proven by the particle rotation experiments, particle clustering is not observed.

The interaction of the permanent magnetic moment of two particles can be approximated by assuming two dipoles at the center of the two particles. The magnetic energy of two interacting dipoles (E_{d-d}) is given by :

$$E_{d-d} = \frac{\mu_0}{4\pi} \frac{\vec{m}_1 \cdot \vec{m}_2}{|r^3|} \quad (5.7)$$

where \vec{m}_1 and \vec{m}_2 are the individual dipole moments and r the distance between the two dipoles. It is now possible to calculate a magnetic moment ($m_{critical}$) at which the dipole-dipole energy is equal to the kinetic energy k_bT assuming $|\vec{m}_1| = |\vec{m}_2| = m_{critical}$:

$$m_{critical} = \sqrt{\frac{4\pi k_B T r^3}{\mu_0}} \quad (5.8)$$

Assuming that each particle behaves as a single dipole and assuming a minimum distance of $2.8 \mu\text{m}$, a critical magnetic moment of $2.2 \cdot 10^{-15} \text{ Am}^2$ is found. So when the average magnetic moment of the two particles is below this critical value, the particle will not cluster due to thermal energy. The average permanent magnetic moment as found in the particle rotation experiments ($1.3 \cdot 10^{-15} \text{ Am}^2$) is close to but smaller than the critical value which agrees with the observation that no clusters are formed in absence of a magnetic field.

A more detailed understanding of the particle rotation can be obtained by rewriting equation 5.5:

$$\frac{d\theta_p}{dt} = \omega_{BD} \sin(\omega_f t - \theta_p) \quad (5.9)$$

with $\omega_{BD} = \frac{m_{perm} B}{\lambda}$. This differential equation is solved numerically and the cumulative angle of the particle is plotted in figure 5.10a for four different field frequencies. The differential equation is solved for a breakdown frequency of 11 Hz ($\frac{\omega_{BD}}{2\pi} = 11 \text{ Hz}$) in order to make a quantitative comparison with the measurement as shown in figure 5.10b. The calculated cumulative angle increases linearly in time for field frequencies below or equal to the breakdown frequency (Fig. 5.10a cases A and B). Consequently, the particle rotates at the same frequency as the applied field ($\omega_f < 11 \text{ Hz}$ in Fig. 5.10b).

If a field frequency above the breakdown frequency is applied (Fig. 5.10a cases C and D), the magnetic torque is not large enough to drag the particle through the fluid at this high frequency. Now the particle follows the rotating magnetic field for a short period of time. Due to the difference in rotation rate between the

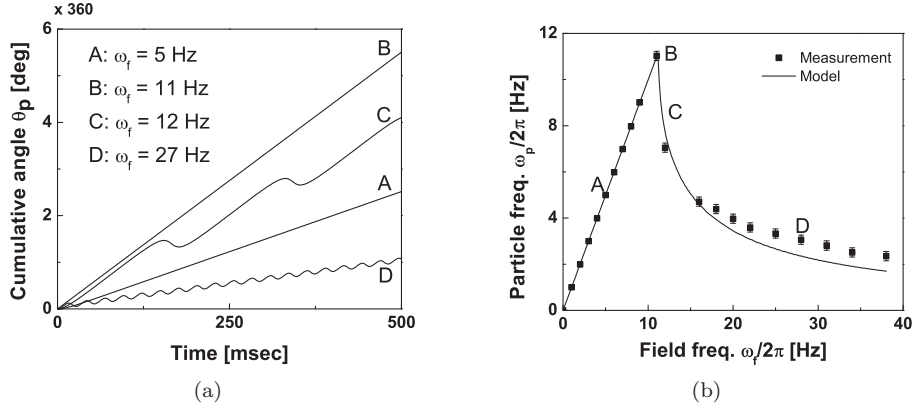


Fig. 5.10: (a) Cumulative angle of a particle in time for four different field frequencies ω_f and for a breakdown frequency $\omega_{BD} = \frac{mB}{\lambda}$ of 11 Hz. (b) Measurement of the average particle rotation frequency (dots) and the model based on the permanent magnetic moment (line). The letters A to D in both panels correspond to each other.

field and the particle, the particle starts lagging behind and the angle between the field and the magnetic moment increases. When the angle becomes larger than 90 degrees, the magnetic torque decreases and the particle slows down. Once the angle exceeds 180 degrees, the particle starts to rotate in the opposite direction. Now the angle between the field and the magnetic moment decreases rapidly, up to the point where the moment is caught up by the field and the cycle restarts. For higher frequencies, the asymmetry between the forward (same direction as the field) and backward (against the direction of the field) rotation becomes smaller causing the net particle frequency to decrease ($\omega_f > 11$ Hz in Fig. 5.10b).

The model based on the permanent magnetic moment reproduces the measured average rotation frequency of the particle over the whole range of applied frequencies (Fig. 5.10b). Note that the breakdown frequency ($\omega_{BD} = \frac{mB}{\lambda}$) is the only parameter used in fitting the model to the data. A closer look at the measured cumulative angle of the particle indeed shows phases of forward and backward rotation upon excitation above the breakdown frequency (Fig. 5.11). For a field frequency of 1 Hz, the magnetic torque is small and the movement of the particle is clearly influenced by Brownian motion *i.e.* without Brownian motion the cumulative angle would increase linearly in time resulting in a straight curve. For a higher field frequency (2 Hz) the magnetic torque dominates the Brownian motion and a more straight curve is measured. When the field frequency is above the breakdown frequency the behavior of the particle becomes instable due to the changes in rotation direction and the Brownian motion becomes more significant again.

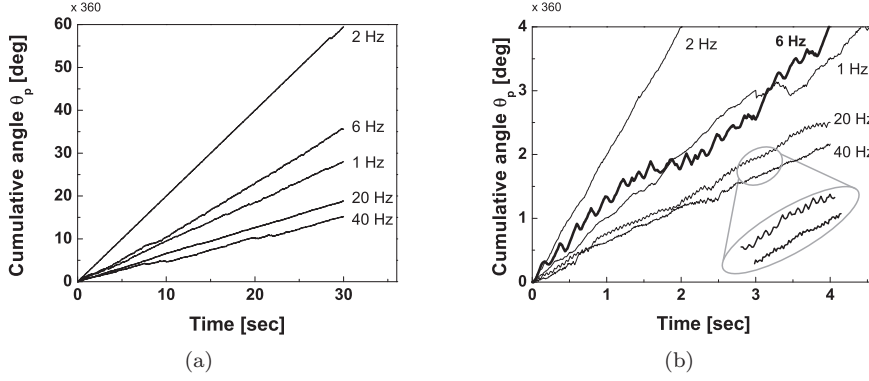


Fig. 5.11: (a) Cumulative angle of the particle measured for different field frequencies (given by the numbers in the graph) over 30 seconds. (b) Close-up of the first four seconds clearly shows the periods of forward and backward rotation upon excitation above the breakdown frequency of about 4 Hz. The influence of Brownian motion on the measured cumulative angle is clearly visible, especially in the curve measured with a field frequency of 1 Hz. The ellipse in bottom right corner shows a close up of the curves measured at a field frequency of 20 Hz and 40 Hz.

The asymmetry between the phases of forward and backward rotation can be calculated by introducing the angle α between the field and the magnetic moment $\alpha = \omega_f t - \theta_p$ (illustrated in figure 5.9) in the differential equation:

$$\omega_f - \frac{d\alpha}{dt} = \omega_{BD} \sin(\alpha) \quad (5.10)$$

The time during which the particles rotates in a forward (t_f) and backward direction (t_b) is calculated by integration over the angle α . The particle follows the field as long as the angle between the field and magnetic moment is smaller than π whereas the particle rotates backward once the angle is above π :

$$t_f = \int_{\alpha=0}^{\alpha=\pi} \frac{d\alpha}{\omega_f - \omega_{BD} \sin(\alpha)} = \frac{2}{\sqrt{\omega_f^2 - \omega_{BD}^2}} \left[\frac{\pi}{2} + \arctan \left(\frac{\omega_{BD}}{\sqrt{\omega_f^2 - \omega_{BD}^2}} \right) \right] \quad (5.11)$$

$$t_b = \int_{\alpha=\pi}^{\alpha=2\pi} \frac{d\alpha}{\omega_f - \omega_{BD} \sin(\alpha)} = \frac{2}{\sqrt{\omega_f^2 - \omega_{BD}^2}} \left[\frac{\pi}{2} - \arctan \left(\frac{\omega_{BD}}{\sqrt{\omega_f^2 - \omega_{BD}^2}} \right) \right] \quad (5.12)$$

Note that the equations are similar except the change in sign of the inverse tangent.

The frequency at which the particle alters its direction of motion is defined as the wiggle frequency:

$$\omega_{wiggle} = \frac{2\pi}{t_{forward} + t_{backward}} = \sqrt{\omega_f^2 - \omega_{BD}^2} \quad (5.13)$$

As mentioned before, the breakdown frequency is determined by measuring the particle rotation frequency for different field frequencies. Consequently, the uncertainty in the found permanent magnetic moment depends on the accuracy at which the breakdown frequency is determined. A more accurate determination of the breakdown frequency demands for smaller steps in the field frequency around point B in figure 5.10b which makes a highly accurate determination of the permanent moment very elaborate.

In theory, the direct relation between the wiggle frequency, breakdown frequency and the field frequency allows for a faster determination of the breakdown frequency from a single measurement instead of a series of measurements at different frequencies. First the field frequency is continuously increased until the particle shows the oscillating behavior. Then the oscillating angular orientation of the particle is recorded for a certain period of time and the wiggle frequency is determined by a Fourier analysis of the measured angular orientation of the particle. From this wiggle frequency, the breakdown frequency and by that the permanent magnetic moment can be calculated. In practice however it is found that the wiggles show some irregular movements due to Brownian motion of the particle (Fig. 5.11b), which results in a low frequency resolution in the Fourier spectrum.

An alternative procedure to determine the permanent moment more accurately is based on the relation between the average particle frequency and the wiggle frequency. Each time the field overtakes the permanent magnetic moment, the particle shows a period of backward rotation. Therefore the frequency at which the wiggles appear is also equal to the field frequency minus the average particle frequency ($\omega_{p,avg}$):

$$\omega_{wiggle} = \omega_f - \omega_{p,avg} \quad (5.14)$$

By rewriting this equation, a relationship between the average particle frequency and the breakdown frequency is found:

$$\omega_{p,avg} = \omega_f - \omega_{wiggle} = \omega_f - \sqrt{\omega_f^2 - \omega_{BD}^2} \quad (5.15)$$

Using this relationship, the breakdown frequency can easily be determined by linearly fitting the measured cumulative angular orientation of the particle in time.

Table 5.1 gives a comparison of the values of the permanent magnetic moment as found by applying the three aforementioned techniques on the same data set to avoid particle-to-particle variation in the magnetic moment.

Table 5.1: The values of the permanent magnetic moment as found by applying the three aforementioned techniques to the same data set. Note that in principle the accuracy of the first technique can be improved by making smaller steps in the field frequency but this makes an accurate determination of the permanent moment very elaborate.

Technique	magnetic moment $m_{perm}/10^{-16}$ [Am ²]
Stepwise increasing the field frequency	2.8 ± 0.3
Fourier analysis of the wiggle frequency	2.7 ± 0.5
Linear fitting of average particle frequency	2.7 ± 0.2

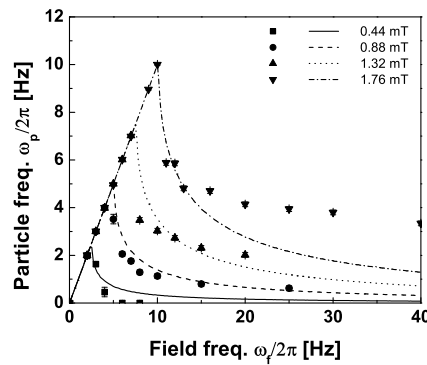


Fig. 5.12: The measured frequency at which the particle rotates plotted versus the field frequency. The data points are fitted with the model based on a permanent magnetic moment of the particle. Note that the model deviates from the measured points for increasing field strength at high frequencies.

To summarize, we have shown that the Dynal M-280 particles follow a rotating magnetic field due to the presence of a small permanent magnetic moment. The permanent magnetic moment is determined by studying the rotational behavior of the particle when applying a rotating magnetic field and is found to be of the order of 10^{-15} Am². This corresponds to approximately 1% of the saturation magnetic moment of the particle. The model based on a permanent magnetic

moment fits the measured frequency response of the particle, but for increasing field frequency, the measured particle rotation frequency decreases slower than the simulated particle rotation frequency (Fig. 5.12). It is observed that this deviation becomes larger for increasing field frequency and field strength.

5.3.2 High frequency actuation

In this section we study the aforementioned deviation of the model for high field strength and high field frequency. The particle rotation frequency was measured at rotation frequencies of the magnetic field ranging from 0.1 Hz to 3 MHz (Fig. 5.13a).

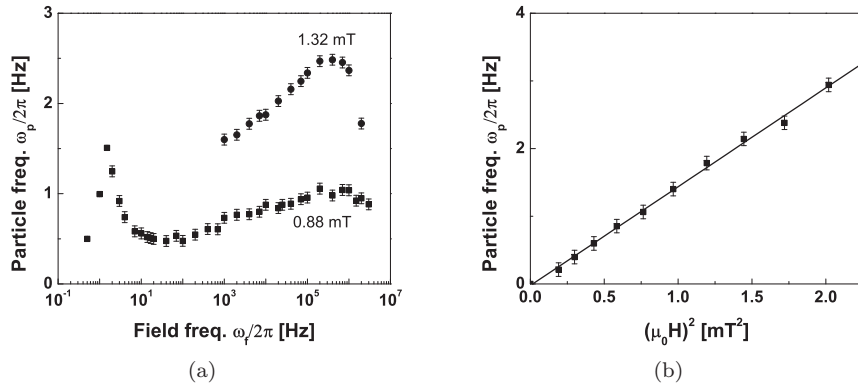


Fig. 5.13: (a) Average rotation frequency of the particle versus the field frequency at two different field strengths. (b) Average rotation frequency of the particle at a field frequency of 40 kHz versus the square of the field strength.

To our surprise, the particle rotation frequency increases for field frequencies between approximately 100 Hz and 400 kHz and decreases again for even higher field frequencies. This rise in rotation frequency cannot be explained by the model based on the permanent magnetic moment. Apparently for low and high field frequencies two different physical mechanisms dictate the particle rotation behavior.

Since the M-280 particles consist of a non-uniform composite material of magnetic nanoparticles, the torque on the particle might result from small individual torques on each individual nanoparticle. Kurlyandskaya *et al.* showed rotation of individual nanoparticles by applying high frequency (\sim MHz) magnetic fields on ferrofluids. The rotation of the magnetic moment and/or physical rotation of the nanoparticles was found to be dependent on the strength of the applied magnetic field.^[7]

The physical mechanism underlying the increase in particle rotation frequency in our experiments at high field frequencies was investigated by studying the dependence on the field strength (Fig. 5.13b). At frequencies above 100 Hz we found

a quadratic increase in particle rotation frequency with increasing field strength. This indicates that the torque $\vec{\tau} = \vec{m} \times \vec{B}$ is caused by a field induced magnetization *i.e.* $\vec{m} \propto \vec{B}$. Note that the observation of a torque acting on the particle implies that in the high frequency range, the induced magnetization is not parallel to the applied field.

The phase lag between the field and the magnetization can be derived from the magnetic relaxation time τ of an iron oxide nanoparticle in an external field with magnetic flux density B :

$$\tau = \nu_0^{-1} \exp \frac{KV \pm mB}{k_B T} \quad (5.16)$$

with ν_0 the attempt frequency, K the magnetic anisotropy constant, V the volume of the ironoxide nanoparticle, m the magnetic dipole moment of the nanoparticle and k_B the Boltzmann constant. For nanoparticles made of magnetite with a saturation magnetization of $5 \cdot 10^5 \text{ J/m}^3$ ^[8] and an anisotropy constant K of $2 \cdot 10^4 \text{ J/m}^3$,^[9] the ratio between the magnetic energy and the anisotropy energy is: $\frac{KV}{mB} \approx \frac{4 \cdot 10^{-2}}{B}$. So for an applied magnetic flux density of the order of 1 mT, this ratio is 40 and the anisotropy energy KV dominates the magnetic relaxation time.

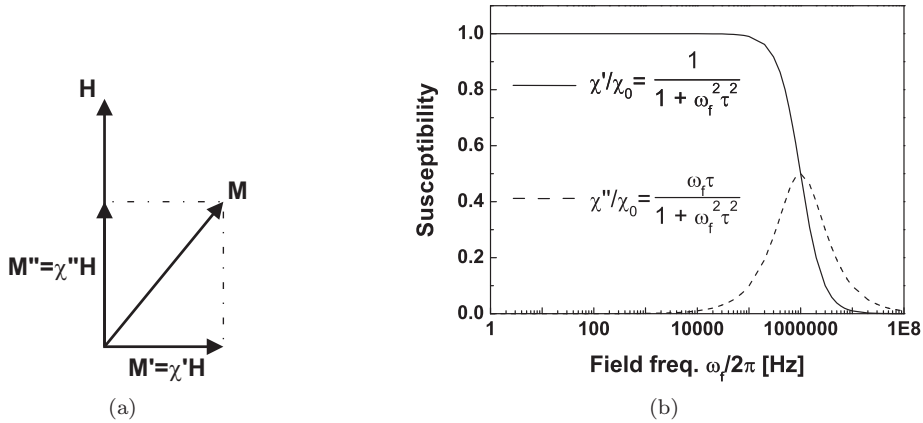


Fig. 5.14: (a) The frequency dependent magnetization (M) of a particle can be expressed as a complex vector: $M(\omega_f) = (\chi'(\omega_f) - i\chi''(\omega_f))H$. (b). The real (χ') and imaginary (χ'') part of the susceptibility normalized to the susceptibility at static field χ_0 .

Since the magnetization lags behind on the applied rotating magnetic field, the magnetization can be expressed as a complex vector: $\vec{M}(\omega_f) = (\chi'(\omega_f) - i\chi''(\omega_f))\vec{H}$ using the Kramers-Kronig relations.^[10] The magnetization and the field are schematically represented in figure 5.14a.

For an ensemble of monodisperse nanoparticles the complex susceptibility is given by:^[11]

$$\chi(\omega_f) = \chi_0 \frac{1}{1 + i\omega_f\tau} \quad (5.17)$$

with χ_0 the susceptibility of the nanoparticle material at static field (Fig. 5.14b).

The rotating field that is applied in the experiments can be decomposed in two orthogonal directions (x and y), where the field in the x-direction is given by:

$$H_x = H \cos \omega t \quad (5.18)$$

The magnetic field induces a magnetization \mathbf{M}_x that lags behind in time with respect to the field:

$$M_x = M \cos(\omega t - \theta) = M(\cos \omega t \cos \theta + \sin \omega t \sin \theta) \quad (5.19)$$

Introducing χ' as the proportionality constant for the component of the magnetization that is in phase with the field and χ'' as the proportionality constant for the component of the magnetization that is $\frac{\pi}{2}$ out of phase, Eqn. 5.19 becomes:

$$M_x = H(\chi' \cos \omega t + \chi'' \sin \omega t) \quad (5.20)$$

Equal for the y-direction:

$$H_y = H \sin \omega t \quad (5.21)$$

$$M_y = H(\chi' \sin \omega t - \chi'' \cos \omega t) \quad (5.22)$$

In vector notation the field and magnetization are given by :

$$\mathbf{H} = H(\cos \omega t)\mathbf{e}_x + H(\sin \omega t)\mathbf{e}_y + 0\mathbf{e}_z \quad (5.23)$$

and

$$\mathbf{M} = H(\chi' \cos \omega t + \chi'' \sin \omega t)\mathbf{e}_x + H(\chi' \sin \omega t - \chi'' \cos \omega t)\mathbf{e}_y + 0\mathbf{e}_z \quad (5.24)$$

The torque density is given by the vector product of the magnetization and the field. The torque on a volume (V) filled with nanoparticles is given by:

$$|\tau| = V|\vec{M} \times \mu_0 \vec{H}| = \mu_0 \chi'' H^2 V \quad (5.25)$$

Note that the torque is proportional to the square of the applied field and to the imaginary part of the susceptibility. The magnetization caused by the real part of the susceptibility is parallel to the applied field and does therefore not contribute to the torque, whereas the magnetization caused by the imaginary part

of the susceptibility does contribute to the torque because it is perpendicular to the applied field.

To calculate the torque on a particle, it is important to consider the fact that the particle contains a distribution of ironoxide nanoparticles with different sizes and thus different relaxation times. Neither the number of nanoparticles inside a particle nor the size distribution is given by the manufacturer of the particles. We therefore modeled the resulting imaginary susceptibility by using a log-normal nanoparticle size distribution, which is commonly observed in the synthesis of magnetic nanoparticles.^[12] The distribution is divided in n size intervals, each with a total volume V_n . Each interval contributes to the total susceptibility with weight factor V_n^2 .^[13]

The total imaginary susceptibility of the particle becomes:

$$\chi''(\omega_f) = \frac{\chi_{particle}}{\sum_n V_n^2} \sum_n \frac{\omega_f \tau_{m,n}}{1 + \omega_f^2 \tau_{m,n}^2} \cdot V_n^2 \quad (5.26)$$

where we normalized the complex susceptibility to the particle susceptibility at static field. The torque due to the induced magnetic moment is added to the equation of motion (Eqn. 5.5) resulting in:

$$m_{perm} \mu_0 H \sin(\omega_f t - \theta_p) + \chi''(\omega_f) \mu_0 H^2 V = \lambda \frac{d\theta_p}{dt} \quad (5.27)$$

with V the volume of the magnetic content of the particle.

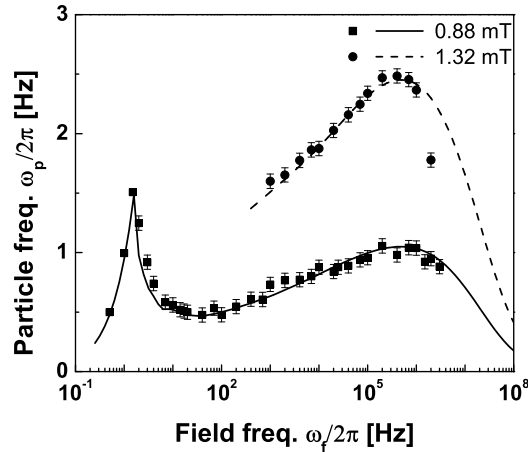


Fig. 5.15: Frequency response of a magnetic particle measured at two different values of the applied field. The two data sets are fitted using Eqn. 5.27. The only difference between the two curves is the magnitude of the applied magnetic field.

Using this equation of motion and the complex susceptibility of the particle (Eqn. 5.26), we can fit the measured particle rotation frequency assuming an anisotropy constant K of $5 \cdot 10^4 \text{ J/m}^3$,^[9] χ_0 of 0.64 and a log-normal distribution with a mean nanoparticle radius r_m of 3.8 nm^[6] and a standard deviation σ of 0.26 nm. It appears that the position of the peak at high frequencies is primarily determined by the anisotropy constant and the mean nanoparticle radius, while the width and shape of the peak are mainly determined by the standard deviation σ . The physical model is validated by fitting the frequency curve for a single particle at two different strengths of the applied field, using the same set of parameters for the magnetic particle (Fig. 5.15). Since the fit does not yield a unique set of parameters, this technique can not be used for determining the magnetic properties of the particles in detail. Nevertheless the model reveals the mechanism behind the generation of a torque on the particle at high field frequencies.

It is interesting to note that a qualitative analogue exists of the phenomena observed here. A nanowire placed in a high-frequency rotating electric field rotates at a frequency much lower than the applied field frequency.^[14] In this case the torque has an electric origin, generated by the interaction between an applied electric field and a field-induced electric dipole moment.

Our model correctly accounts for the observed decrease of the particle rotation frequency beyond 400 kHz. We understand this as follows. At each field frequency, a different part of the nanoparticle size distribution contributes to the torque. Nanoparticles having a short relaxation time ($\tau \ll 2\pi/\omega_f$) follow the field instantaneously, giving the real part of the magnetization. Nanoparticles with a relaxation time comparable to $2\pi/\omega_f$ follow the field with a certain phase lag, causing the imaginary part of the magnetization. Finally, large nanoparticles with a long relaxation time ($\tau \gg 2\pi/\omega_f$) do not follow the rotating magnetic field. The observed maximum response is caused by the fact that at frequencies above one MHz, even the smallest nanoparticles can not follow the high field frequency and the rotation frequency of the particle goes to zero.

5.3.3 Chemically coupled two-particle cluster

Although the M-280 particles are spherically shaped, it can not be ruled out that the particles have a magnetic anisotropy for example due to an inhomogeneous spatial distribution of the nanoparticles inside the particle. Such a magnetic anisotropy causes the induced magnetization to have a preferential orientation with respect to the particle. When this preferential orientation is not aligned with the applied field, the angle between the field and the induced magnetization results in a torque on the particle. Therefore it is interesting to study the influence of a magnetic anisotropy on the rotational behavior of the particle. The goal is to study if the torque due to shape anisotropy can be discriminated from the torque due to the permanent magnetic moment and the torque due to the finite relaxation time of the nanoparticles.

To study the influence of shape anisotropy of the particle, measurements have been performed on $1 \mu\text{m}$ streptavidin coated Dynal My-One particles that are biochemically coupled by Biotinylated Bovine Serum Albumin. Each BSA molecule has four to eight Biotin molecules attached to it, which can bind to the streptavidin on the particles and by that allow the formation of clusters. In the experiments described in this section, clusters of two particles are used.

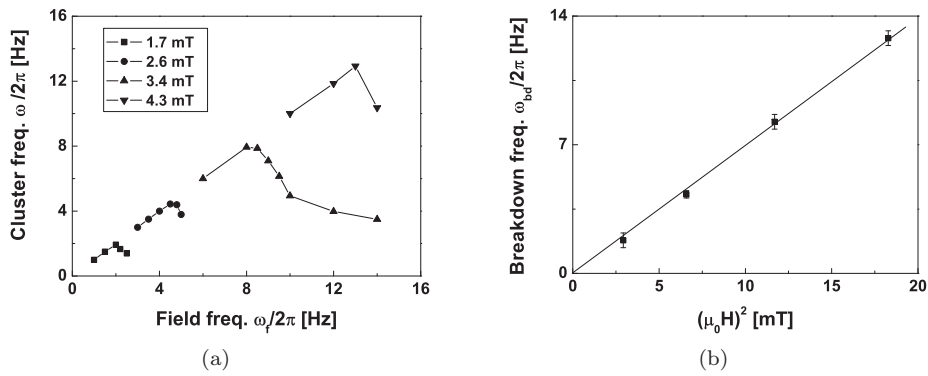


Fig. 5.16: (a) Average rotation frequency of the two-particle cluster versus the field frequency for different field strength. (b) Breakdown frequency versus the square of the field strength.

Clusters in which two particles are formed by interaction of the magnetic moments of the two individual particles have been qualitatively studied by Garcia *et al.*,^[15] where the main focus was to address oscillations of the inter-particle distance above the breakdown frequency. In our experiments the distance between the particles is fixed due to the biological bond, which allows us to treat the two-particle cluster as a single solid magnetizable body with a shape anisotropy.

For low field frequencies (Fig. 5.16a) the average rotation frequency of the two-particle cluster increases linearly up to a breakdown frequency, similar as for the single $2.8 \mu\text{m}$ particles. However, the measured breakdown frequency increases quadratically with the applied field strength (Fig. 5.16b) which indicates that the rotation at low field frequencies is caused by an induced magnetic moment. Above the breakdown frequency the two-particle cluster starts to wiggle with a frequency [$\omega_{wiggle} = 2(\omega_f - \omega_p)$] that is twice that of a single particle with a fixed magnetic moment.

The shape anisotropy of the two-particle cluster causes the magnetization to have a preferable orientation along the long axis of the two-particle cluster. When the two-particle cluster is placed in a magnetic field, it orientates itself with the long axis along the field lines. Note that because of symmetry, the two-particle cluster can align in two directions (180 degrees opposite of each other). Below the breakdown frequency the two-particle cluster is able to follow the field, but above

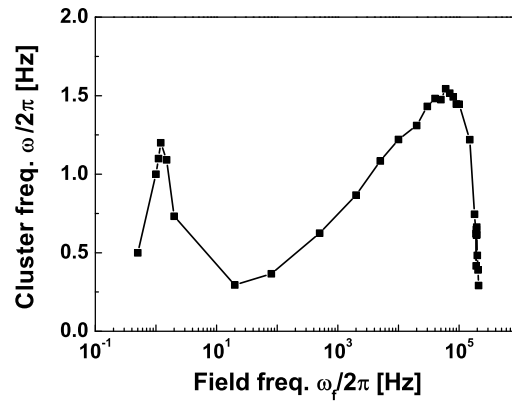


Fig. 5.17: Average rotation frequency of the two-particle cluster versus the field frequency. The line is plotted as a guide to the eye.

the breakdown frequency the two-particle cluster starts lagging behind and the angle between the long axis and the field increases. Once this angle is larger than 90 degrees, the magnetization of the two-particle cluster flips along the easy axis and a period of backward rotation is observed where the angle between the field and the long axis decreases until it reaches zero. Then the two-particle cluster follows the field again, until the angle is again larger than 90 degrees and the magnetization flips again. Note that the flipping of the induced magnetic moment along the easy axis causes the factor two in the wiggle frequency [$\omega_{wiggle} = 2(\omega_f - \omega_p)$]. It is concluded that, although the 1 μm particles have a small permanent magnetic moment,^[16] the rotation of the two-particle cluster at low field frequencies is dominated by the induced magnetization that preferably aligns along the long axis of the two-particle cluster. For high field frequencies (>50 Hz) the rotation of the two-particle cluster is dominated by torque due to the complex susceptibility like in the case of the single particles (Fig. 5.17). A detailed model describing this behavior quantitatively is presented in the paper of Ranzoni *et al.*^[16]

Finally it is useful to list the three indications that the low-frequency rotation of the Dynal M-280 particles is caused by a permanent magnetic moment with a fixed orientation and not by a magnetic anisotropy. First, the measured breakdown frequency of the M-280 particles increases linearly rather than quadratically with the applied field. Second, we observed in the microscope that every particle orientates itself in one unique direction with respect to an applied field rather than two directions. Finally we observed for field frequencies above the breakdown frequency that the rotation is periodically interrupted by short phases of backward rotation that appear at a frequency $\omega = \omega_f - \omega_p$ rather than at $2(\omega_f - \omega_p)$.

5.4 Conclusion

In summary, we have demonstrated rotation of Dynal M-280 particles due to a rotating magnetic field over a wide range of applied field frequencies. At low field frequencies, the torque is determined by a small permanent magnetic moment in the particle. We have developed a method to determine the permanent magnetic moment from the rotational behavior of the particle when applying a rotating magnetic field. The permanent moment of the M-280 particles is found to vary between $(2 \pm 0.2) \cdot 10^{-16} \text{ Am}^2$ and $(2.5 \pm 0.2) \cdot 10^{-15} \text{ Am}^2$. Since the orientation of the permanent magnetic moment is fixed with respect to the particle, the applied torque is dependent on the physical orientation of the particle with respect to the applied field.

At high field frequencies, the phase lag between the field and the induced magnetization gives rise to a torque on the particle. The torque can be understood from the non-zero relaxation time of the ironoxide nanoparticles in the particle and can be quantitatively described with a frequency dependent complex susceptibility. The torque related to the complex susceptibility is independent on the physical orientation of the field and fully determined by the orientation of the induced magnetization with respect to the applied field.

In conclusion, we have described novel ways to quantitatively determine the magnetic torque of single magnetic particles in a rotating magnetic field. The insight into torque generation mechanisms will be applied in biological experiments, as described in the following chapters.

References

- [1] U. Bockelmann. Single-molecule manipulation of nucleic acids. *Current Opinion in Structural Biology*, 14:368–373, 2004.
- [2] K. Besteman, S. Hage, N.H. Dekker, and S.G. Lemay. Role of Tension and Twist in Single-Molecule DNA Condensation. *Physical Review Letters*, 98(5):058103, 2007.
- [3] D.A. Koster, K. Palle, E.S.M. Bot, M.A. Bjornsti, and N.H. Dekker. Antitumour drugs impede DNA uncoiling by topoisomerase I. *Nature*, 448:213–217, 2007.
- [4] K. van Ommering, J.H. Nieuwenhuis, L.J. van IJzendoorn, B. Koopmans, and M.W.J. Prins. Confined brownian motion of individual magnetic nanoparticles on a chip: Characterization of magnetic susceptibility. *Applied Physics Letters*, 89:142511, 2006.
- [5] X.J.A. Janssen, L.J. van IJzendoorn, and M.W.J. Prins. On-chip manipulation and detection of magnetic particles for functional biosensors. *Biosensors and Bioelectronics*, 23:833–838, 2008.

-
- [6] G. Fønnum, C. Johansson, A. Molteberg, S. Mørup, and E. Aksnes. Characterisation of Dynabeads by magnetization measurements and Mössbauer spectroscopy. *Journal of Magnetism and Magnetic Materials*, 293:41–47, 2005.
- [7] G.V. Kurl'yanskaya, M.L. Sánchez, B. Hernando, V.M. Prida, P. Gorria, and M. Tejedor. Giant-magnetoimpedance-based sensitive element as a model for biosensors. *Applied Physics Letters*, 82:3053–3055, 2003.
- [8] C.J. Goss. Saturation magnetisation, coercivity and lattice parameter changes in the system $\text{Fe}_3\text{O}_4\text{-}\gamma\text{-Fe}_2\text{O}_3$, and their relationship to structure. *Physics and Chemistry of Minerals*, 16:164–171, 1988.
- [9] F. Bødker, S. Mørup, and S. Linderøth. Surface effects in metallic iron nanoparticles. *Physical Review Letters*, 72(2):282–285, 1994.
- [10] E. du Trémolet de Lacheisserie, D. Gignoux, and M. Schlenker. *Magnetism: Materials and Applications*. Springer, 1 edition, 2004.
- [11] P.C. Fannin, L. Cohen-Tannoudji, E. Bertrand, A.T. Giannitsis, C. Mac Oireachtaigh, and J. Bibette. Investigation of the complex susceptibility of magnetic beads containing maghemite nanoparticles. *Journal of Magnetism and Magnetic Materials*, 303:147–152, 2006.
- [12] C. Johansson, M. hansson, M.S. Pedersen, and S. Mørup. Magnetic properties of magnetic liquids with iron-oxide particles - the influence of anisotropy and interactions. *Journal of Magnetism and Magnetic Materials*, 173:5–14, 1997.
- [13] R.E. Rosensweig. *Ferrohydrodynamics*. Cambridge University Press, 1985.
- [14] D.L. Fan, F.Q. Zhu, R.C. Cammarata, and C.L. Chien. Controllable high-speed rotation of nanowires. *Physical Review Letters*, 94(24):247208, 2005.
- [15] P. Domínguez-García, Sonia Melle, O. G. Calderón, and M.A. Rubio. Doublet dynamics of magnetizable particles under frequency modulated rotating fields. *Colloids and Surfaces A: Physicochemical and Engineering Aspects*, 270271:270–276, 2005.
- [16] A. Ranzoni, X.J.A. Janssen, M. Ovsyanko, L.J. van IJzendoorn, and M.W.J. Prins. Magnetically controlled rotation and torque of uniaxial microactuators for lab-on-a-chip applications. *accepted for publication in Lab on a Chip*, 2009.

Chapter 6

Non-specific binding of particles studied by rotating magnetic fields

We describe a new technique to study the interaction between protein-coated particles and a surface. The technique is based on the rotation of magnetic particles by uniform rotating magnetic fields. The non-specific binding between streptavidin coated Dynal M-280 particles and a glass substrate is measured for various buffer conditions. Binding increases for increasing ionic strength and decreasing pH, which we attribute to shielding of electrostatic repulsion between the particles and the surface. The results of this new technique are compared and found to be in good agreement with results of magnetic tweezers experiments and with calculations of the electrostatic interaction between a sphere and a wall. Furthermore we used a model system in which binding is reduced by blocking the substrate with bovine serum albumin (BSA) to show the feasibility of the technique to measure the effect of surface coating.

A condensed version of this chapter is in preparation for publication: X.J.A. Janssen, A. van Reenen, L.J. van IJzendoorn, A.M. de Jong and M.W.J. prins *The rotating particles probe: a new technique to measure interactions between protein-coated particles and a substrate*

6.1 Introduction

In this chapter we describe a new technique to measure interactions between protein-coated particles and a surface. The technique is based on the measurement of field-induced rotation of magnetic particles in contact with a surface as discussed in the previous chapter. The discrimination between the bound and unbound state is made by monitoring the rotation of the particles. The rotation technique has an advantage over the pulling experiments presented in chapter 4, that the unbound particles stay on the surface. Therefore the full association and dissociation behavior can be measured continuously in time in a single measurement using a single sample. Furthermore the parallel measurement of many particles with single-particle resolution gives reliable statistics in a short time.

We show the feasibility of this novel technique by measuring the non-specific interaction between streptavidin coated particles and a glass surface under varying conditions like ionic strength, pH and BSA coating of the substrate. The results are compared with a model that describes the electrostatic interaction between the substrate and the particles.

6.2 Experimental

6.2.1 Quadrupole setup

Design and simulations

In the single particle experiments presented in chapter 5, the local horizontal and vertical field gradients confined the particle at the intersection of the two wires. When applying a magnetic field over a large area (much larger than the size of the particles) in order to study multiple particles in parallel, it is desirable that the applied field is homogeneous, such that over the area in which the particles are studied, all the particles experience the same field. Furthermore it is important to minimize field gradients because these induce translational forces on the particles and consequently to the biological molecules. The forces can complicate the interpretation of torsional magnetic tweezers experiments.

A quadrupole setup was developed to apply a homogeneous rotating magnetic field over a large area (typically 1 x 1 mm). The setup consists of four soft iron^[1] pole tips connected by a soft iron yoke (Fig. 6.1a). The pole tips are slanted to guide the field towards the sample that is placed on top of the tips (Fig. 6.1b). The magnetic field, when seen from above, can be applied in two orthogonal directions by actuation of two opposite coils (Fig. 6.1c and f). By varying the currents through all four coils, the field can be orientated in every direction in the plane of the sample (Fig. 6.1c-f).

The shape of the pole tips is designed using Comsol Multiphysics simulations where we aimed on minimizing the horizontal and vertical field gradients. Figures 6.2a and b show the magnetic field strength between two poles, calculated along a

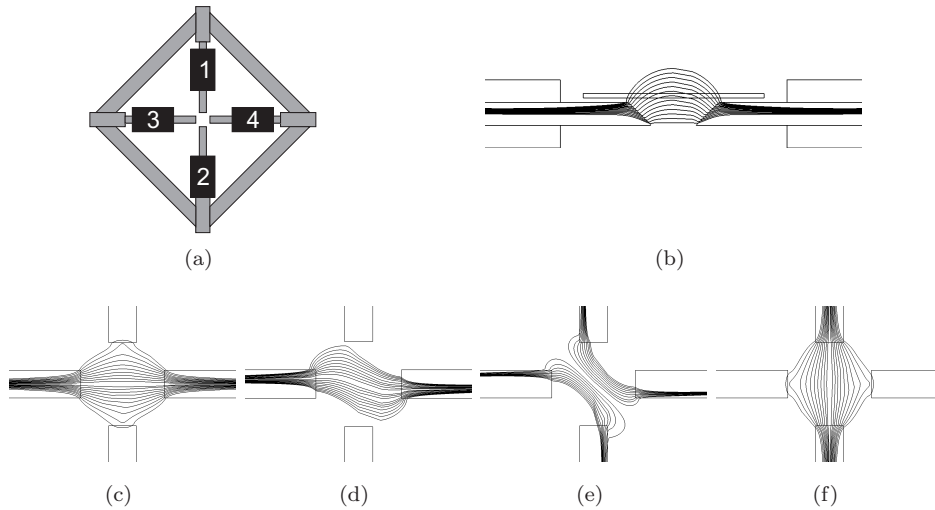


Fig. 6.1: (a) Top view of the magnetic rotation setup which consists of four individual controlled coils (black) with soft-iron poles connected by a soft-iron yoke. (b) Cross section of the rotation setup showing the slanted pole tips and the field-lines simulated by Comsol Multiphysics. The position of the sample on top of the pole tips is indicated by the rectangle. (c-f) Top view of the magnetic field lines orientated under 0, 22.5, 45 and 90 degrees by balancing the currents through the coils.

horizontal and vertical cross-section. The field gradient is calculated by numerical differentiation of the field strength with respect to the position (Fig. 6.2c and d). Three different angles of the pole tips ($\theta = 30, 45$ and 60 degrees) are simulated while the distance between the tips is kept constant at 10 mm.

The total field strength at the center of the sample (Fig. 6.2a and b) increases with increasing angle θ because the upper corners of the tips approach the sample. The vertical gradient of the total field (Fig. 6.2c) also increases with increasing angle θ since it is proportional to the field strength and is typically -4 T/m at the center of the sample. Due to this small gradient the particles are pulled downwards and are only in mild contact with the surface compared to the experiment using the on-chip current wires (with vertical gradients of typically $2 \cdot 10^3$ T/m). The horizontal gradient of the total field (Fig. 6.2c) decreases with decreasing distance to the center of the setup and is exactly zero at the center due to symmetry. For a pole tip angle around 45 degrees (Fig. 6.2c) the gradient is almost constant and zero over several millimeters.

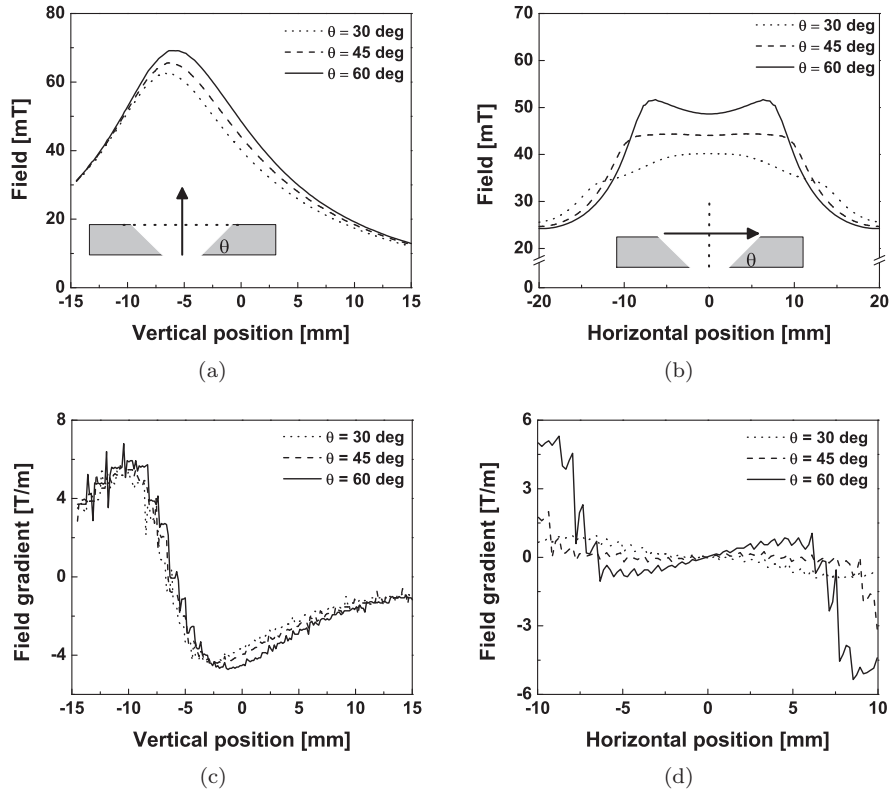


Fig. 6.2: (a) Total magnetic field strength as function of the vertical distance to the top of the pole tips. (b) Total magnetic field strength as function of the horizontal distance to the center of the setup. The arrows in the sketches of the pole tips indicate the position and the direction of the line scan and the dotted line in the sketches represents the origin of the line scan. (c) Vertical gradient of the total field as function of the vertical distance to the top of the pole tips. (d) Horizontal gradient of the total field as function of the horizontal distance to the center of the setup.

Although these simulations do not represent a full optimization procedure, the setup was manufactured with pole tips slanted under 45 degrees. The distance between the pole tips can be varied to optimize the setup after manufacturing, depending on the desired conditions (field strength versus gradient).

Characterization

Two opposite coils are connected in series and the field strength was measured using a Hall-sensor (F.W. Bell STH57-0404). The probe was attached to a micro-manipulator (Leica) which allows a positioning with an accuracy of $10 \mu\text{m}$. The hysteresis loop is measured quasi-statically with the probe positioned at the cen-

ter of the sample (Fig. 6.3a). The proportionality constant between the applied current and the measured field is 37 mT/A and no saturation of the soft-iron is observed up to 400 mA. The effect of hysteresis on a time dependent magnetic field is visualized by applying a sinusoidal current with a frequency of 0.2 Hz and measuring the generated field using a GMR sensor (Fig. 6.3b). The generated field has a small non-constant phase lag with respect to the applied current *i.e.* the phase lag is zero at the extremes of the applied current since maximum field is obtained at maximum current. When a rotating magnetic field is created this phase lag is present in both orthogonal directions (between coils 1-2 and coils 3-4). When a magnetic field with constant magnitude that rotates with a constant angular velocity is represented by a circle, the phase lag causes this circle to become slightly elliptically with the long axis under 45 degrees with respect to the pole tips. Because this deviation is typically a few percent it is neglected in further calculations/measurements.

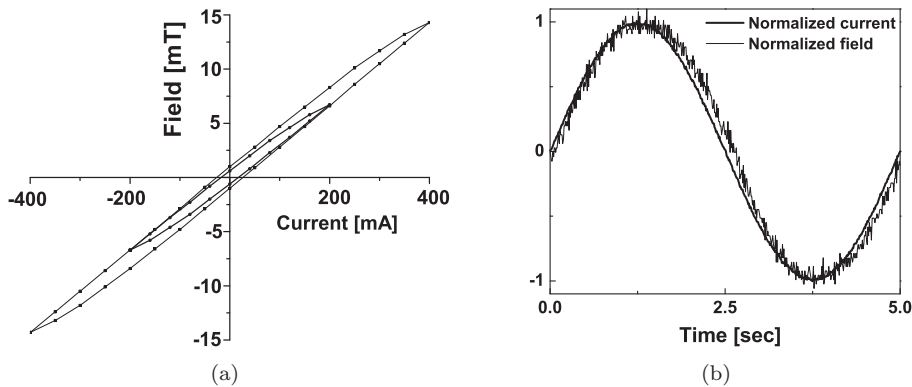


Fig. 6.3: (a) Quasistatic measurements of the hysteresis loop of the setup for two amplitudes of the sinusoidal currents (200 and 400 mA_{pp}). (b) Dynamic measurement of the applied current and generated magnetic field showing the effect of hysteresis (both normalized).

The field strength is also measured as a function of the height above the pole tips (Fig. 6.4a) and the distance to the center of the setup (Fig. 6.4b) with a step size of 0.1 mm. The field gradient is calculated by numerical differentiation of the data. For a current of 277 mA, the field strength at the center of the sample is 11 mT with a vertical gradient of -1 T/m. Since the gradient scales with the applied field, these values are comparable to those found in the simulation (-4 T/m at 45 mT). To illustrate: a field of 10 mT with a gradient of 1 T/m exerts a force of $6 \cdot 10^{-14}$ N on a 2.8 μm Dynal particle which is comparable to the gravitational force ($5 \cdot 10^{-14}$ N) on the particle when it is suspended in water. The gradient in horizontal direction is smaller than 0.25 T/m up to a distance of 5 mm from the center of the setup which gives a force on the particles of the order of $1 \cdot 10^{-14}$ N.

According to Stoke's law, a $2.8 \mu\text{m}$ particle experiencing a force of $1 \cdot 10^{-14}$ N force will travel at a speed of $0.4 \mu\text{m/s}$ in bulk fluid. During the experiments described in the remaining part of this chapter, no movement of unbound particles on the substrate is observed. We attribute this to the fact that the effective viscosity increases close to the surface and furthermore, the particles are in mild contact with the surface due to the small vertical force.

Since the two coils are connected in series, the current through both coils is identical and the asymmetry in the field strength (with respect to the horizontal position) is caused by coil-to-coil variations in the windings. During further experiments the current through each coil is controlled individually by four voltage-controlled push-pull current sources (Chapter 4) to correct for coil-to-coil variations.

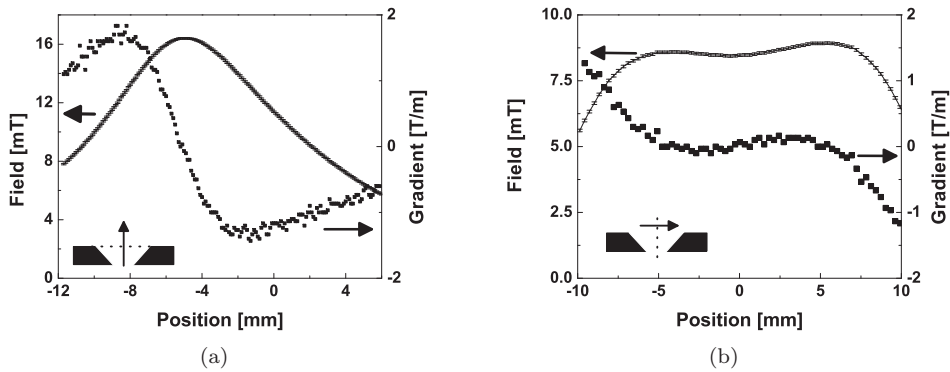


Fig. 6.4: (a) Measurement of the magnetic field strength as function of the vertical distance to the center of the setup. (b) Measurement of the magnetic field strength as function of the horizontal distance to the center of the setup. The arrows in the sketches of the pole tips indicate the position and the direction of the line scan and the dotted line in the sketches represents the origin of the line scan.

6.2.2 Sample preparation and methods

Standard microscope slides (76 mm x 26 mm x 1 mm) of Menzel-Gläser are cleaned with iso-propanol and a Secure-Seal spacer is placed on top of the glass to create a well with a diameter of 9 mm and a depth of 0.12 mm (Fig. 6.5a). The cell is filled with a known amount of diluted particle solution (Fig. 6.5b) and placed under the water-immersion objective of the microscope (Fig. 6.5c). After sedimentation of the particles for 5 minutes, a known amount of de-ionized water is added to make contact between the objective and the sample (Fig. 6.5d). Finally, the rotating magnetic field is switched on and the condition of the fluid *i.e.* ionic strength, pH is changed by adding a known amount of buffer solution (Fig. 6.5e). The sample is imaged with a total magnification of $1260 \times$ (Leica DM6000M) and movies are

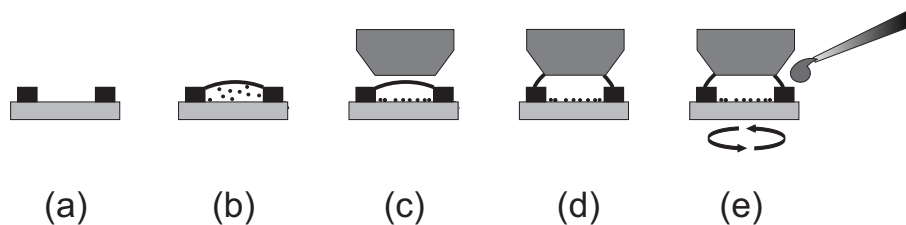


Fig. 6.5: Sample preparation starts with making a cell (a) on top of a glass substrate which is filled with particles suspended in fluid (b). After sedimentation (c) the cell is placed under an immersion objective and de-ionized water is added to make contact with the the objective (d). Finally the rotating magnetic field is switched on and the condition of the fluid (i.a. ionic strength or pH) is changed by adding buffer fluid (e).

recorded during the experiment using a high speed camera (Redlake MotionPro HS-3). The movies are analyzed after the experiment and the number of rotating particles is determined as function of time. Particles that do not follow the rotating field are regarded as bound to the surface of the substrate.

6.3 Results and discussion

6.3.1 Influence of ionic strength

It is observed that before changing the buffer conditions, more than 95% of the particles follow the rotating field over a period up to several hours, and therefore it is concluded that particles suspended in de-ionized water do not bind to the glass substrate. After increasing the ionic strength by adding phosphate buffered saline (PBS) buffer (at $t = 0$ sec), the fraction of rotating particles decreases in time until a steady state is reached (Fig. 6.6a). Apparently, some kind of interaction between the particles and the substrate prohibits free rotation. We regard this binding as non-specific since no biological ligand/receptor system is present. After diluting the buffer with de-ionized water at $t = 500$ seconds and $t = 750$ seconds, the fraction of free particles increases again, showing that the binding is a reversible process.

The addition of the fluid to change the buffer condition causes mixing of the sample, but it can not be assumed that the sample is homogenously mixed at the start of the experiment. The rate of binding is therefore a combination of binding kinetics and homogenization of the fluid by diffusion and convection. Using a premixed suspension of particles and buffer assures a homogeneous mixture at the start of the experiment, but the measured binding rate is then influenced by the variations in residence time of the particles at the surface. The sedimentation speed of the particles is typically $2 \mu\text{m/s}$ whereas the droplet height between the

objective and the substrate is 2 mm. Particles that are initially in the upper part of the fluid reach the surface minutes later than those that were already close to the surface. Particles that are on the surface for a longer period of time have a higher chance of being in the bound state since no unbinding is observed and therefore we have chosen not to use a premixed solution.

The dependency of binding on the ionic strength is studied by varying the ionic strength using different concentrations of added PBS buffer (Fig. 6.6b). The

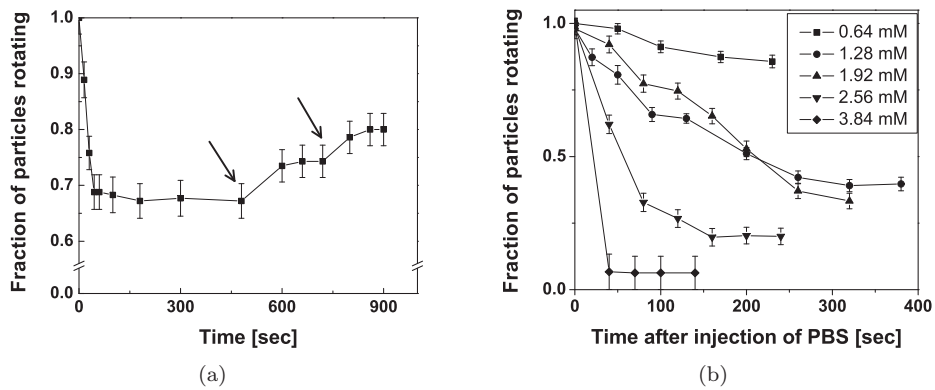


Fig. 6.6: (a) The fraction of free particles versus time after increasing the ionic strength by adding PBS at $t = 0$ and decreasing by adding de-ionized water after 500 and 750 seconds (indicated by the arrows) (b) The fraction of free particles versus time for different ionic strengths of the PBS buffer.

steady state fraction is found to be dependent on the ionic strength of the solution. Figure 6.7a shows the steady state fraction of bound particles versus the ionic strength of the solution. The results of the rotation experiments show a similar sigmoidal dependency of the binding on the ionic strength between 1 mM and 10 mM as in the experiments using magnetic force discrimination (Chapter 4). The ionic strength at which 50% of the particles bind to the surface is slightly higher in the pulling experiments (2 mM versus 6 mM).

It is difficult to compare the outcome of both types of experiments directly because of the different physical nature between a translational force and an applied torque. With a typical magnetic moment of $1 \cdot 10^{-15} \text{ Am}^2$ (chapter 5), the magnetic torque exerted on the particles is $4 \cdot 10^{-18} \text{ Nm}$. The exact size of the region over which the interaction between the particle and the surface takes place is not known. If we assume a lever between 5 nm (size of a protein) and 100 nm (typical distance between two protruding parts of the particle), we find a corresponding force of respectively 750 pN and 40 pN. Note that the force applied in the pulling experiments was 80 pN.

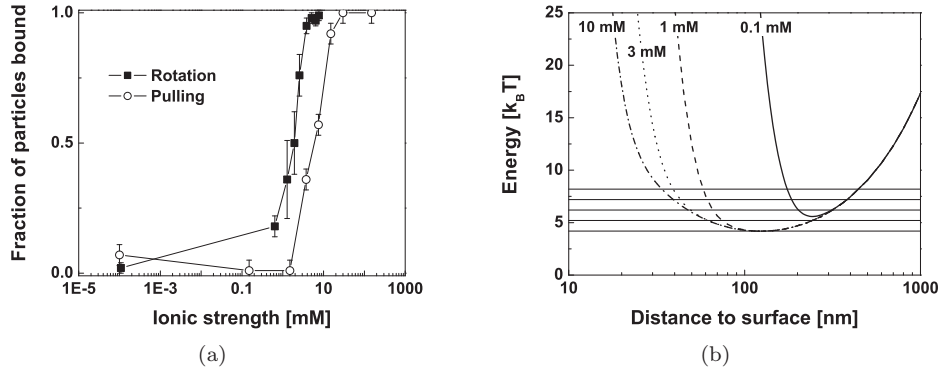


Fig. 6.7: (a) Fraction of free particles versus the ionic strength of the fluid for rotational actuation of the particles and for magnetic force discrimination (Chapter 4). (b) The sum of the gravitational, magnetic, van der Waals (Hamaker constant $0.45 \cdot 10^{-20}$ J) and electrostatic energy of a sphere with a zeta-potential of -20 mV above a surface with a zeta-potential of -30 mV versus the distance between the sphere and the surface for varying ionic strength of the fluid. The horizontal lines are spaced $k_B T$ apart to give an indication of the freedom of movement of the sphere due to thermal energy.

As explained in chapter 4, the strong dependency of binding on the ionic strength leads us to the hypothesis that for low ionic strength electrostatic repulsion keeps the particles at a finite distance from the substrate. For increasing ionic strength the surface potentials are increasingly shielded causing the equilibrium height of the particles to decrease. When the protruding parts of the particles are able to touch the substrate, the particles can bind non-specifically to the substrate as a result of the short range van der Waals interactions between the streptavidin and the glass.^[2]

The classic DLVO model (chapter 2) gives a qualitative insight into the forces playing a role in the dependency of the non-specific binding on the ionic strength of the solution. Figure 6.7b shows the total energy as function of the distance between a sphere and the surface. The calculation is identical to that shown in chapter 4 but now also the magnetic force that is pulling the particles towards the surface is taken into account.

6.3.2 Influence of pH

In order to further investigate the assumption that the electrostatic interaction is a dominant factor in our experiments, we studied particle binding under different pH conditions (Fig. 6.8a). The used buffers, 2-(*N*-morpholino)ethanesulfonic acid (MES) with pH 4.7, Phosphate buffered saline (PBS) with pH 7.4 and carbonate with pH 9.6 are diluted with de-ionized water to change the ionic strength of the

solution. Due to the dilution, the pH effectively changes with the changing ionic strength since the buffers can not maintain the pH for low ionic strength (< 0.01 mM). For increasing ionic strength, the pH of the diluted buffer comes closer to that of the undiluted buffer. For increasing ionic strengths (10^{-4} mM to 150 mM), the pH of the MES, PBS and carbonate buffer changes respectively from 7.4 to 4.7, 7.0 to 7.4 and 9.0 to 9.6

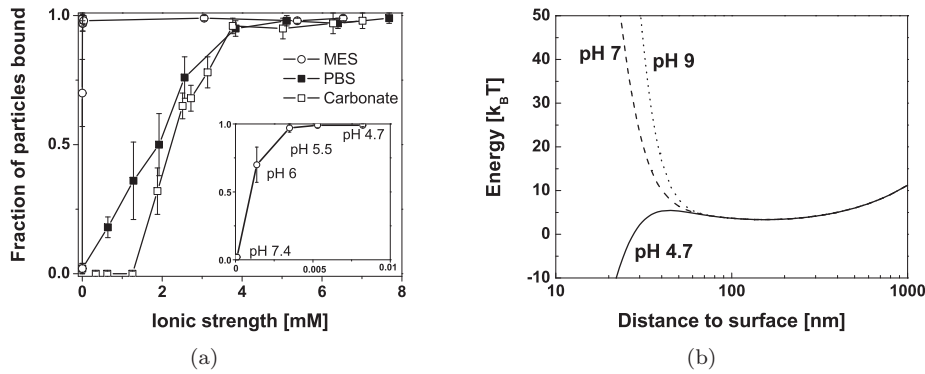


Fig. 6.8: (a) Dependency of the non-specific binding of particles on the ionic strength and pH of the buffer. Inset: Fraction of particles rotating on the substrate for low ionic strength of the MES-Buffer. Note that the MES-buffer can not hold pH 4.7 for low ionic strength. The lines are guides to the eye. (b) The total energy of a sphere close to a flat surface calculated by summation of the van der Waals (Hamaker constant typically -1 kT), magnetic, gravitational and electrostatic interaction for different pH.

For a low pH (MES buffer), all the particles bind to the substrate and only for very low ionic strength (< 5 μ M) some particles are not bound (inset of Fig 6.8a). Diluting the MES buffer below 0.01 mM causes the pH to rise above the iso-electric point (pI) of the particles and as a result the surface charge of the particles changes from positive to negative making the electrostatic interaction repulsive. For the PBS and carbonate buffer, the ionic strength at which 50% of the particles bind to the substrate, is respectively 1.8 mM and 2.5 mM (Fig. 6.8a). For pH 9, a threshold in the ionic strength (1.2 mM) is observed below which the particles do not bind.

Table 6.1: The zeta potential of the Dynal M-280 particles^[3] and a typical glass surface^[4, 5] for various pH values of the fluid.

	pH 4.7	pH 7.0	pH 9.0
ζ particle [mV]	20	-20	-35
ζ glass [mV]	-10	-29	-40

Changing the pH effectively results in changing the zeta potential of both the substrate and the particle (Table 6.1). We calculated the total energy (van der Waals, electrostatic, magnetic and gravitational energy) as function of the distance between the sphere and the surface (Fig. 6.8b) for different values of the zeta potential. For a pH below the pI of the particles (pH 5), the particles are positively charged while the glass is still negatively charged. Electrostatic attraction brings the particles close to the substrate and allows binding. For increasing pH (7.5 and 9.0) the electrostatic interaction becomes repulsive and a higher ionic strength is needed to effectively shield the electrostatic repulsion before the particles can come into contact with the surface and allow binding.

6.3.3 Surface blocking with bovine serum albumin

In immunoassays non-specific binding of molecules/labels negatively affects the detection limit, the sensitivity as well as the specificity of the assay.^[6] In sensors based on magnetic particles different strategies are explored (mainly by empirical testing) to reduce non-specific binding by e.g. magnetic forces, dielectrophoretic repulsion or fluidic shear forces.^[7–10] Another well known technique to reduce non-specific binding is surface coating with e.g. self-assembled monolayers^[11–13] or proteins like Bovine Serum Albumine (BSA).^[14,15]

To study the feasibility of the rotating particles technique to measure the blocking effect, we used a model system in which the binding is reduced by coating the glass surface with BSA. The time to equilibrium and the amount of BSA absorbed onto the substrate are dependent on the pH of the BSA solution and the pI of BSA and the pI of the substrate.^[15,16] For a pH in between both pI's, the BSA and the substrate have opposite surface charge which gives rise to an electrostatic attraction between the BSA and the surface which favors binding. For equally signed charge, BSA still binds to the surface but the electrostatic repulsion reduces the binding rate. Incubation times for BSA are reported to range from less than an hour^[8,9] up to one day^[15,16] depending on the conditions, substrates and type of assay.

To ensure equilibrium, we incubated the glass substrate for 18 hours at 4 degrees Celsius with different concentrations of BSA dissolved in PBS buffer (pH 7.4). After incubation, the sample is rinsed with de-ionized water. After drying the samples with nitrogen gas, the well is used as described before to determine binding for different ionic strength of the buffer at three different BSA concentrations and for different BSA concentrations at a fixed ionic strength of 2.8 mM.

Binding is strongly reduced when increasing the BSA concentration (Fig. 6.9a). A threshold in the ionic strength is observed below which no binding occurs, which increases from 1.2 mM for 10^{-2} g/L BSA to above 6 mM for 10^{-1} g/L BSA. Measured at a fixed ionic strength, the fraction of bound particles shows a sigmoidal curve with respect to the BSA concentration (Fig. 6.9b). Experiments on blocking in Enzyme-Linked Immunosorbent Assays (ELISA)^[6] using various blocking

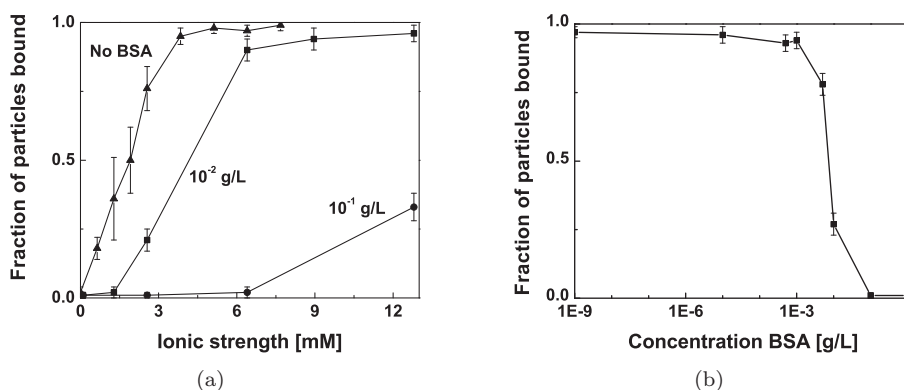


Fig. 6.9: (a) Dependency of binding on the ionic strength after blocking the surface of the substrate with different concentrations of BSA (no BSA, 10^{-2} g/L and 10^{-1} g/L). (b) Dependency of binding on the concentration of BSA for an ionic strength of 2.8 mM PBS. The lines are guides to the eye.

agents (including BSA) show similar sigmoidal curves. Independent of the type of blocking agent, the transition between 0% blocking and 100% blocking spreads over two orders of magnitude in the concentration of the blocking agent. Why this transition spreads over two orders of magnitude in the concentration is not known. The rapid increase of blocking activity above a certain concentration of the blocking agent is caused by exceeding the minimum concentration for saturating the surface of the substrate for the used incubation conditions.^[6]

The pI and the zeta potential of BSA at pH 7 have been reported to be 5.1 and -18 mV^[15,17] whereas the zeta potential of the glass is about -20 mV for the ionic strengths used in these experiments.^[5] Adding a layer of BSA on the surface of the glass is therefore not likely to change the zeta potential of the glass. The blocking up to an ionic strength of 13 mM (Fig. 6.9a) can therefore not be understood from the electrostatic repulsion between the particle and the surface. Furthermore for a streptavidin-water-glass system the van der Waals force is repulsive (positive Hamaker constant) whereas for a streptavidin-water-BSA system the van der Waals force is attractive (negative Hamaker constant).

Since the electrostatic and van der Waals interactions between the mesoscopic objects (particle and surface) cannot cause the observed blocking effect, we hypothesize that interactions on the molecular scale prevent the streptavidin from binding to the glass. Vogt *et al.*^[6] hypothesized that the absorption of a monolayer of proteins on a substrate prevents further binding of other proteins by protein-surface interactions. This theory is supported by the findings of Docoslis *et al.*^[18] who attribute the blocking effect of serum albumin to steric hindrance. Furthermore it is stated that once a protein is absorbed onto a surface, it not only prevents absorption of another protein at that exact spot but also in its vicinity.^[18]

Although the blocking effect is not fully understood, our measurements clearly show that the effect of BSA blocking can be measured using the particle rotation probe technique. This paves the way for binding/unbinding experiments on biological ligand/receptor systems (i.e. studying specific interactions) in magnetic particle based assays to determine dissociation kinetics and optimizing buffer conditions that can be ultimately applied in a functional biosensor.

6.4 Conclusion

In summary, we have developed a technique to measure binding between magnetic particles and a substrate, based on monitoring the rotation of particles actuated by a uniform rotating magnetic field. Using this technique, we showed that the non-specific binding between streptavidin coated Dynal M-280 particles and a glass substrate is highly dependent on the pH and the ionic strength of the buffer solution. Calculations on the electrostatic interaction show that the increase of the non-specific binding with increasing ionic strength is caused by shielding of the electrostatic repulsion between the particles and the surface. When coating the glass substrate with bovine serum albumin (BSA), the non-specific binding of streptavidin coated particles is strongly reduced. Although the blocking effect of BSA is not fully understood, our measurements clearly show the feasibility of rotational excitation of particles to probe molecular interactions. The main advantage of rotational actuation over pulling is the fact that unbound particles are not lost during the experiment which allows to study binding as well as unbinding kinetics. In conclusion, our technique represents a novel way to measure (non-specific) binding and/or unbinding of magnetic labels in a biological assay.

References

- [1] Armco-Pure-Iron. Ak steel. www.aksteel.com.
- [2] M.L. Korwin-Edson, A.G. Clare, M.M. Hall, and A. Goldstein. Biospecificity of glass surfaces: streptavidin attachment to silica. *Journal of Non-Crystalline Solids*, 349:260–266, 2004.
- [3] *Invitrogen E-mail inquiry*.
- [4] S.H. Behrens and D.G. Grier. The charge of glass and silica surfaces. *Journal of Chemical Physics*, 115(14):6716–6721, 2001.
- [5] Y. Gu and D. Li. The ζ -potential of glass surface in contact with aqueous solutions. *Journal of Colloid and Interface Science*, 226:328–339, 2000.
- [6] R.F. Vogt, D.L. Phillips, L. Omar Henderson, W. Withfield, and F.W. Spierto. Quantitative differences among various proteins as blocking agents

- for ELISA microtiterplates. *Journal of Immunological Methods*, 101:43–50, 1987.
- [7] V.N. Morozov and T.Y. Morozova. Active bead-linked immunoassay on protein microarrays. *Analytica Chimica Acta*, 564:40–52, 2006.
- [8] M. Koets, T. van der Wijk, J.T.W.M. van Eemeren, A. van Amerongen, and M.W.J. Prins. Rapid DNA multi-analyte immunoassay on a magneto-resistance biosensor. *Biosensors and Bioelectronics*, 24(7):1893–1898, 2008.
- [9] W.U. Dittmer, P. de Kievit, M.W.J. Prins, J.L.M. Vissers, M.E.C. Mersch, and M.F.W.C. Martens. Sensitive and rapid immunoassay for parathyroid hormone using magnetic particle labels and magnetic actuation. *Journal of Immunological Methods*, 338:40–46, 2008.
- [10] C. Liu, R. De Palma, G. Reekmans, W. Laureyn, T. Stakenborg, and L. Lagae. Discrimination of specific and non-specific bindings by dielectrophoretic repulsion in on-chip magnetic bio-assays. *Biosensors and Bioelectronics*, 24(7):2294–2297, 2009.
- [11] P. Harder, M. Grunze, R. Dahint, G.M. Whitesides, and P.E. Laibinis. Molecular Conformation in Oligo(ethylene glycol)-Terminated Self-Assembled Monolayers on Gold and Silver Surfaces Determines Their Ability To Resist Protein Adsorption. *The Journal of Physical Chemistry B*, 102:426–436, 1998.
- [12] T. Aqua, R. Naaman, and S.S. Daube. Controlling the Adsorption and Reactivity of DNA on Gold. *Langmuir*, 19(25):10573–10580, 2003.
- [13] S. Peeters, T. Stakenborg, G. Reekmans, W. Laureyn, L. Lagae, A. van Aerschot, and M. van Ranst. Impact of spacers on the hybridization efficiency of mixed self-assembled DNA/alkanethiol films. *Biosensors and Bioelectronics*, 24:72–77, 2008.
- [14] E. Wedege and G. Svenneby. Effects of the blocking agents bovine serum albumin and tween 20 in different buffers on immunoblotting of brain proteins and marker proteins. *Journal of Immunological Methods*, 88:233–237, 1986.
- [15] W.K. Lee, J.S. Ko, and H.M. Kim. Effect of electrostatic interaction on the adsorption of globular proteins on octacalcium phosphate crystal film. *Journal of Colloid and Interface Science*, 246:70–77, 2002.
- [16] Z.G. Peng, K. Hidajat, and M.S. Uddin. Adsorption of bovine serum albumin on nanosized magnetic particles. *Journal of Colloid and Interface Science*, 271:277–283, 2004.
- [17] T.J. Peters. Serum albumin. *Advances in Protein Chemistry*, 37:161–245, 1985.

- [18] A. Docoslis, W. Wu, R.F. Giese, and C.J. van Oss. Measurements of the kinetic constant of protein adsorption onto silica particles. *Colloids and Surfaces B: Biointerfaces*, 13:83–104, 1999.

Chapter 7

Torsional stiffness of a protein system: a feasibility study

We demonstrate the feasibility of rotational actuation of magnetic particles to measure the torsional stiffness of a biological molecular system with a length scale of several tens of nanometers. As a model system we use protein G coated particles that binds selectively to the crystallisable part of the IgG antibody adsorbed onto a polystyrene substrate. The M-270 carboxyl particles used in the experiments show optically not sufficient contrast to follow the rotational behavior of the particles. Therefore we labeled the M-270 particles with 250 nm non-magnetic spherical polystyrene particles which allows to reconstruct the angle of rotation by image analysis of video microscopy images. The angular orientation of the particles that are bound to the substrate shows an oscillating behavior upon applying a rotating magnetic field. The amplitude of the oscillation decreases with increasing anti-body concentration. This we attribute to the formation of multiple bonds between the particle and the surface which increases the effective stiffness. We find a lower limit of the torsional modulus of $4.5 \cdot 10^{-26}$ Nm² which is two orders of magnitude larger than typical values found for DNA strands. This can be qualitatively understood from the structural properties of the protein complex.

A condensed version of this chapter is in preparation for publication: X.J.A. Janssen, J.M. van Noorloos, L.J. van IJzendoorn, A.M. de Jong and M.W.J. Prins *Torsional stiffness of a protein system: a feasibility study*

7.1 Introduction

In single molecule experiments the torsional properties of micrometer sized DNA strands have been studied using magnetic^[1-3] and optical tweezers.^[4] In this chapter we show the feasibility of rotational actuation of magnetic particles to measure the torsional stiffness of a biological system that is only several tens of nanometers long. As a model system we use protein G on the polystyrene particle that binds selectively to the crystallisable part of the IgG antibody^[5] that is absorbed onto the polystyrene substrate as schematically represented in figure 7.1.

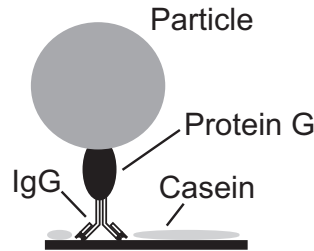


Fig. 7.1: Schematic representation of the model system to measure the torsional stiffness of an antibody-antigen couple. Protein G on a particle binds selectively to the crystallisable part of an IgG antibody located on the surface of a polystyrene substrate. The surface is blocked with Casein to prevent non-specific binding between the polystyrene substrate and the protein G on the particle. Note that the size of the proteins is largely exaggerated compared to the size of the particle.

First we present a mathematical description that shows how the presence of a bond influences the movement of the particle in a rotating magnetic field. Hereafter we give the magnetic properties of the labeled M-270 particles that are used in the experiments. Finally we show some results of measurements on the torsional stiffness of the IgG-protein G system.

7.2 Rotational properties of bound particles

We describe the presence of a bond between a particle and a substrate by a torsion spring that obeys the angular form of Hooke's law:

$$\tau = -k\theta \quad (7.1)$$

with τ the torque on the spring, k the torsional spring constant and θ the angular rotation of the spring away from its equilibrium position.

To make equation 7.1 more generally applicable, we introduce an angular dependent torsional spring constant $k(\theta)$ and add this term to the equation of motion (Eqn. 5.5):

$$m\mu_0 H \sin(\omega_f t - \theta) = \lambda \frac{d\theta}{dt} - k(\theta)\theta \quad (7.2)$$

The equation of motion now gives the balance between the applied magnetic torque (left-hand side) and the sum of the hydrodynamic and spring torsional torque (right-hand side). We solved this differential equation numerically and found that depending on the ratio between the magnetic torque (mB) and the torsional spring constant (k), the particle shows a characteristic movement when a rotating magnetic field is applied (Fig. 7.2).

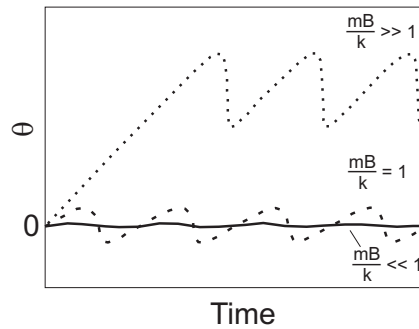


Fig. 7.2: The angular orientation of the particle (θ) in time for different ratios between the magnetic torque (mB) and an angle-independent torsional spring constant ($k(\theta) = k$) as obtained by numerically solving the equation of motion (Eqn 7.2). For a very stiff biological system the particle hardly rotates. For a torsional spring constant comparable to the applied magnetic torque, the particle shows an angular orientation that oscillates around zero. For a very weak torsional spring constant the particle follows the rotating field over several revolutions whereafter the oscillation starts.

When the magnetic torque is comparable to the torsional spring constant, the particle follows the magnetic field and as a result the spring is loaded. For increasing angular orientation, the torque due to the spring increases and the angle between the magnetic moment and the field has to increase for the magnetic torque to increase and the particle to follow the field. When the angle between the magnetic field and the magnetic moment exceeds 90 degrees, the magnetic torque decreases and the particle is rotated in opposite direction due to the torque of the spring. As a result, the angle between the field and the magnetic moment increases further and as the angle exceeds 180 degrees, the magnetic torque changes direction and pulls the particle back even faster (causing asymmetry in the oscillations). As a result, the angle between the magnetic moment and the field decreases, the

particle is pulled back to its equilibrium position and the cycle is repeated.

When the ratio between the magnetic torque (mB) and the torsional spring constant (k) is small, the amplitude of the oscillations is very small. For a very weak torsional spring constant, the spring is rotated over several revolutions before the torque of the spring equals the magnetic torque. Since the field continues to rotate, the spring can at maximum unwind one turn before the magnetic moment is again overtaken by the field. As a result the equilibrium position of the oscillations is shifted away from zero. By measuring and analyzing the oscillatory behavior of the particle in time, we can deduce the torsional spring constant of the biological system sandwiched between the particle and substrate.

In this illustrative example an angle-independent torsional spring constant ($k(\theta) = k$) is used, whereas in reality $k(\theta)$ is likely to be a more complicated function. Note that this does not limit the interpretation of the measured angular orientation of the particle in time, since only the detailed shape of the measured angular orientation of the particle in time is directly dependent on $k(\theta)$. The overall oscillatory movement will always be observed as it arises from the fact that the field periodically overtakes the magnetic moment.

7.3 Experimental

For the experiments described in this chapter, we used Dynal M-270 carboxyl particles with a diameter of $2.7 \mu\text{m}$ instead of the Dynal M-280 streptavidin particles. Light microscopy images reveal that the M-270 carboxyl particles do not show a characteristic pattern as that is visible on the M-280 particles. The absence of this pattern prevents the detection of particle rotation upon applying a rotating magnetic field. Scanning electron microscopy (SEM) images show that the surface roughness of the M-270 particles is remarkably smaller than that of the M-280 particles (Fig. 7.3a and b). In order to study the rotation of M-270 carboxyl particles, we artificially create a visible pattern by labeling the particles with small (250 nm) non-magnetic polystyrene particles (Fig. 7.3c).

Besides labeling with small particles, the M-270 particles also have to be coated with protein G.^[6] Since the small particles are large compared to the size of proteins, care has to be taken that only a small number (typically < 10) of small particles is bonded to the large particle. Otherwise the protein G on the M-270 particle can not come in contact with the IgG on the surface of the substrate due to steric hindrance. Note that the binding of the small particles is a statistical process, so the exact number of small particles bound to a large particle is not known. Although the small particles create a visible pattern on the large particles, the number of small particles can not be determined optically since the size of the small particles is below the diffraction limit of the light microscope.

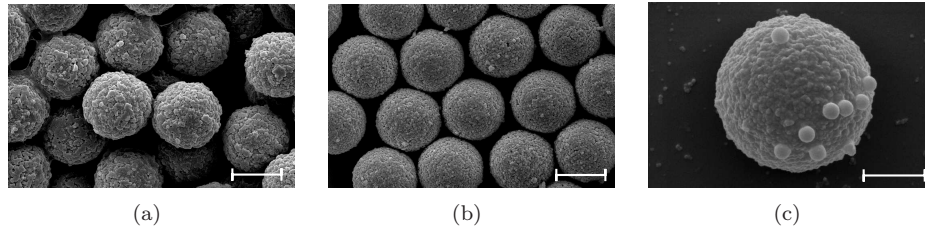


Fig. 7.3: (a) SEM pictures of Dynal M-280 streptavidin and (b) M-270 carboxyl particles show the difference in surface roughness. The scale bar represents $2\ \mu\text{m}$. (c) M-270 particles labeled with $250\ \text{nm}$ non-magnetic polystyrene particles. The scale bar represents $1\ \mu\text{m}$.

The functionalization of the M-270 particles is done using the following steps:

- Coupling biotin EZ-link^[7] to the M-270 particles by activation of carboxyl groups using 1-ethyl-3-(3-dimethylaminopropyl) carbodiimide (EDC).
- Removing excess of EDC and unbound biotin EZ-link.
- Coupling protein G to the remaining activated carboxyl groups.
- Removing excess of *N*-Hydroxysuccinimide (NHS) and unbound protein G.
- Labeling the M-270 particles with $250\ \text{nm}$ streptavidin coated particles that bind to the biotin.
- Quenching activated carboxyl groups with ethanolamine.
- Washing and storage in PBS buffer.

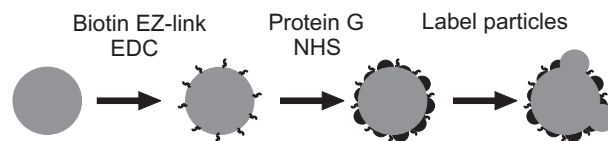


Fig. 7.4: Schematic representation of the functionalization of the M-270 carboxyl particles. First the carboxyl groups are activated with EDC and a fraction of them is used to covalently bind biotin EZ-link. Once the excess EDC and biotin EZ-link is washed away, the streptavidin coated $250\ \text{nm}$ non-magnetic polystyrene particles are added to label the M-270 particles.

It is deliberately chosen to do the activation of the carboxyl groups and the coupling of protein G in two separate steps. If protein G would be present together with EDC, cross-linking of protein G molecules can occur between carboxyl and amine groups that are both present in the protein G molecules.

7.4 Results and discussion

7.4.1 Permanent magnetic moment of M-270 particles

We applied a rotating magnetic field to the labeled M-270 particles to study the magnetic properties of the particles. It is observed that the particles follow the rotating magnetic field up to a breakdown frequency (Fig. 7.5a). Above the breakdown frequency, the average particle rotation frequency decreases with increasing field frequency. Furthermore, we observed oscillations in the angular orientation of the particle when applying a field frequency above the breakdown frequency. The oscillations have a frequency that is equal to the difference of the field frequency and the average rotation frequency of the particle. These observations make us to conclude that the M-270 particles have a permanent magnetic moment as is also observed for the M-280 particles (chapter 5).

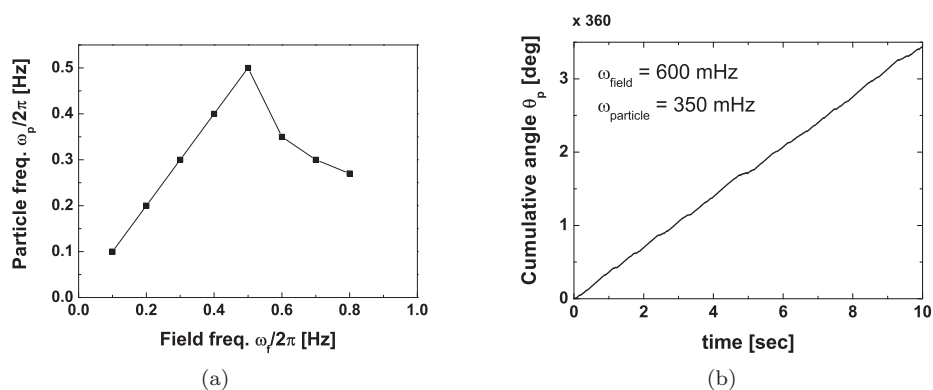


Fig. 7.5: (a) Average rotation frequency of the particle as function of the frequency of the applied field for a field strength of 2 mT. The line is plotted as a guide to the eye. (b) Cumulative angle of the particle measured over 10 seconds gives an average particle rotation frequency of 350 mHz when applying a field of 2 mT with a field frequency of 600 mHz.

The angular orientation of the particle is measured in time for a field frequency slightly above the breakdown frequency and the average particle rotation frequency is found by linear fitting the data (Fig. 7.5b). The permanent magnetic moment of the particle is then determined from the average particle rotation frequency as described in chapter 5. If we use the same approximation as used to determine the permanent magnetic moment of the M-280 particles *i.e.* drag constant for a particle in a bulk fluid ($\lambda = 8\pi\eta R^3$), the permanent moment of the M-270 particle is found to be $1.3 \cdot 10^{-16}$ Am². This is a factor of ten lower than the maximum permanent moment found for the M-280 particles. Furthermore, the particle-to-particle variation in permanent magnetic moment is of the order of 25% where for the M-280 particles a spread of a factor 10 is found. Note that the presence of

the small particles increases the hydrodynamic drag of the particle and leads to an underestimation of the permanent magnetic moment.

The increase in hydrodynamic drag due to the presence of a small particle is proportional to the effective fluid speed around the small particle and therefore dependent on the position of the small particle (Fig. 7.6a). Note that the fluid near the surface of the M-270 particle is dragged around due to the no-slip condition on its surface.

The flow profile around the M-270 particle at the equatorial plane can be approximated by that of an infinite long cylinder (Fig. 7.6b) and is given by:^[8]

$$v(r) = \frac{\omega R^2}{r} \quad (7.3)$$



Fig. 7.6: (a) The increase in hydrodynamic drag due to the presence of a small particle attached to a large rotating particle is dependent on the position of the small particle. The hydrodynamic force on the small particle results in a torque on the large particle. The lever on which this force acts becomes smaller when the particle is positioned further away from the equatorial plane of the large particle. (b) The flow profile around an infinite long cylinder with radius R that rotates in a fluid around its long axis is given by $v(r) = \frac{\omega R^2}{r}$. A small cylinder with radius R' that is attached to the large cylinder experiences a drag force proportional to the effective fluid speed i.e. $v_{eff} = (R + R')\omega - \frac{\omega R^2}{R + R'}$

The drag force on a sphere with radius R' moving with a speed v through a fluid with viscosity η is given by:

$$F_{drag} = -6\pi\eta R' v_{eff} \quad (7.4)$$

The effective speed at which the small particle moves through the fluid is approximated by:

$$v_{eff} = v_{small} - v_{fluid} = (R + R')\omega - \frac{\omega R^2}{R + R'} \quad (7.5)$$

Substitution of the effective speed gives the drag force on the small particle:

$$F_{drag} = -6\pi\eta\omega R' \left[R + R' - \frac{R^2}{R + R'} \right] \quad (7.6)$$

which corresponds to a torque with respect to the rotational axis of the large particle:

$$\tau_{small} = -6\pi\eta\omega [R'^3 + 2RR'^2] \quad (7.7)$$

The total torque on the large particle with respect to its rotational axis is then given by:

$$\tau_{total} = -8\pi\eta\omega R^3 - 6\pi\eta\omega [R'^3 + 2RR'^2] \quad (7.8)$$

Binding a single 250 nm particle to the equator of a 2.7 μm particle increases the hydrodynamic drag with 1%. When the small particle is bound further away from the equator, the influence on the hydrodynamic torque of the large particle becomes smaller since the lever at which the torque works is smaller. Note that SEM pictures show that there are typically less than ten small particles bound to a large particle. When the large particle would be entirely covered with small particles, its radius is effectively increased by the diameter of the small particle. For a 2.7 μm particle entirely covered with 250 nm particles, the hydrodynamic drag is increased with a factor 1.7. So by neglecting the increased hydrodynamic drag, we underestimated the permanent magnetic moment at maximum with a factor of 1.7. In the following part of this chapter we will use the found moment of $1.3 \cdot 10^{-16} \text{ Am}^2$ in the calculations of the torque applied to the particles.

7.4.2 Sample preparation

A cell with a diameter of 9 mm and a depth of 0.12 mm was made using a polystyrene substrate and a Secure-Seal spacer (Fig. 7.7).

Mouse IgG antibodies^[9] are physically adsorbed on the substrate by incubation for 45 minutes with 100 μL of a given concentration of IgG in phosphate buffered saline (PBS). Then the substrate is rinsed with PBS and blocked with casein for 45 minutes to reduce non-specific binding of the particles to the bare polystyrene. After rinsing the sample with PBS, the particles are added and the cell is closed with a cover slip. The particles sediment and bind selectively to the substrate due to the formation of IgG-protein G bonds. After this incubation process, the sample is turned upside-down and the unbound particles sediment to the bottom of the cell.

The fraction of bound particles is determined as function of the IgG concentration used for incubation (Fig. 7.8). For low IgG concentration very few particles bind to the surface indicating a low amount of IgG present on the surface of the substrate and more important, a low amount of non-specific binding of the par-

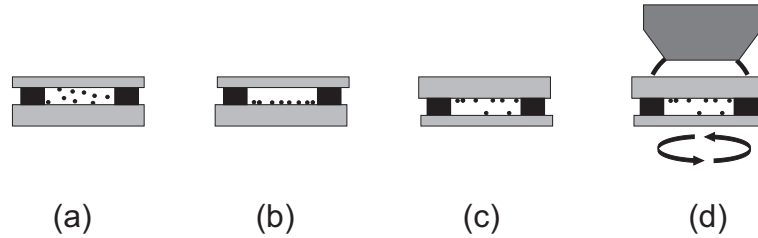


Fig. 7.7: (a) A cell made of a substrate coated with IgG is filled with particle solution and covered with a cover slip. (b) The particles sediment onto the functionalized surface and bind specifically by the formation of IgG - protein G bonds. (c) The sample is turned upside-down and the unbound particles sediment to the bottom of the cell. (d) The immersion objective is focused onto the particles hanging below the substrate and the rotational behavior of the bound particles is studied in a rotating magnetic field.

ticles to the casein blocked substrate. Above $1 \cdot 10^{-8}$ M the fraction of bound particles increases rapidly with increasing IgG concentration.

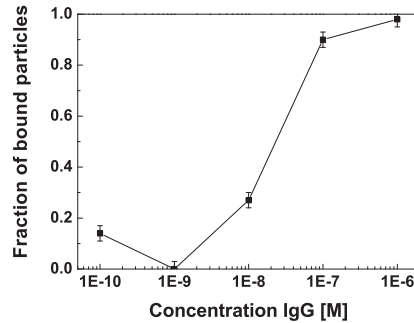


Fig. 7.8: The fraction of particles bound to the surface versus the IgG concentration used for incubation of the polystyrene surface. The line is plotted as a guide to the eye.

The absolute amount of IgG on the surface (number of molecules per unit surface) is not known since it depends on the binding rate of IgG during incubation, on the concentration of IgG and on the incubation time. Since the particles specifically bind to the surface we conclude that each particle has at least one IgG-protein G bond with the surface. We therefore attribute the rapid increase in binding above $1 \cdot 10^{-8}$ M to the fact that the surface coverage becomes high enough that each particle can form at least one bond. Note that for a given IgG concentration, the number of bonds per particle can vary since the binding is a statistical process and the proteins (IgG and protein G) are not likely to have a uniform spatial distribution over the surfaces (substrate and particle).

7.4.3 Torsional stiffness of IgG-protein G couple

We measured the rotational behavior of the particles for two different IgG concentrations (50 nM and 1 μ M) in a magnetic field of 22 mT rotating at 200 mHz. By evaluation of the recorded video-streams it is observed that angular movement of the particles can be divided in two categories: particles that show an oscillating angular orientation and particles that are static *i.e.* do not show any angular motion. For an IgG concentration of 50 nM, about 50% the particles show an oscillating movement whereas for 1 μ M, the fraction of oscillating particles decreases to only a few percent. We attribute the increase of the static fraction with increasing IgG concentration to the fact that the surface coverage becomes high enough such that particles can form multiple bonds. Consequently, the effective bond between the particles and the substrate becomes stiffer and the particles are not able to follow the rotating field.

For the oscillating fraction it is observed that the particles are able to follow the rotating magnetic field typically over tens of degrees which indicates that the applied torque is of the order of the torsional stiffness of the biological system *i.e.* ($\frac{mB}{k} \approx 1$). Figure 7.9 shows the typical behavior for two IgG concentrations (50 nM and 1 μ M).

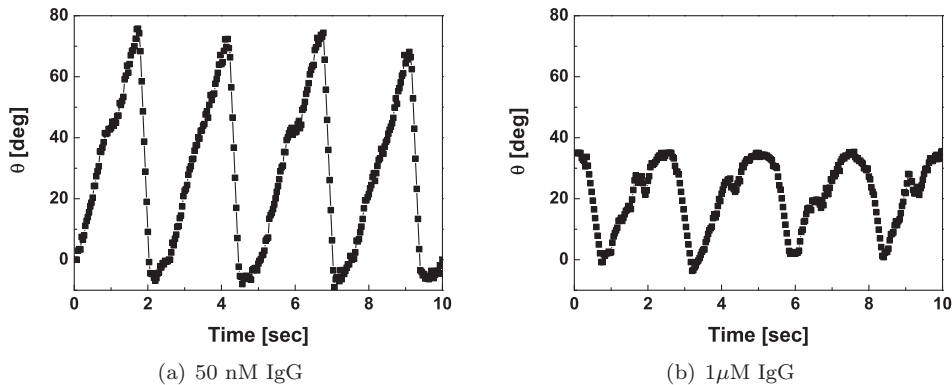


Fig. 7.9: Angular orientation of a particle bound to a substrate coated with (a) 50 nM and (b) 1 μ M IgG measured with an applied rotating field of 200 mHz and 22 mT. The measured oscillation frequency is twice the rotation frequency of the field because of remagnetization of the particle. We attribute the artifacts in the rising slopes to the interpolation technique used in the image analysis software.

Initially, the particle is able to follow the rotating field and the biological molecules become twisted. Consequently the torque on the particle increases. For the particle to rotate further, the angle between the field and the permanent magnetic moment has to increase in order to increase the magnetic torque. When the magnetic torque reaches its maximum, the particle does not rotate any further and the angle between the magnetic moment and the field becomes larger than 90

degrees. As a result, the magnetic torque decreases and the particle rotates back quickly. The cycle is repeated when the magnetic moment is again overtaken by the field.

In the experiments, it is observed that the oscillation frequency of the particle is twice the rotation frequency of the field. This behavior can not be explained by the model based on a permanent magnetic moment of the particle. However, this double frequency might be explained by remagnetization of the particle at the moment the field opposes the magnetic moment of the particle. Note that remagnetization is only possible when the applied field exceeds the coercive field of the particle. This is verified by studying the behavior at low field strength and indeed no flipping of the magnetic moment is observed when $B < 3$ mT *i.e.* at low fields the oscillation frequency is equal to the rotation frequency of the field. Consequently the term permanent magnetic moment is incorrect and it would be more appropriate to speak in terms of a (uniaxial) ferromagnetic moment.

The amplitude of the oscillations is measured as function of the applied field (Fig. 7.10a) for two different IgG concentrations (50 nM and 1 μ M). Note that in each of the two measurement series a single particle is studied to avoid influence from particle-to-particle variations in the magnetic moment and/or hydrodynamic properties. For increasing field strength, the magnetic torque increases and the particle is able to rotate over a larger angle before the torque of the biological system equals the maximum applied magnetic torque. For increasing IgG concentration we hypothesize that more IgG-protein G bonds are formed between the particle and the surface. As a result the effective binding becomes stiffer and the maximum angle over which the particle rotates decreases when applying the same magnetic torque.

Note that in principle also the viscous drag influences the rotational behavior *i.e.* due to the viscous drag the particle can not follow a high field frequency and in that case the maximum angle becomes smaller. In the experiments, the angular velocity of the particle is typically smaller than 1 rad/s which corresponds to a hydrodynamic torque of $7 \cdot 10^{-20}$ Nm whereas the applied magnetic torque is typically between $4 \cdot 10^{-19}$ Nm and $3 \cdot 10^{-18}$ Nm for field strengths between 3 mT and 20 mT. Therefore the influence of the drag can be neglected, especially for high field strengths (> 10 mT).

The amplitude of the oscillation was also measured for several concentrations of the IgG solution used for incubation using a rotating field of 20 mT (Fig. 7.10b). A relatively large variation in the measured maximum angle was found for a fixed IgG concentration when measuring the angular movement of different particles on the same sample. These variations are most likely caused by a varying number of bonds between the particles and the surface due to a non-uniform spatial distribution of IgG and protein G.

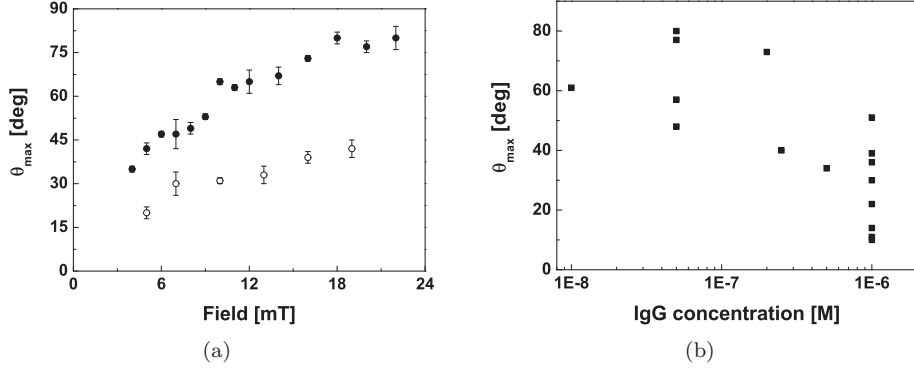


Fig. 7.10: (a) Amplitude of the oscillations versus the field strength for a substrate coated with 50 nM (●) and 1 μM (○) IgG. In each of the two measurement series a single particle is observed while changing the magnetic field strength to avoid influence from particle-to-particle variations in the magnetic moment and hydrodynamic properties. (b) The amplitude of the oscillation is measured for increasing IgG concentration using a field of 20 mT. The decrease in amplitude with increasing IgG concentration is attributed to an increasing number of bonds between the surface and the particle. The multiple data points at a given IgG concentration are obtained by measuring different particles using the same sample.

From the measured angular orientation in time we can determine the torsional spring constant of the system by rewriting the equation of motion:

$$k(\theta) = \frac{mB_1 \sin(\omega t_1 - \theta) - 8\pi\eta R^3 \left. \frac{d\theta}{dt} \right|_{t_1}}{\theta} \quad (7.9)$$

Note that the angular orientation of the particle in figure 7.9 has been determined with respect to the angular orientation of the particle in first frame of the video recording. Therefore the absolute orientation of the particle (θ) with respect to the equilibrium position *i.e.* that position where no energy is stored in the spring ($k(\theta)\theta = 0$) is not known.

As mentioned earlier, for a particle with a uniaxial ferromagnetic moment, the angle between the magnetic moment and the field is 90 degrees when the rotation of the particle is reversed. Exploiting this knowledge, we can calculate the angle ($\omega_f t - \theta$) between the field and the magnetic moment from that point backwards in time for any given point on the curve where the particle follows the field. So although the orientation of the particle with respect to the equilibrium position is not known, we can calculate the torque due to the biological system $k(\theta)\theta = mB_1 \sin(\omega t_1 - \theta) - 8\pi\eta R^3 \frac{d\theta}{dt}$ and plot this versus the angular orientation θ with an unknown offset θ_0 .

Figure 7.11 shows the results when using the data presented in figure 7.9. Linear fitting of the data gives a constant torsional spring constant of respectively $(1.5 \pm 0.3) \cdot 10^{-18}$ Nm/rad and $(4.2 \pm 0.6) \cdot 10^{-18}$ Nm/rad for a substrate incubated with 50 nM and 1 μ M IgG. Note that although $1.5 \cdot 10^{-18}$ Nm/rad is the smallest torsional spring constant we measured, we can not assume that to be the torsional spring constant of a single IgG-protein G couple since we can not rule out the presence of multiple bonds.

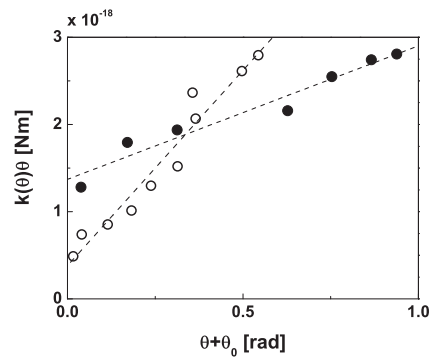


Fig. 7.11: The torque due to the biological system plotted versus the angular orientation of the particle θ with an unknown offset θ_0 . Linear fitting of the data gives a constant torsional spring constant of respectively $(2.7 \pm 0.3) \cdot 10^{-20}$ Nm/rad and $(7.5 \pm 0.6) \cdot 10^{-20}$ Nm/rad for a substrate incubated with 50 nM IgG (●) and 1 μ M IgG (○) IgG.

When comparing torsional spring constants of different biological systems one has to take into account that the spring constant is not a material property but is dependent on the length of the spring. One way of comparing systems with different length scales is by calculating the torsional modulus *i.e.* the torsional spring constant times the length of the spring. The size of the protein G molecule is dependent on its spatial structure and is not exactly known. For antibodies the size is well known and typically 15 nm x 7 nm x 3.5 nm.^[5] If we assume a biological system of 30 nm long (twice the size of the antibody) we find a torsional modulus of $4.5 \cdot 10^{-26}$ Nm² for the torsional spring constant of $1.5 \cdot 10^{-18}$ Nm/rad. Torsional moduli of double stranded DNA^[4] are reported of the order of $3 \cdot 10^{-28}$ Nm² which is roughly two orders of magnitude smaller than we find for the IgG-protein G system.

It is interesting to investigate whether it is possible to estimate the ratio in the torsional moduli between DNA and a IgG-protein G complex. An order of magnitude estimate of the ratio might be obtained by calculating the torsional modulus of the biological system assuming a continuum approximation and an equal shear modulus for both biological systems (DNA and the antibody-antigen complex). The biological system might be considered as a cylindrical rod (Fig.

7.12) with a diameter R and a length L . When this mesoscopic rod is twisted by applying a torque τ , the twist θ is given by:^[10]

$$\theta = \frac{\tau L}{JG} \quad (7.10)$$

with G the shear modulus of the material and J the polar moment of inertia of a disk ($J = \frac{1}{2}\pi R^4$). Introduction of the torsional spring constant $k = \frac{GJ}{L}$ gives the angular form of Hooke's law ($\theta = \frac{\tau}{k}$) and the torsional modulus (kL) of the cylindrical shaft increases with the diameter of the rod to the fourth power:

$$kL = \frac{GJ}{L}L = GJ = \frac{1}{2}\pi R^4G \quad (7.11)$$

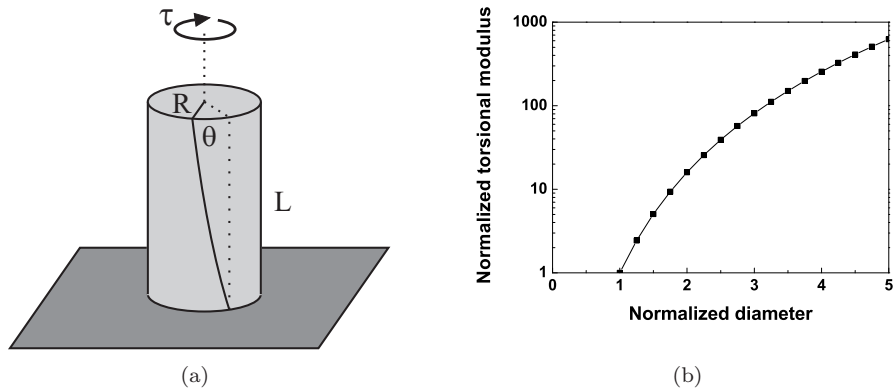


Fig. 7.12: (a) Schematic representation of a cylindrical rod with a diameter R and a length L that is twisted over an angle θ by a torque τ . (b) The normalized torsional modulus of a cylindrical shaft increases with the diameter of the rod to the fourth power.

Using this relation and assuming equal values for the shear modulus, we can estimate the ratio in torsional modulus between DNA and an antigen-antibody couple. The radius of a DNA strand ($1.2 \text{ nm}^{[11]}$) is about three to four times smaller than that of an antibody-antigen couple which, according to equation 7.11, results in a 100 to 200 times smaller torsional modulus. The ratio between the measured torsional moduli is approximately $\frac{4.5 \cdot 10^{-26}}{3 \cdot 10^{-28}} = 150$. This value is similar to the value calculated with equation 7.11 which is remarkable in view of the involved assumptions. A more extended comparison using molecular-based models is still to be done.

The constant torsional spring constant that is found for small (< 90 degrees) angular deformation, implies a harmonic potential and consequently, the deformation of the antigen-antibody couple was described with the angular form of

Hooke's law. For larger angular deformation, significant and possibly irreversible changes of the antigen-antibody couple can be expected. Therefore, although not possible with the current setup, it is interesting to perform measurements in which a larger magnetic torque can be applied to the particle.

7.5 Conclusion

In summary, we have used rotational actuation of magnetic particles to measure the torsional stiffness of a small biological system sandwiched between a particle and a substrate. As a model system we used protein G on the particles that binds selectively to the crystallisable part of the IgG antibody that is present on a polystyrene substrate. The angular orientation of the bound particles shows an oscillating behavior upon applying a rotating magnetic field. We attribute the decreases of this amplitude with increasing anti-body concentration to the formation of multiple bonds between the particle and the surface. The lowest torsional modulus we found is typically two orders of magnitude larger than that of double stranded DNA. In conclusion, we have proven that rotational actuation of magnetic particles can be used to measure the torsional stiffness of a biological system with a typical length scale of several tens of nanometers like an antibody-antigen couples.

References

- [1] D.A. Koster, V. Croquette, C. Dekker, S. Shuman, and N.H. Dekker. Friction and torque govern the relaxation of DNA supercoils by eukaryotic topoisomerase IB. *Letters to Nature*, 434:671–674, 2005.
- [2] D.A. Koster, K. Palle, E.S.M. Bot, M.A. Bjornsti, and N.H. Dekker. Antitumour drugs impede DNA uncoiling by topoisomerase I. *Nature*, 448:213–217, 2007.
- [3] K. Besteman, S. Hage, N.H. Dekker, and S.G. Lemay. Role of Tension and Twist in Single-Molecule DNA Condensation. *Physical Review Letters*, 98(5):058103, 2007.
- [4] S. Forth, C. Deufel, M.Y. Sheinin, B. Daniels, J.P. Sethna, and M.D. Wang. Abrupt Buckling Transition Observed during the Plectoneme Formation of Individual DNA Molecules. *Physical Review Letters*, 100:148301–4, 2008.
- [5] W.K. Lee, J.S. Ko, and H.M. Kim. Effect of electrostatic interaction on the adsorption of globular proteins on octacalcium phosphate crystal film. *Journal of Colloid and Interface Science*, 246:70–77, 2002.
- [6] Protein G, Calbiochem lot: D00031516.

- [7] EZ-link Biotin-PEO₃-Amine, Pierce.
- [8] P. K. Kundu and I.M. Cohen. *Fluid Mechanics*. Academic press, 2002.
- [9] Mouse IgG serum in PBS, Calbiochem lot: D00056508.
- [10] F.P. Beer, E.R. Johnston, and J.T. DeWolf. *Mechanics of materials*. McGraw Hill, 3 edition, 2001.
- [11] B.Alberts, A. Johnson, J. Lewis, M. Raff, K. Roberts, and P. Walter. *Molecular Biology of the Cell*. Garland, 4 edition, 2002.

List of publications

Papers

- X.J.A. Janssen, J.M. van Noorloos, L.J. van IJzendoorn, A.M. de Jong and M.W.J. Prins *Torsional stiffness of a protein system: a feasibility study* In preparation
- X.J.A. Janssen, A. van Reenen, L.J. van IJzendoorn, A.M. de Jong and M.W.J. prins *The rotating particles probe: a new technique to measure interactions between protein-coated particles and a substrate* In preparation
- A. Ranzoni, X.J.A. Janssen, M. Ovsyanko, L.J. van IJzendoorn and M.W.J. Prins *Magnetically controlled rotation and torque of uniaxial microactuators for lab-on-a-chip applications* accepted for publication in Lab on a Chip
- X.J.A. Janssen, A.J. Schellekens, K. van Ommering, L.J. van IJzendoorn and M.W.J. Prins *Controlled torque on super-paramagnetic beads for functional biosensors* Biosensors and Bioelectronics **24**, 1937–1941 (2009)
- X.J.A. Janssen, L.J. van IJzendoorn and M.W.J. Prins *On-chip manipulation and detection of magnetic particles for functional biosensors* Biosensors and Bioelectronics **23**, 833–838 (2008)

Papers not related to this work:

- C.C. van Donkelaar, X.J.A. Janssen and A.M. de Jong *Distinct developmental changes in the distribution of calcium, phosphorus and sulphur during fetal growth* Journal of Anatomy **210** 186-194 (2007)

Poster presentations international

- Gordon research conference on Bioanalytical Sensors June 29 - July 4, 2008
Bryant University Smithfield, RI, USA
- ESF-EMBO symposium biomagnetism and magnetic biosystems based on
molecular recognition processes, September 22-27, 2007 Sant Feliu de Guixols,
Spain.
- Scientific and Clinical Applications of Magnetic Carriers, May 17-20, 2006
Krems, Austria

Patent applications

- Torque calibration on magnetic particles (in priority year)
- Magnet design (in priority year)
- X.J.A. Janssen, L.J. van IJzendoorn, M.W.J. Prins, *Sensor with HF-AC
magnetic field*, Publication number: WO2009037636
- W.U. Dittmer, P. de Kievit, J.H. Nieuwenhuis, M.W.J. Prins, L.J. van
IJzendoorn, X.J.A. Janssen, *Measuring agglutination parameters*, Publica-
tion number: WO2008075285

Acknowledgments / *dankwoord*

Tijdens mijn promotie onderzoek heb ik veel hulp van anderen gekregen en zonder iemand tekort te willen doen, wil ik hierbij een aantal mensen met naam bedanken.

Allereerst wil ik mijn promotor Menno Prins en copromotor Leo van IJzendoorn bedanken voor alle begeleiding maar vooral voor de vrijheid die ik heb gekregen om mijn promotie-onderzoek richting te geven. Tevens wil ik ook Arthur de Jong bedanken voor alle inbreng in mijn onderzoek, maar ook als verantwoordelijke van het chemische lab. Dankzij jouw inzet bleef de hoeveelheid rommel in het chemische lab beperkt tot een aanvaardbaar niveau. I would also like to thank the members of the core-committee, Priv.-Doz.Dr.habil. Hubert Brückl, prof.dr. Nynke Dekker, and prof.dr.ir. René Janssen for their contribution to this thesis.

Graag bedank ik ook de mensen van Philips Research Eindhoven: Jeroen Veen, Theo Jansen, Joost Kahlman en Hans van Zon voor alle uitleg over de werking van de Philips biosensor, het ontwerp van de diverse chips en de discussies over nieuwe toepassingen van de sensor chips. Zonder jullie hulp en apparatuur had het onderzoek in onze nieuwe vakgroep nooit zo snel van start kunnen gaan. Verder wil ik ook graag de medewerkers van de faculteit-werkplaats bedanken voor het maken van de opstellingen, maar toch vooral ook voor alle klusjes die altijd weer snel "even tussendoor" mochten.

Ook wil ik alle collega's uit de vakgroep bedanken voor de samenwerking en de fijne sfeer binnen de groep. Francis Fahrni and Asha Jacob, thanks for being my room-mates. Francis and your girlfriend María, thanks for teaching me how to make Mojo and for importing Swiss Rösti and Thomy "Macht aus Gutem das Beste" mayonaise. Asha, thank you for introducing real biology to the physicists in our group. Verder alle promovendi binnen de groep: Loes van Zijp, Marijn Kemper, Mathias Irmscher, Kelly Yang en binnen Philips Research Eindhoven: Kim van Ommering en Andrea Ranzoni, bedankt voor alle discussies en lekkernijen bij de group-meetings en groepsuitjes. Voor alle hulp bij de Comsol Multiphysics simulaties en het uitlenen van de Hall-probe wil ik graag Roy Derks van de faculteit werktuigbouwkunde bedanken.

Verder wil ik ook alle stagairs: Frank Schoenaker, Frank Jehoel, Michael van Omering, Sjors Schellekens, Joost Verburg, Lindert Laven en Antoon Janssen en de afstudeerders: Petra Rombouts, Ben De Clercq en Joost van Noorloos bedanken voor hun bijdrage aan mijn onderzoek. Peter Pasmans, bedankt dat je nog tijd wilde vrijmaken voor het uitvoeren van de VSM metingen ondanks dat je toch zeer druk was met het afronden van jouw afstudeerverslag.

Voor alle steun door de jaren heen wil ik mijn familie, schoonfamilie en andere mensen uit mijn privésfeer bedanken. En als laatste An, niet alleen voor de mooie SEM foto's en alle hulp bij Latex, maar vooral dat je het al die tijd met mij hebt uitgehouden en je nog steeds mijn steun en toeverlaat bent.

Xander

Curriculum Vitae

- 19-11-1980 Born in Roermond, The Netherlands
- 1993 - 1998 HAVO, Scholengemeenschap St. Ursula Horn, The Netherlands
- 1998 - 2000 VWO, Scholengemeenschap St. Ursula Horn, The Netherlands
- 2000 - 2003 B. Sc. Applied Physics, Eindhoven University of Technology
- Research training under supervision of prof. dr. ir. K. Kopinga
Design of a RF-section for high-resolution NMR experiments
- Teaching assistant under supervision of prof. dr. ir. K. Kopinga
Assembly and calibration of dedicated sensitive temperature measurement systems
- 2003 - 2005 M. Sc. Applied Physics, Eindhoven University of Technology
- M. Sc. thesis: *Elemental distributions in the growth plate analyzed with a proton microprobe*
Supervision: Dr.ir. A.M. de Jong and dr. L.J. van IJzendoorn
- Research training: *Simultaneous measurements of galvanic evoked body sway and ocular torsion: a feasibility study*
Academic Hospital Maastricht, the Netherlands
Supervision: Prof.dr. H. Kingma
- 2005 - 2009 PhD research, Eindhoven University of Technology
- Department: Applied physics
Research group: Molecular Biosensors for Medical Diagnostics
Supervision: Dr. L.J. van IJzendoorn and prof.dr.ir. M.W.J. Prins